NORTHWESTERN UNIVERSITY

Superconductivity and optical properties of semiconductors

A DISSERTATION

SUBMITTED TO THE GRADUATE SCHOOL

IN PARTIAL FULFILLMENT OF THE REQUIREMENTS

for the degree

DOCTOR OF PHILOSOPHY

Field of Physics and Astronomy

By

Sung-Hyon Rhim

EVANSTON, ILLINOIS

December 2007

ABSTRACT

Superconductivity and optical properties of semiconductors

Sung-Hyon Rhim

A study of the optical properties and superconductivity in semiconductors is presented using the highly precise all-electron full-potential linearized augmented plane wave (FLAPW) density functional calculations.

Optical properties [$\varepsilon(\omega)$,$n(\omega)$,$k(\omega)$,$R(\omega)$ and $\alpha(\omega)$] of some III-V semiconductors [InAs, InSb, GaSb, and AlSb] and their critical point (CP) energies, are calculated from the eigenvalues and wave functions obtained from calculations using the screened-exchange local-density approximation (sX-LDA) with spin-orbit coupling included. The full $e^{i\mathbf{q}\cdot\mathbf{r}}$ expression for the optical matrix is incorporated instead of the momentum representation. The results show a remarkable improvement over the usual LDA and better agreement with experiment. The method employed has the following features: (i) it is based *purely* on first-principles without resorting to adjustable parameters and uses only the self-consistent eigenvalues and wave functions; (ii) the non-locality sX-LDA Hamiltonian requires using the longitudinal expression for the optical matrix elements.

In order to explore the excitonic (*or* electronic) mechanism of superconductivity, CuCl/Si superlattices are studied. Experimentally, CuCl epitaxy on Si (111) substrate was reported by Mattes and Foiles to have a nearly ideal diamagnetism between 60 and 150 K.

First, the superconducting transition temperatures (T_C's) are estimated using the electron-phonon (*e-p*) pairing mechanism in the rigid muffin-tin approximation (RMTA). Interface metallicity with 2D character is found for all CuCl/Si superlattices as evidenced by band structure, Fermi surfaces, and charge densities. A Hopfield parameter calculation shows that the electron-phonon interaction is present mostly at the interfaces and T_C is estimated to be $0.03 \sim 4.4$ K. Although superconductivity is present even when invoking the *e-p* mechanism, it is not strong enough to account for the experimentally reported T_C between 60 and 150 K. Other semiconductor heterostructures, such GaP/Si and ZnS/Si superlattices also reveal two dimensional metallicity at the interfaces but zero T_C. Although the *e-p* interaction is dominant at the interfaces, superconductivity is not present, which makes CuCl/Si superlattices special.

To further explore the excitonic (*or* electronic) mechanism of superconductivity, the dynamical dielectric function, $\varepsilon(\mathbf{q}, \omega)$ is evaluated for CuCl/Si superlattices. A theoretical formulation of the dielectric function and the inverse dielectric function, and the superconducting kernel function is provided. The pairing potentials $V_{\mathbf{k},\mathbf{k}'}$ and the kernel functions are evaluated. The results show that there is a range of energies from some CuCl/Si superlattices where there is an effective attractive electron-electron interaction involving the excitonic pairing mechanism.

Acknowledgment

I want to express my biggest and deepest thanks to Prof. Art Freeman, without whom this work would not have been possible. His constant encouragement and understanding, not only in my physics work but also in my personal development has been the cornerstone of my life as a physicist.

I am very lucky to be surrounded by colleagues with wonderful personalities and intelligence. Especially, I would like to thank Prof. Rolando Saniz, without whom this superconductivity work would have never been accomplished. His passion for physics has greatly influenced and educated me. I would like to express my gratitude to Prof. Jaejun Yu, my previous adviser in Korea. Discussions with him have helped me in understanding concepts more concretely. For discussing about physics problems, providing suggestions, I am grateful to Prof. John Ketterson for always answering my dumb questions. I thank Dr. Paul Sievert for his careful reading of this thesis and the discussions we have had on superconductivity. I greatly acknowledge Dr. Lin-Hui Ye, who has been my officemate. Regular discussions with him have broadened my insight and challenged my ignorance in physics. His explanations always helped me with clarity, in physics and especially in coding. Special thanks to “future Ph.D.” Nicholas Hatcher, whose wonderful personality has always filled the “bachelor’s office” with joy, comfort, and excitement, and who helped

tutor me in English.

I am indebted to Dr. Miyoung Kim, Dr. Joo-Hyoung Lee and Mary Lesniak for their support.

I want to express my gratitude to "FLAPW" family: Art and Doris Freeman, Prof. Michael Weinert, Dr. In-Gee Kim, Dr. Julia Medvedeva, Dr. Minsik Park and his wife, Dr. Y.-C. Hsueh, Dr. Jung-Hwan Song, Dr. Dima Novikov, Dr. Oleg Kontsevoi, Dr. Jun Li, Dr. Ryoji Asahi, Dr. Michel Posternak, Dr. Silvia Picozzi, Dr. Bernard Delley, Prof. Jae-Il Lee, Prof. B. I. Min, Prof. Tamio Oguchi, Dr. Tatsuya Shishidou, and Dr. Masatake Yamaguchi. I acknowledge Dr. Jong-Hyun Song.

I also want to thank many people who are not listed here, but guided me in many ways throughout my life.

Finally, I express my gratitude and honor to my family for their infinite and unconditional support. Especially to my father, who has been a role model in my life, whose perpetual passion in work has motivated and inspired me.

Contents

List of Tables

List of Figures

Chapter 1: Introduction

The richness of semiconductor physics for long drawn the attention of condensed matter physicists. Needless to say, semiconductor technology is of fundamental importance in modern electronic technology. Among interesting physics of semiconductors, optical properties and superconductivity, are challenging problems both theoretically and experimentally. First-principles calculation of the optical properties is an interesting subject for two reasons: (i) difficulty in describing excited states theoretically, and (ii) their potential applications for optoelectronic devices. Although a density functional[1,2] description of the ground states of solids with the local density approximation[3] (LDA) has been successful, description of band gaps of semiconductors are poor, i.e. LDA underestimates band gaps and erroneously predicts some semiconductors to be metallic. To calculate the optical properties, overcoming the band gap problem of LDA in semiconductors is crucial. To overcome these LDA shortcomings, the scissor operator was employed to match band gaps with experiment by rigidly shifting the conduction band upward. The screened-exchange LDA[4,5,6] (sX-LDA) was proposed and has shown a great improvement in the band gap and the optical properties over LDA. Unlike the scissor operator, the sX-LDA method is the fully first-principles using the self-consistent eigenvalues and wave functions. In this thesis, we present results of electronic structure and optical property calculations of some

III-V semiconductors; namely, InAs, InSb, GaSb and AlSb, calculated with FLAPW using the sX-LDA method with spin-orbit coupling included.

Superconductivity is an important subject in physics. In most cases, the pairing mechanism is believed to be phonon mediated. In many superconductors this was confirmed by isotope experiments.[7,8] The BCS theory, however, did not specify a particular pairing mechanism, but only assumed there is pairing between electrons. It was generally accepted that T_C of the phonon mechanism would be limited to low. An alternative, the so-called excitonic mechanism was suggested by Little[9] and Ginzburg,[10] which could lead to higher T_C. Later, Allender, Bray, and Bardeen[11] (ABB) studied the metal-insulator interface showing that an enhancement of T_C is possible. Subsequent experiments were conducted to find evidence of the excitonic mechanism in some PbTe or interface system but failed. Mattes and Foiles in 1985, reported ideal diamagnetism in CuCl epitaxy on Si substrate, whose T_C was speculated to be between 60 and 150 K.[12] After the Mattes and Foiles experiment, Yu and Freeman performed a preliminary calculation on a CuCl/Si superlattice with one CuCl layer, where interface metallicity and superconductivity was known to be highly plausible.[13] Despite of its possibility of enormously high T_C, the exciton mechanism has been forgotten for a long time, because of the discovery of the cuprates in 1986. Moreover, the geometry proposed by Ginzburg and Little, such as metallic chain, and dielectric-metal-dielectric sandwich structure were difficult to fabricate. We revisit the excitonic mechanism of superconductivity and present some results of CuCl/Si superlattices. The interface metallicity and possible superconductivity are investigated using results from the band structures, Fermi surfaces, and charge densities of these superlattices. At first, T_C is estimated by the rigid muffin-tin approximation (RMTA) within the

electron-phonon mediation scheme. The dynamic dielectric function is calculated and an effective screened electron-electron interaction is evaluated from its inverse. The kernel function is evaluated from the screened electron-electron interaction.

The CuCl/Si superlattices are unique because, although superlattices such as GaP/Si and ZnS/Si exhibit two dimensional metallicity at the interfaces, superconductivity is absent. Further, we extend our study of the CuCl/Si superlattice to the excitonic mechanism.

This thesis is organized as follows: In Chapter 2, a brief description of methodologies i.e. density functional theory (DFT), and the highly precise all-electron full-potential plane wave (FLAPW),[14,15] method is given. The local density approximation[3] (LDA) and screened exchange LDA[4,16,5,6] (sX-LDA) are also briefly discussed. Also a summary of the explicit orthogonalization (XO)[17] is presented. The XO removes the difficulty of ghost-bands. The optical properties of some III-V semiconductors, InAs, InSb, GaSb, and AlSb, are presented in Chapter 3, where all calculations are done by fully first-principles using the self-consistent eigenvalues and wave functions obtained from sX-LDA calculations with spin-orbit coupling included and without any adjustable parameters.[18] Superconductivity is discussed in Chapter 4.-6. A review of superconductivity is given in Chapter 4 which contains a historical overview, and a brief outline of BCS[19] and Eliashberg theory, McMillan T_C formula[20] and the rigid muffin-tin approximation (RMTA),[21] and the excitonic mechanism[9,10] and related past works. Interface metallicity and possible superconductivity are discussed in Chapter 5 for CuCl/Si, ZnS/Si, and GaP/Si superlattices and calculation results are presented.[22] The *e-p* mediation scheme is used to estimate T_C within the RMTA method. The exciton mechanism is treated in detail in Chapter 6, where a formal theory on the dielectric function and its inverse is given. The pairing potential and

the superconducting kernel function are outlined in this chapter followed by results of the CuCl/Si superlattices with the dynamic susceptibility calculations. We conclude this thesis with a summary given in Chapter 7. A detailed derivation of the pairing potential is given Appendix A. The tetrahedron integration with Dirac's delta function is discussed in Appendix B, where derivative of the weight of each corner point is used instead of the weights in the usual integration scheme given by Blöchl *et al.*[23]

Chapter 2: Method of calculation

2.1 Density functional theory

An early attempt of considering density as a fundamental quantity dates back late 1920's, when Thomas-Fermi (TF) propose the description of many-body system.[24,25] In TF model, the exchange-correlations were enormously simplified, but the attraction of the density functional approach was demonstrated : the number of degrees of freedom is reduced to a minimum. The rigorous formulation of the density functional theory (DFT) in its modern form, was first proposed by Hohenberg and Kohn (HK)[1] in 1964, which has become the foundation of most first-principles or *ab initio* calculations. Practical application to real material systems, however, was established by the Kohn-Sham scheme,[2] where the effective single-particle equation was derived. A further simplification was achieved by introducing local density approximation (LDA) to the exchange-correlation part in Kohn-Sham's single-particle equation.

2.1.1 Hohenberg-Kohn theorem

There are two fundamental theorems of DFT in the original formulation by Hohenberg and Kohn (HK).

The first HK theorem legitimizes the use of electron density $\rho(\mathbf{r})$ as the basic variable. It states that: the external potential $v(\mathbf{r})$ is determined, within a trivial additive constant, by the electron density $\rho(\mathbf{r})$. Since $\rho(\mathbf{r})$ determines the number of electrons, $\rho(\mathbf{r})$ also determines the ground-state wave function and other electronic properties of the system. Note that $v(\mathbf{r})$ is not restricted to Coulomb potentials. Once the external potential, $v(\mathbf{r})$ is given, the total Hamiltonian is known. In a non-degenerate system, the corresponding eigenstates $|\Psi\rangle$ and densities ρ are, in principle determined through Schrödinger equation,

$$\hat{H}|\Psi\rangle = E|\Psi\rangle, \tag{2.1}$$

where $\hat{H}$ is Hamiltonian, $\hat{H} = \hat{T} + \hat{V} + \hat{v}$ and $\hat{T}$, $\hat{V}$, and $\hat{v}$ are the kinetic, Coulomb interaction and external potential, respectively. The HK theorem tells us that a one-to-one and invertible mapping, $\hat{v} \rightarrow \Psi \rightarrow \rho(\mathbf{r})$ exists in the ground state. Energy functional can be written explicitly:

$$\begin{aligned} E_{\mathrm{v}}[\rho] &= \langle\Psi[\rho]|\hat{H}|\Psi[\rho]\rangle \\ &= \langle\Psi[\rho]|\hat{T} + \hat{V}|\Psi[\rho]\rangle + \langle\Psi[\rho]|\hat{v}|\Psi[\rho]\rangle \\ &= F_{HK}[\rho] + \int d\mathbf{r}\; v(\mathbf{r})\rho(\mathbf{r}), \end{aligned} \tag{2.2}$$

where the HK functional $F_{HK}[\rho]$ is universal and independent of external potential $v(\mathbf{r})$.

The second HK theorem provides the energy variational principles. It states that: for a trial density $\bar{\rho}$ such that $\bar{\rho} \geq 0$ and $\int d\mathbf{r}\; \bar{\rho} = N$,

$$E_0 \leq E_v[\bar{\rho}] \tag{2.3}$$

where $E_v[\bar{\rho}]$ is the energy functional of Eq. (2.2). To prove this theorem, note that the first theorem assures that $\bar{\rho}$ determines its own $\bar{v}$, Hamiltonian $\bar{\hat{H}}$, and wave function $\bar{\Psi}$, which

can be taken as a trial function for an external potential v. Thus

$$\langle\bar{\Psi}|\bar{\hat{H}}|\bar{\Psi}\rangle = \int d\mathbf{r}\ \bar{\rho}v(\mathbf{r}) + F_{HK}[\bar{\rho}] = E_v[\bar{\rho}] \geq E_v[\rho]. \tag{2.4}$$

The equality obtains for the true ground state density. The variational principle ((2.3)) requires that the ground-state density satisfy the stationary principle

$$\delta\Big(E_v[\rho] - \mu\Big[\int d\mathbf{r}\ \rho(\mathbf{r}) - N\Big]\Big) = 0, \tag{2.5}$$

which gives the Euler-Lagrange equation

$$\mu = \frac{\delta E_v[\rho]}{\delta\rho(\mathbf{r})} = v(\mathbf{r}) + \frac{\delta F_{HK}[\rho]}{\delta\rho(\mathbf{r})}. \tag{2.6}$$

2.1.2 Kohn-Sham scheme

While Hohenberg and Kohn (HK) theorems are mathematically rigorous and complete, there was no practical guide to construct explicit functionals. Kohn and Sham (KS)[2] introduced such a method (the KS scheme) to calculate the ground state properties for many-particle systems. The underlying assertion for KS scheme is that for any interacting system there exists a local single-particle potential $v_s(\mathbf{r})$ for a non-interacting system such that the exact ground state density of the interacting system, $\rho(\mathbf{r})$, equals to the ground state density of the non-interacting system. The energy functional can be rewritten as

$$\begin{aligned} E[\rho] &= \int d\mathbf{r}\ v(\mathbf{r})\rho(\mathbf{r}) + F_{HK}[\rho] \\ &= \int d\mathbf{r}\ v(\mathbf{r})\rho(\mathbf{r}) + T_s[\rho] + \frac{1}{2}\int\int \frac{\rho(\mathbf{r})\rho(\mathbf{r}')}{|\mathbf{r}-\mathbf{r}'|} + E_{\rm xc}[\rho], \end{aligned} \tag{2.7}$$

where $T_s[\rho]$ is the kinetic energy of a non-interacting system with density $\rho(\mathbf{r})$, and $E_{\rm xc}[\rho]$ is the exchange-correlation energy of an interacting system with density $\rho(\mathbf{r})$. An exchange-

correlation potential is defined as

$$\mu_{\rm xc}(\mathbf{r}) = \frac{\delta E_{\rm xc}[\rho]}{\delta \rho(\mathbf{r})} \ . \tag{2.8}$$

Applying variational principle to Eq. (2.7) subject to constraint $\int d\mathbf{r}\rho(\mathbf{r}) = N$ or $\delta\rho(\mathbf{r}) = 0$, Kohn and Sham[2] showed that for a given external potential $v(\mathbf{r})$ and exchange-correlation potential $\mu_{xc}(\mathbf{r})$, $\rho(\mathbf{r})$ is exactly the same as solving the single-particle Schrödinger-like equation (Kohn-Sham equation) of the non-interacting electrons moving in the effective potential V_{eff},

$$\Big[-\frac{1}{2}\nabla^2 + V_{eff}(\mathbf{r}) \Big] \psi_i(\mathbf{r}) = \epsilon_i \psi_i(\mathbf{r}) \tag{2.9}$$

Defining

$$\rho(\mathbf{r}) = \sum_i^{occ} |\psi_i(\mathbf{r})|^2, \tag{2.10}$$

the effective potential V_{eff} is given by

$$V_{eff}(\mathbf{r}) = v(\mathbf{r}) + \int d\mathbf{r} \ \frac{\rho(\mathbf{r})}{|\mathbf{r} - \mathbf{r}'|} + \mu_{\rm xc}(\mathbf{r}) \ . \tag{2.11}$$

2.1.3 Local (spin) density approximation

In the KS scheme, the only unknown term is the exchange-correlation potential $\mu_{\rm xc}(\mathbf{r})$ In fact, all the complicated physics in the interacting system can thus be replaced by finding $E_{\rm xc}[\rho]$, of which an exact formal expression not known. The simplest and most used approximation proved to give remarkably accurate results in a variety of systems is the local density approximation (LDA).[3] The idea is that to use the exchange-correlation energy density of homogeneous electron gas, $\varepsilon_{\rm xc}$, which depends only on the local density, $\rho(\mathbf{r})$. Then, the corresponding exchange-correlation energy is

$$E_{\rm xc}[\rho] \simeq \int d\mathbf{r} \ \rho(\mathbf{r}) \varepsilon_{\rm xc}(\rho(\mathbf{r})), \tag{2.12}$$

and the exchange-correlation potential $\mu_{\rm xc}(\mathbf{r})$ becomes

$$\mu_{\rm xc}(\mathbf{r}) = \frac{d}{d\rho}\Big[\rho\,\varepsilon_{\rm xc}(\rho)\Big]. \tag{2.13}$$

In practical calculations, we adopted LDA formulated by Hedin-Lundqvist.[3] The generalization to spin-polarized systems is the local spin density approximation (LSDA), formulated by von Barth and Hedin,[26] which is spin-polarized version of Hedin-Lundqvist. In Hedin and Lundqvist result, the $\varepsilon_{\rm xc}$ is divided into two term,

$$\varepsilon_{\rm xc}(\rho) = \varepsilon_{\rm x}(\rho) + \varepsilon_{\rm c}(\rho). \tag{2.14}$$

Here $\varepsilon_{\rm x}$ describes only the exchange term and can be determined by applying the Hartree-Fock method[27] to the homogeneous electron gas,[28]

$$\varepsilon_{\rm x}(\rho) = -\frac{3e^2}{4\pi}(3\pi^2\rho)^{1/3}. \tag{2.15}$$

The correlation energy, $\varepsilon_{\rm c}$, is given by

$$\varepsilon_{\rm c}(\rho) = -C\frac{e^2}{a_0}\,F(x), \tag{2.16}$$

$$F(x) = (1+x^3)\,\ln(1+\frac{1}{x}) + \frac{x}{2} - x^2 - \frac{1}{3}\,. \tag{2.17}$$

where $C = 0.0225$, a_0 is the Bohr radius, and

$$x = \frac{r_s}{21a_0}. \tag{2.18}$$

r_s is the so-called screening radius,

$$r_s = \left(\frac{3}{4\pi\rho}\right)^{1/3}. \tag{2.19}$$

For LSDA, the exchange-correlation energy density is described by two variables, the charge density $\rho(\mathbf{r}) = \rho_\uparrow(\mathbf{r}) - \rho_\downarrow(\mathbf{r})$, and the spin density ζ, defined as $\zeta \equiv [\rho_\uparrow(\mathbf{r}) -$

$\rho_\downarrow(\mathbf{r})]/\rho(\mathbf{r})$. Then the exchange-correlation energy density $\varepsilon_{\rm xc}$ is given for paramagnetic (P) and ferromagnetic (F) cases as

$$\varepsilon_{\rm xc}(\rho,\zeta) = \varepsilon_{\rm xc}^P(\rho) + [\,\varepsilon_{\rm xc}^F(\rho) - \varepsilon_{\rm xc}^P(\rho)\,]f(\zeta), \tag{2.20}$$

$$f(\zeta) = \frac{(1+\zeta)^{4/3} + (1-\zeta)^{4/3} - 2}{2^{4/3} - 2}. \tag{2.21}$$

The exchange part for spin-polarized case is given by

$$\varepsilon_{\rm xc}^F(\rho) = 2^{1/3}\,\varepsilon_{\rm xc}^P(\rho), \tag{2.22}$$

and the correlation part is given by

$$\varepsilon_{\rm c}^i(\rho) = -C^i\,F\Big(\frac{r_s}{r^i}\Big), \quad i = P, F \tag{2.23}$$

where $F(x)$ is given in Eq. (2.17). The numerically fitted parameters by Hedin and Lundqvist are

$$C^P = 0.0225 \tag{2.24}$$

$$C^F = 0.01125$$

$$r^P = 21$$

$$r^F = 53.$$

2.2 FLAPW

2.2.1 Basis functions

The computational method employed in this thesis is the full-potential linearized augmented plane wave (FLAPW)[14,15] method, one of the most accurate and powerful schemes

to solve Kohn-Sham equations, based on the linearized augmented plane wave (LAPW) method.[29] It has been widely used and successful to determine the ground state properties of solid, *e.g.* the electronic band structure, charge and spin densities, atomic core levels, the Fermi contact hyperfine magnetic field, and the ground state structure obtained by the atomic force. The FLAPW method in the slab geometry and here, also provides accurate surface and magneto-optical properties such as the surface reconstructions, work function of metals, molecular chemisorptions, MOKE (magnetic-optical Kerr effect), and MCD (magnetic circular dichroism).

In FLAPW, the single-particle Bloch wave function, $\psi_i(\mathbf{k}, \mathbf{r})$ is expanded in linearized augmented plane wave basis functions, $\phi(\mathbf{k} + \mathbf{G}, \mathbf{r})$, as

$$\psi_i(\mathbf{k}, \mathbf{r}) = \sum_{\mathbf{G}} C_i(\mathbf{k} + \mathbf{G})\ \phi(\mathbf{k} + \mathbf{G}, \mathbf{r}), \tag{2.25}$$

where i is band index, and $\mathbf{k}$ lies in the first Brillouin zone. The unit cell is divided into three regions, as illustrated in Fig. 2.1; namely muffin-tin (MT) sphere around the nuclei, a vacuum region on each side of the slab, and the remaining interstitial region. The basis functions $\phi(\mathbf{k} + \mathbf{G}, \mathbf{r})$ is given in different forms in the three different region as,

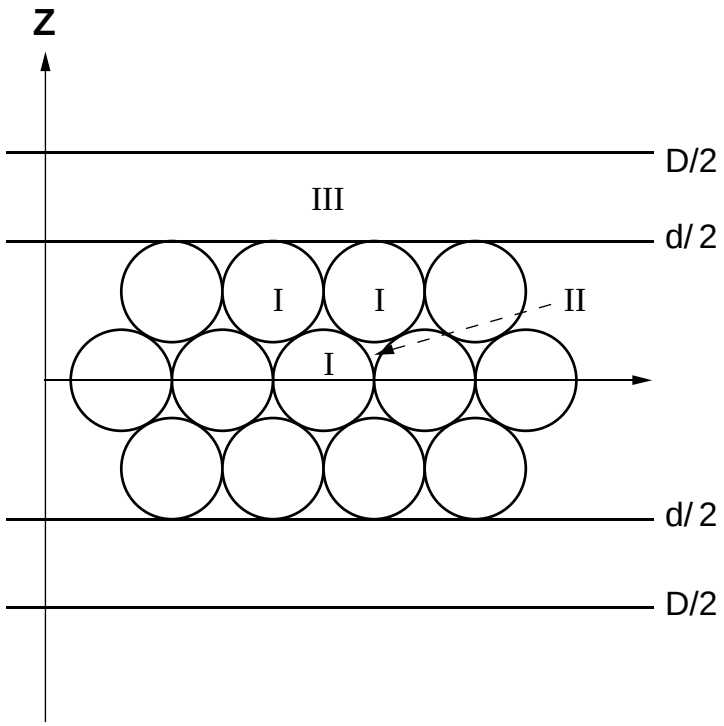

Figure 2.1: Slab geometry. I is the MT sphere, II is the interstitial and III is the vacuum region. The unit cell is defined by D while the interstitial - vacuum boundary is defined by d.

$$\phi(\mathbf{k}+\mathbf{G},\mathbf{r}) = \begin{cases} \Omega^{-1/2}\exp[i(\mathbf{k}+\mathbf{G})\cdot\mathbf{r}], & \mathbf{r}\in \texttt{interstitial} \\ \sum_L \left[A_L(\mathbf{k}+\mathbf{G})u_l(E_l,r)\right. & \\ \left.+B_L(\mathbf{k}+\mathbf{G})\dot{u}_l(E_l,r)\right]Y_L(\hat{\mathbf{r}}), & \mathbf{r}\in \texttt{MT sphere} \\ \Big[A_v(\mathbf{k}+\mathbf{G})u_{\mathbf{k}_\parallel+\mathbf{G}_\parallel}(E_v,z) & \\ +B_v(\mathbf{k}+\mathbf{G})\dot{u}_{\mathbf{k}_\parallel+\mathbf{G}_\parallel}(E_v,z)\Big]\exp[i(\mathbf{k}_\parallel+\mathbf{G}_\parallel)\cdot\mathbf{r}_\parallel], & \\ & \mathbf{r}\in \texttt{vacuum.} \end{cases} \tag{2.26}$$

The z component of $\mathbf{G}$ is defined in terms of the slab thickness D, as shown in Fig. 2.1; Ω is the volume of unit cell. The radial function, $u_l(E_l,r)$, is the solution of the radial Schrödinger equation with effective potential at a fixed energy E_l in each muffin-tin sphere, i.e.

$$\frac{1}{r}\frac{d^2}{dr^2}[ru_l] - \frac{l(l+1)}{r^2}u_l + 2(E_l - V)u_l = 0, \tag{2.27}$$

and the $\dot{u}_l(E_l,r)$, which is the energy derivative of u_l, satisfies

$$\frac{1}{r}\frac{d^2}{dr^2}[r\dot{u}_l] - \frac{l(l+1)}{r^2}\dot{u}_l + 2(E_l - V)\dot{u}_l + 2u_l = 0, \tag{2.28}$$

where u_l is normalized, and $\dot{u}_l$ is required to be orthogonal to u_l:

$$\int_0^{R_{MT}} r^2 u_l^2 dr = 1 \tag{2.29}$$

$$\int_0^{R_{MT}} r^2 u_l\, \dot{u}_l dr = 0\ , \tag{2.30}$$

where R_{MT} is the muffin-tin radius. In the vacuum region, the basis function $u_{\mathbf{k}_\parallel+\mathbf{G}_\parallel}$ and $\dot{u}_{\mathbf{k}_\parallel+\mathbf{G}_\parallel}$ are solutions of one-dimensional Schrödinger equation and its energy derivative,

respectively:

$$[\quad \frac{\partial^2}{\partial z^2} + 2(E_v - V(z) - (\mathbf{k}_\parallel + \mathbf{G}_\parallel)^2)]u_{\mathbf{k}_\parallel+\mathbf{G}_\parallel} = 0, \tag{2.31}$$

$$[\quad \frac{\partial^2}{\partial z^2} + 2(E_v - V(z) - (\mathbf{k}_\parallel + \mathbf{G}_\parallel)^2)]\dot{u}_{\mathbf{k}_\parallel+\mathbf{G}_\parallel} + 2u_{\mathbf{k}_\parallel+\mathbf{G}_\parallel} = 0. \tag{2.32}$$

The A_L and B_L, as well as A_v and B_v are determined by matching boundary conditions of the basis function $\phi(r)$ and its derivative $\partial\phi/\partial r$ across the sphere and the vacuum boundary. In practice, these u_l and $\dot{u}_l$ for MT regions are solved scalar-relativistically, while for vacuum region they are obtained by solving one-dimensional Schrödinger equation, Eq. (2.31) and (2.32). With these FLAPW bases, the wave functions are expressed as in Eq. (2.25). The coefficients, $C_i(\mathbf{k} + \mathbf{G})$, are determined by solving the secular equation;

$$\sum_{\mathbf{G}'}[H_{\mathbf{G},\mathbf{G}'} - \epsilon_i(\mathbf{k})S_{\mathbf{G},\mathbf{G}'}]C_i(\mathbf{k} + \mathbf{G}') = 0, \tag{2.33}$$

where $H_{\mathbf{G},\mathbf{G}'}$ is the Hamiltonian matrix in the Kohn-Sham equation and $S_{\mathbf{G},\mathbf{G}'}$ is the overlap matrix.

The important feature of the LAPW method is that the Hamiltonian and the overlap matrix in Eq. (2.33) are energy independent due to this linearization scheme using $\dot{u}_\ell$. The secular equation can be solved by diagonalizing once to get the eigenvalues and eigenfunctions simultaneously.

2.2.2 Representations

In constructing the Hamiltonian, the charge density and the effective potential, "natural" representations are used for each of three spatial regions. The contribution of the core electrons is assumed to be of spherical symmetry, thus is expressed as a simple radial function.

The valence electrons are expressed in a most general way and no shape approximation is made.

Inside the MT sphere, the charge density and the effective potential are expressed as the radial expression of the lattice harmonics, K_ν,

$$\rho_\alpha(\mathbf{r}) = \sum_\nu \rho_\nu(r_\alpha) K_\nu(\hat{\mathbf{r}}) - Z_\alpha \delta(\hat{\mathbf{r}}), \tag{2.34}$$

where Z_α is the total charge of the α-th nucleus and the lattice harmonics, K_ν, is given as

$$K_\nu(\mathbf{r} - \mathbf{R}_\alpha) = \sum_l c^\nu_{l,m} Y_{l,m}(\mathbf{r} - \mathbf{R}_\alpha), \tag{2.35}$$

for each inequivalent atom α at $\mathbf{R}_\alpha$, which are constructed for the local site symmetry from the spherical harmonics.[a] The coefficient $c^\nu_{l,m}$ is determined by requiring the lattice harmonics to be real and orthogonal. The K_ν's satisfy orthogonality in ν,

$$\int d\Omega K_\nu(\hat{\mathbf{r}}_\alpha) K_{\nu'}(\hat{\mathbf{r}}_\alpha) = \delta_{\nu,\nu'} \tag{2.36}$$

In the interstitial region, the charge density is expressed as an expansion of the *star* functions, Φ_s,

$$\rho(\mathbf{r}) = \sum_{\mathbf{G}_s} \rho_{\mathbf{G}_s} \Phi_{\mathbf{G}_s}(\mathbf{r}), \tag{2.37}$$

where the stars is defined to ensure the space group symmetry as

$$\Phi_{\mathbf{G}_s}(\mathbf{r}) = \frac{1}{N_G} \sum_{\hat{R}} e^{i\hat{R}\mathbf{G}_s \cdot (\mathbf{r} - \mathbf{t}_{\hat{R}})} \tag{2.38}$$

where $\hat{R} \equiv \{\hat{R}|\mathbf{t}_{\hat{R}}\}$ is the space group operation, N_G is the total number of the space group operations, and $\mathbf{G}_s$ is the star representative reciprocal vector.

[0a] Factor 2 in front of delta function is found in Eq. 2.34 in some literature, where Rydberg is used for the energy unit. In Hartree units, Eq. 2.34 is the correct expression for lattice harmonics.

In the vacuum region, the charge density is expressed in terms of the corresponding star functions

$$\rho^{vac}(\mathbf{r}) = \sum_{\mathbf{G}_\parallel} n^{vac}_{\mathbf{G}_\parallel}(z) n_{\mathbf{G}_\parallel} \Phi_{\mathbf{G}_\parallel}(\mathbf{r}) \tag{2.39}$$

where

$$\Phi_{\mathbf{G}_\parallel}(\mathbf{r}) = \frac{1}{n_0^{(2)}} \sum_{\hat{R}_\parallel} e^{i\hat{R}_\parallel \mathbf{G}_\parallel \cdot (\mathbf{r} - \mathbf{t}_{\hat{R}_\parallel})}, \tag{2.40}$$

and $\mathbf{G}_\parallel$ is the two-dimensional star representative reciprocal vector, and the $n_0^{(2)}$ is the order of the two-dimensional space group, $\{\hat{R}_\parallel | \mathbf{t}_{\hat{R}_\parallel}\}$.

The classical Coulomb potential, $V_C(\mathbf{r})$, in the unit cell, is obtained by solving the Poisson equation,

$$-\nabla^2 V_C(\mathbf{r}) = 4\pi\rho(\mathbf{r}), \tag{2.41}$$

separately for the three regions. In the case of the slab geometry, the potential at infinity is set equal to zero. The above Poisson equation is diagonal in reciprocal space, but the difficulty lies in a slowly convergent Fourier expansion of the MT charge density due to the large oscillation near the nuclei. Thus, the true charge density inside MT spheres is replaced with a pseudo-charge density with the same multipole moments but with a rapidly convergent Fourier expansion.[30]Then, the potential inside the spheres is obtained by solving the boundary-value problem using the true charge density inside the MT. The exchange-correlation potential given by the real space charge density is added as in Eq. (2.15) or Eq.((2.20)).

The core states are calculated fully relativistically and updated at each iteration to achieve self-consistent density, whereas the valence states are treated semi-relativistically. After obtaining the self-consistent charge density and wave functions, the spin-orbit inter-

action is applied in the usual perturbative way to obtain the relativistic band structure.

2.3 sX-LDA method

Despite its successes in the description of electronic structures, LDA is well-known for several shortcomings: among them one of the most serious is band-gap failure. There have been many attempts to overcome this band-gap problem. The screened-exchange (sX-LDA) is one of these methods.

In the generalized Kohn-Sham (GKS) scheme,[16] it can be shown that the sX-LDA method satisfies the variational principle, hence the corresponding Kohn-Sham single-particle equation is obtained as

$$\Big[\frac{-\hbar^2}{2m}\nabla^2 + V_{eff}(\mathbf{r})\Big]\psi_i(\mathbf{r}) + \int d\mathbf{r}' v_{\rm sx}^{NL}(\mathbf{r},\mathbf{r}')\psi_i(\mathbf{r}') - v_{\rm sx}^{L}(\mathbf{r})\psi_i(\mathbf{r}) = \epsilon_i^{\rm sx}\psi_i(\mathbf{r}), \quad (2.42)$$

where $V_{eff}(\mathbf{r})$ is the effective potential formulated by LDA, and $v_{\rm sx}^{NL}(\mathbf{r},\mathbf{r}')$ and $v_{\rm sx}^{L}(\mathbf{r})$ are non-local and and local screened exchange potentials, respectively.

In sX-LDA, a GKS equation is given by-invoking perturbation theory as

$$(\hat{h}^{LDA} + \Delta\hat{v}_{\rm sx})\psi_i(\mathbf{r}) = \epsilon_i^{\rm sx}\psi_i(\mathbf{r}), \quad (2.43)$$

where

$$\Delta\hat{v}_{\rm sx} = \hat{v}_{\rm sx}^{NL} - \hat{v}_{\rm sx}^{L}, \quad (2.44)$$

$\hat{h}^{LDA}$ is the LDA Hamiltonian, $\hat{v}_{\rm sx}^{NL}$ the non-local screened Fock operator, $\hat{v}_{\rm sx}^{L}$ the corresponding local one, and $\psi_i(\mathbf{r})$ is the sX-LDA wave-function. The local screened exchange potential is subtracted so that this potential which is also in the LDA Hamiltonian, is not

double counted. The screened Fock exchange operator is given as

$$v_{\rm sx}^{NL}(\mathbf{r},\mathbf{r}') = -\sum_{j}^{occ} W(\mathbf{r},\mathbf{r}')\langle\mathbf{r}|j\rangle\langle j|\mathbf{r}'\rangle \tag{2.45}$$

where summation is over occupied states of the valence electrons. For screening, in the current sX-LDA method, simple Thomas-Fermi screening is employed for $\Delta\hat{v}_{\rm sx}$,

$$W(r) = \frac{e^{-k_{\rm TF}r}}{r}, \tag{2.46}$$

and the corresponding local potentials are

$$v_{\rm sx}^{L}[\rho(\mathbf{r})] = -2\Big(\frac{3}{\pi}\rho\Big)^{1/3} F(\gamma), \tag{2.47}$$

$$F(\gamma) = 1 - \frac{4}{3}\gamma \arctan\frac{2}{\gamma} - \frac{\gamma^2}{6}\Big[1 - (\frac{\gamma^2}{4}+3)\ln(1+\frac{4}{\gamma^2})\Big]. \tag{2.48}$$

Here $\gamma = k_{TF}/q_F$, and k_{TF} is a Thomas-Fermi screening wave vector, and q_F is a Fermi wave vector corresponding to the average density, $\bar{\rho}$. It should be noted here, as discussed in Bylander and Kleinman[4] and Asahi,[6] that it is assumed that the *local* screened exchange density functional has the same dependence on the local density as the LDA exchange functional, thus γ has no dependence on $\rho(\mathbf{r})$ and q_F depends only on $\bar{\rho}$. The detail of the sX-LDA method can be found in Asahi[6] and Ye.[31]

2.4 Explicit Orthogonalization

In the LAPW method, the linearization energy E_ℓ defined in Eq. (2.27) is chosen to be the center of bands of interest. However, for some cases this choice does not give satisfactory results, where there is no single choice of E_ℓ. There are highly lying and extended core states, especially in $4f$ and early transition metal elements and compounds. Such states

are called “semi-core states”, which yield typically ghost bands and makes calculations unreliable. Many attempts were devoted to resolve this problem, such as multiple windows and local-orbital methods. However, “explicit orthogonalization”(XO) was suggested by Weinert,[17] in which an explicit orthogonalization of basis functions to the core states is enforced . The basic idea of the XO method is to modify the energy derivative $\dot{u}_\ell$ to be explicitly orthogonal to the core states. Thus, in constructing basis functions, the radial function u_ℓ is kept the same as without XO, while the energy derivatives, $\dot{u}_\ell$ is modified as

$$|\tilde{\dot{u}}_\ell\rangle = |\dot{u}_\ell\rangle + \alpha|\phi_c\rangle + \beta|u_\ell\rangle \quad , \tag{2.49}$$

and explicit orthogonalization to core states enforces $\langle\tilde{\dot{u}}_\ell|\phi_c\rangle = 0$ and $\langle\tilde{\dot{u}}_\ell|u_\ell\rangle = 0$, where $|\phi_c\rangle$ are the core states. The coefficients, α and β, for this modified energy derivative $\tilde{\dot{u}}_\ell$ are

$$\alpha = -\frac{\langle\phi_c|\dot{u}_\ell\rangle}{\langle\phi_c|\phi_c\rangle - \langle\phi_c|u_\ell\rangle^2} \quad , \tag{2.50}$$

$$\beta = -\alpha\langle u|\phi_c\rangle \quad . \tag{2.51}$$

So the new energy derivative, $\tilde{\dot{u}}_\ell$ is

$$|\tilde{\dot{u}}_\ell\rangle = |\dot{u}_\ell\rangle - \frac{\langle\phi_c|\dot{u}_\ell\rangle}{\langle\phi_c|\phi_c\rangle - \langle\phi_c|u_\ell\rangle^2}\Big(|\phi_c\rangle - \langle u_\ell|\phi_c\rangle|u_\ell\rangle\Big). \tag{2.52}$$

Since one of the basis functions for the MT region is completely changed, it is worthwhile to check the effects on the Hamiltonian and overlap matrices.

As a first step, we check the action of muffin-tin Hamiltonian $\hat{h}_{MT}$ on u_ℓ and $\dot{u}_\ell$, which yields the following equations:

$$\hat{h}_{MT}u_\ell = E_l u_\ell \quad , \tag{2.53}$$

$$\hat{h}_{MT}\dot{u}_\ell = E_l\dot{u}_\ell + u_\ell \quad , \tag{2.54}$$

where $\hat{h}_{MT}$ is Hamiltonian acting on the MT part only. Applying $\hat{h}_{MT}$ to $\tilde{\dot{u}}_\ell$ instead of $\dot{u}_\ell$ will yield

$$\begin{aligned}
\hat{h}_{MT}\tilde{\dot{u}}_\ell &= \hat{h}_{MT}(\dot{u}_\ell + \alpha\phi_c + \beta u_\ell) \\
&= E_l\dot{u}_\ell + u_\ell + \alpha E_c\phi_c + \beta E_l u_\ell \\
&= E_l(\dot{u}_\ell + \beta u_\ell + \alpha\phi_c - \alpha\phi_c) + u_\ell + \alpha E_c\phi_c \\
&= E_l\tilde{\dot{u}}_\ell + u_\ell + \alpha(E_c - E_l)\phi_c,
\end{aligned} \tag{2.55}$$

where E_c is the energy of core states and $\hat{h}_{MT}\phi_c = E_c\phi_c$. In Eq. (2.55), $(E_c - E_l)$ in the last term is due to introducing modified energy derivative, $\tilde{\dot{u}}_\ell$. If the original energy derivative $\dot{u}_\ell$ is already orthogonal to core states, which means $\alpha = 0$ in Eq. (2.50), the term containing $(E_c - E_l)$ vanishes. However, for semi-core states, where $\langle\phi_c|\dot{u}_\ell\rangle > 0$, the term with $(E_c - E_l)$ is not negligible. Thus, one can expect that the XO method will affect the overlap matrix and the MT part of the Hamiltonian.

First, the overlap matrix, $S(\mathbf{G}, \mathbf{G}')$, becomes

$$\begin{aligned}
&S(\mathbf{G}, \mathbf{G}') = \langle\phi(\mathbf{k}+\mathbf{G})|\phi(\mathbf{k}+\mathbf{G}')\rangle \\
&= \sum_{\ell,\ell'}\langle A_\ell(\mathbf{G})u_\ell + B_\ell(\mathbf{G})\tilde{\dot{u}}_\ell|A_{\ell'}(\mathbf{G}')u_{\ell'} + B_{\ell'}(\mathbf{G}')\tilde{\dot{u}}_{\ell'}\rangle\frac{2\ell+1}{4\pi}P_\ell(\hat{g}\cdot\hat{g}')\delta_{\ell,\ell'}\delta_{m,m'} \\
&= \sum_\ell\left[A^*_\ell(\mathbf{G})A_\ell(\mathbf{G}') + B^*_\ell(\mathbf{G})B_\ell(\mathbf{G}')\langle\tilde{\dot{u}}_\ell|\tilde{\dot{u}}_\ell\rangle\right]\frac{2\ell+1}{4\pi}P_\ell(\hat{g}\cdot\hat{g}') \ ,
\end{aligned} \tag{2.56}$$

where $\mathbf{g} = \mathbf{k} + \mathbf{G}$ and $\mathbf{g}' = \mathbf{k} + \mathbf{G}'$, respectively. Calculating $\tilde{N}_\ell \equiv \langle\tilde{\dot{u}}_\ell|\tilde{\dot{u}}_\ell\rangle$ explicitly,

$$\begin{aligned}
\tilde{N}_\ell &= \langle\tilde{\dot{u}}_\ell|\tilde{\dot{u}}_\ell\rangle \\
&= N_\ell - \frac{\langle\phi_c|\dot{u}_\ell\rangle}{\langle\phi_c|\phi_c\rangle - \langle\phi_c|u_\ell\rangle^2},
\end{aligned} \tag{2.57}$$

where $N_\ell = \langle\dot{u}_\ell|\dot{u}_\ell\rangle$ is the overlap of the original energy derivative $\dot{u}_\ell$, Therefore, the

correction in overlap matrix due to the XO method is

$$-\sum_{\ell}\frac{\langle c|\dot{u}_\ell\rangle}{\langle\phi_c|\phi_c\rangle-\langle\phi_c|u_\ell\dot{u}_\ell\rangle^2}B^*_\ell(\mathbf{G})B_\ell(\mathbf{G}')\frac{2\ell+1}{4\pi}P_\ell(\hat{g}\cdot\hat{g}') \ . \tag{2.58}$$

Second, to see changes in Hamiltonian due to XO basis, we operate on the MT-Hamiltonian $\hat{h}_{MT}$, i.e. $\langle\phi(\mathbf{k}+\mathbf{G})|\hat{h}_{MT}|\phi(\mathbf{k}+\mathbf{G}')\rangle$. By manipulation of Eq. (2.55) and some algebra, we get

$$\begin{aligned}
&\langle\phi(\mathbf{k}+\mathbf{G})|\hat{h}_{MT}|\phi(\mathbf{k}+\mathbf{G}')\rangle \qquad (2.59)\\
=\ &\sum_{\ell}\left[\Big[A^*_\ell(\mathbf{G})A_{\ell'}(\mathbf{G}')+B^*_\ell(\mathbf{G})B_{\ell'}(\mathbf{G}')\Big]E_l+A^*_\ell(\mathbf{G})B_\ell(\mathbf{G}')\right]\\
-\ &\sum_{\ell,\ell'}A^*_\ell(\mathbf{G})B_{\ell'}(\mathbf{G}')\frac{\langle\phi_c|\dot{u}\rangle\langle u|\phi_c\rangle}{\langle\phi_c|\phi_c\rangle-\langle\phi_c|u\rangle^2} \ ,
\end{aligned}$$

where the last term is the correction due to XO basis.

In this section, we briefly reviewed the XO method, its new definition of basis functions, its effects on overlap matrix and MT Hamiltonian. The XO method resolves the ghost band problem in a very efficient way.

Chapter 3: Optical properties of semiconductors

3.1 Introduction

Since semiconductors are important for their extensive applications as optoelectronic devices such as light emitting diodes and optosensors, it is of great importance to be able to accurately describe excitations by highly reliable and efficient *ab initio* approaches. As is well-known, density functional theory (DFT)[1,2] has proven to be a very powerful tool for determining the electronic ground-state properties in a variety of materials. Although the local density approximation (LDA) has provided detailed calculations of the optical and dielectric properties based mostly on the independent-particle approximation[32,33] its description of the excitation properties is questionable. The very well-known band gap problem of LDA is the major challenge in the *ab initio* calculation of excitation energies[34,35,36] since the optical properties determined in LDA still show large discrepancies from experiment. One approach to determine the optical properties theoretically, is to model the dielectric function by adapting critical point energies from experiment.[37] The other approach uses the scissor approximation[38,39] which displaces the eigenvalues of the unoccupied states by a rigid energy shift. The problem with this approximation is to find a more or less proper way to choose the shift of energy: one can adjust the eigenvalues

so that the main peak of the imaginary part of the dielectric function corresponds to the transition energy $X_5^v \rightarrow X_1^c$ without spin-orbit coupling (SOC), or the $X_7^v \rightarrow X_6^c$ transition with SOC[39] The resulting peak position is obtained considering only one *k* point in the Brillouin zone while the true contribution is rather spread out in the Brillouin zone.[40] Thus, it is also questionable whether the resulting eigenvalues thus shifted at other *k* points are the same as the experimental band structure. On the other hand, direct quasi-particle energies are available within the GW approximation[41] and $\varepsilon_2(\omega)$ of Si was determined including excitonic and local-field effects by the GW approximation[42] It was also shown that the existence of non-locality in the self-energy makes the relation $\mathbf{v} = \mathbf{p}/m$ incorrect to ensure gauge invariance and charge conservation[39,43] Although the GW approximation removes most of the problems of LDA in treating excitation properties, its heavy computational demands have hampered determining properties self-consistently. A simplification of the GW approximation, called the model GW[44,45] was proposed to reduce the numerical efforts associated with the GW approximation. The model GW has generally shown good agreement with experiment for nonmagnetic semiconductors using the pseudopotential method[44] and for transition-metal oxides[45,46] using the all-electron full-potential linearized augmented plane wave (FLAPW) method. Although the model GW method is a promising scheme for various applications, the reliability of the calculated total energy, and therefore, the ground states has not been clearly shown. The recently proposed screened-exchange LDA method[4,16] (sX-LDA) is one of the theories designed to find a better energy functional beyond LDA by modeling the exchange-correlation hole within *nonlocal* density schemes. The sX-LDA demonstrated encouraging results for the band gaps and structural properties of semiconductor materials with the plane-wave pseudopotential method[16]

and the FLAPW method.[47] In particular, lattice constants obtained for Si, Ge, and GaAs show[16] better agreement with experiment than LDA, which indicates the ground states of sX-LDA are expected to be better than those of LDA. The advantage of sX-LDA over the GW approximation is that it is much less computationally demanding and it also enables the self-consistent determination of the ground state and excited properties and with full matrix elements for the optical properties. The recent work with sX-LDA using FLAPW demonstrates very successful descriptions of excited states for pure semiconductors,[5] III-V semiconductors[48] and heterostructure.[49] The linear optical properties of Si, Ge, GaAs, and InSb was determined using self-consistent sX-LDA calculations,[5,6] as implemented in the FLAPW method with no adjustable parameters. Most recently, the sX-LDA approach has been successfully extended to the treatment of surfaces/interfaces and multi-layers.[49] In this chapter, we report results of self-consistent sX-LDA plus spin-orbit coupling (SOC) calculations as implemented in the FLAPW method for the narrow band gap materials InAs, InSb, GaSb and AlSb. With self-consistent eigenvalues and wave-functions and using the independent-particle approximation and no artificial parametrization, we determine the linear optical properties for these materials, namely the imaginary dielectric function, $\varepsilon_2(\omega)$, the index of refraction, $n(\omega)+ik(\omega)$, the reflectivity, $R(\omega)$, and the absorption coefficients, $\alpha(\omega)$, and make comparisons with experiment. We also demonstrate critical point energies obtained from the self-consistent sX-LDA plus SOC method which reveals the expected great improvement over the LDA.

3.2 Optical properties in sX-LDA

Optical properties, such as the imaginary part of the dielectric function, index of refraction, reflectivity and absorption coefficient, [$\varepsilon_2(\omega)$,$n(\omega)$, $k(\omega)$, $R(\omega)$,$\alpha(\omega)$] of some III-V semiconductors (InAs, InSb, GaSb, and AlSb), are determined using the highly precise full-potential linearized augmented plane wave (FLAPW) method with the screened-exchange local density approximation (sX-LDA) solved self-consistently and with spin-orbit coupling included. Here $\varepsilon_2(\omega)$ is calculated using the longitudinal expression with full $e^{i\mathbf{q}\cdot\mathbf{r}}$ matrix elements, due to the non-locality of the potential in the sX-LDA method, and its structure is analyzed with band structures and consideration of interband transitions. The critical point(CP) energies are also studied in comparison with experiment. The results of these fully first-principles calculations (no scissor operator or semi-empirical inputs) show good agreement of the peak positions in $\varepsilon_2(\omega)$, $n(\omega)+ik(\omega)$, $R(\omega)$, $\alpha(\omega)$ and critical point energies with experiments.

For our calculations, we employ the highly precise *ab initio* electronic structure FLAPW method with no artificial shape approximation for the wave functions, charge densities, and potentials. At first, the LDA-FLAPW is performed with the exchange-correlation potential using the Hedin-Lundqvist parametrization[3] and cutoffs of the plane-wave basis (3.6 a.u. for InSb and 3.3 a.u. for the rest) and potential representation 8.0 a.u., and the expansion in terms of spherical harmonics with $\ell \leq 8$ inside the muffin-tin (MT) spheres. We used the experimental lattice constants for all materials: 11.45 (InAs), 12.24 (InSb), 11.51 (GaSb) and 11.59 (AlSb) in atomic units. With the converged LDA results, we performed sX-LDA plus spin-orbit coupling (SOC) calculations self-consistently with cut-off parameters of 3.1 a.u. in the wave vectors and $\ell \leq 4$ inside the MT spheres. Only s and p electrons

were included in the screening. Summation over the Brillouin zone were done using ten special *k* points[50] in the irreducible wedge. Core states are treated fully relativistically and updated at each iteration, while the valence states are treated semi-relativistically.

For the calculation of optical properties, the linear electronic response to a longitudinal external perturbation is described in the independent-particle approximation, or the random-phase approximation (RPA), by the dielectric matrix,

$$\varepsilon(\mathbf{q}+\mathbf{G},\mathbf{q}+\mathbf{G}',\omega) = \delta_{\mathbf{G},\mathbf{G}'} - V(\mathbf{q}+\mathbf{G})\chi_0(\mathbf{q}+\mathbf{G},\mathbf{q}+\mathbf{G}',\omega), \tag{3.1}$$

with $V(\mathbf{q}) = 4\pi e^2/q^2$, the Fourier representation of the Coulomb potential, and χ_0, the polarization function of the independent-particle. Neglecting local-field effects, the imaginary part of the dielectric function in the long-wavelength limit, $q \to 0$, is written as

$$\varepsilon_2(\omega) = \frac{8\pi^2 e^2}{\Omega} \lim_{q\to 0} \sum_{c,v} \sum_{\mathbf{k}} \frac{1}{q^2} |\langle c, \mathbf{k}+\mathbf{q}|e^{i\mathbf{q}\cdot\mathbf{r}}|v,\mathbf{k}\rangle|^2 \cdot \delta[E_c(\mathbf{k}+\mathbf{q}) - E_v(\mathbf{k}) - \hbar\omega], \tag{3.2}$$

where *c* and *v* denote conduction- and valence-band, respectively. The direction of $\mathbf{q}$ defines one of the diagonal elements of the dielectric tensor, $\epsilon_{\alpha\alpha}$, which are all equal for cubic crystals. Taking the trace, therefore, makes it possible to restrict the calculations to the irreducible Brillouin zone (IBZ) defined by the crystal symmetry group. If we use the relation $\mathbf{p}/m = \frac{i}{\hbar}[H,\mathbf{r}]$, Eq. (3.2) is expressed as

$$\varepsilon_2(\omega) = \frac{8\pi^2 e^2}{\omega^2 m^2 \Omega} \sum_{c,v} \sum_{\mathbf{k}} |\langle c,\mathbf{k}|\hat{\mathbf{e}}\cdot\mathbf{p}|v,\mathbf{k}\rangle|^2 \cdot \delta[E_c(\mathbf{k}) - E_v(\mathbf{k}) - \hbar\omega], \tag{3.3}$$

The calculation using the transverse expression [Eq.(3.3)], is much faster than using Eq.(3.2) since only wave functions at the same $\mathbf{k}$-points of the conduction and valence bands are needed instead of pairs at $\mathbf{k}$ and $\mathbf{k}+\mathbf{q}$. However, as pointed out by Del Sole *et al.*,[39] Strace,[43] and Levine *et al.*,[51] Eq. (3.3) is not correct when the Hamiltonian includes

nonlocal potentials, as in the case of the sX-LDA method. Rather than the momentum operator, one needs to use the velocity operator defined by the Heisenberg equation of motion,

$$\mathbf{v} = \frac{d\mathbf{r}}{dt} = \frac{i}{\hbar}[H, \mathbf{r}] = \frac{\mathbf{p}}{m} + \frac{i}{\hbar}[v_{sx}^{\mathrm{NL}}(\mathbf{r}, \mathbf{r}'), \mathbf{r}]. \tag{3.4}$$

Due to the non-locality of the Hamiltonian with the sX-LDA approach, the gauge invariance requires the light-matter interaction in terms of $\mathbf{v}\cdot\mathbf{A}$ instead of $\mathbf{p}\cdot\mathbf{A}$,[43] since the transverse expression, Eq. (3.3), does not satisfy gauge invariance or equivalently charge conservation. Then it is easy to show that the dipole transition probability is equivalent to the longitudinal expression, Eq.(3.2), in the long-wavelength limit through the relation

$$i\langle c|[H, \mathbf{r}]|v\rangle = \lim_{q\to 0}(\frac{1}{q})(E_c - E_v)\langle c|e^{i\mathbf{q}\cdot\mathbf{r}}|v\rangle. \tag{3.5}$$

In other words, Eq.(3.2) is appropriate whether the Hamiltonian is local or not, and so in this work the longitudinal expression [Eq.3.2] is employed. We calculated the optical properties using the self-consistent eigenvalues and wave functions obtained with the sX-LDA plus spin-orbit interaction. Once $\varepsilon_2(\omega)$ is obtained, we obtain the real part, $\varepsilon_1(\omega)$, by the Kramers-Kronig relation. Other quantities, the index of refraction $[n(\omega) + ik(\omega)]$, the reflectivity $[R(\omega)]$, and the absorption coefficient $[\alpha(\omega)]$, are obtained by the relations.[52]

$$\begin{aligned} \varepsilon_1(\omega) &= n(\omega)^2 - k(\omega)^2, \quad \varepsilon_2(\omega) = 2\, n(\omega)\, k(\omega), \\ R(\omega) &= \frac{[n(\omega)-1]^2 + k(\omega)^2}{[n(\omega)+1]^2 + k(\omega)^2}, \\ \alpha(\omega) &= \frac{2\omega k(\omega)}{c}. \end{aligned} \tag{3.6}$$

Band Gap	InAs	InSb	GaSb	AlSb	
				Indirect	Direct
LDA	-0.51[53]	-0.47[53]	-0.09	1.06	1.41
sX-LDA + SOC	0.35	0.11	0.43	1.53	2.11
Experiment[54]	0.42	0.24	0.82	1.69	2.38

Table 3.1: Band gaps (in eV) by LDA, sX-LDA plus SOC and experiment.

InAs	E_0	$E_0+\Delta_0$	E_0'	E_1	$E_1+\Delta_1$	E_2
LDA	-0.51		3.50	1.57		3.54
sX-LDA plus SOC	0.36	0.75	4.21	2.55	2.83	4.61
Expt.(Spitzer *et al*[55])	0.42[54]		4.50	2.49	2.78	4.70
Adachi[37]	0.36	0.76		2.50	2.78	4.45

Table 3.2: Critical-Point energies(in eV) for InAs.

InSb	E_0	$E_0+\Delta_0$	E_0'	E_1	$E_1+\Delta_1$	E_1'	E_2
LDA	-0.47		2.79	1.33		4.72	3.44
sX-LDA plus SOC	0.11	0.97	2.88	1.86	2.39	5.09	4.13
Expt.(Spitzer *et al*[55])	0.23[54]		3.20	1.88	2.38		4.10
Adachi[56]	0.18	0.99	3.26	1.80	2.30	5.11	3.85

Table 3.3: Critical-Point energies (in eV) for InSb.

GaSb	E_0	$E_0+\Delta_0$	E_0'	E_1	$E_1+\Delta_1$	E_2
LDA	-0.09		2.71	1.44		3.41
sX-LDA plus SOC	0.43	1.23	3.04*	1.95	2.41	4.00
Expt.(Muñoz[57])	0.73	1.52	3.40	2.04	2.49	4.10
Adachi[37]	0.72	1.46		2.05	2.50	4.00

Table 3.4: Critical-Point energies (in eV) for GaSb. $*\ \Gamma_8^v \rightarrow \Gamma_8^c$ transition is considered.

	E_0	E_0'	E_1	$E_1+\Delta_1$	E_1'	E_2
LDA	1.41	3.05	2.39		3.53	3.29
sX-LDA plus SOC	2.11	3.44	2.67	3.09	5.06	3.86
Expt.(Spitzer[55])		3.70	2.81	3.21		4.30
Expt.(Zollner *et al*[58])	2.27	3.76	2.84	3.23	5.30	4.23

Table 3.5: Critical-Point energies (in eV) for AlSb.

3.3 Results

In Table 3.1, we list calculated band gaps of InAs, InSb, GaSb, and AlSb with LDA and sX-LDA plus spin-orbit coupling and compare with experiment. While LDA gives negative band gaps for InAs, InSb and GaSb, the sX-LDA plus SOC gives great improvement for the band gaps of these three materials. In addition, the sX-LDA plus SOC shows improvement not only for these direct band gap materials but also for indirect band gap materials for both their indirect and direct band gap, as is the case of AlSb. In the following subsections, we present band structures, imaginary dielectric constants, indices of refraction, reflectivity and absorption coefficients of InAs, InSb, GaSb and AlSb. Also we discuss the CP energies obtained from sX-LDA plus SOC in comparison with CP energies from LDA, experiment and theoretical modeling by Adachi[37,56]. Adachi considered the following transition data from works by Aspnes *et al*[59] and Seraphin *et al*:[60] $\Gamma_8^v \rightarrow \Gamma_6^c(E_0$ transition), $\Gamma_8^v \rightarrow \Gamma_7^c(E_0'$ transition), $L_{4,5}^v \rightarrow L_6^c(E_1$ transition), $L_6^v \rightarrow L_6^c(E_1 + \Delta_1$ transition) and $X_7^v \rightarrow X_6^c(E_2$ transition). ($L_{4,5}^v \rightarrow L_{4,5}^c(E_1'$ transition) is considered for InSb) For the description of these interband transitions, the labels follow Cardona's convention;[61] subscripts 0,1 and 2 stand for transitions at Γ, L and X in reciprocal space, respectively. Spin-orbit split energies are denoted as Δ.

3.3.1 InAs

The calculated critical-point energies are given in Table 3.3. While LDA underestimates all CP energies, the sX-LDA plus SOC gives excellent agreement with experiment. The calculated band structure of InAs, with sX-LDA plus SOC, is shown in Fig. 3.1(a) where the

important interband transitions are labeled and shown with vertical arrows. The imaginary dielectric function, $\varepsilon_2(\omega)$, is also shown in Fig. 3.1(b), which is obtained from the band structure with Eq. (3.2) using full matrix elements. Our results show a strong similarity of the peak structure with experiment. The E_2 peak, the transition from the valence band maximum(VBM) to the conduction band minimum(CBM) ($X_7^v \rightarrow X_6^c$), is 0.4 eV bigger than that of experiment. The $E_1 + \Delta_1$ peak, the transition from the spin-orbit split band to the CBM ($L_6^v \rightarrow L_6^c$) is 0.2 eV bigger than that of experiment.[59] The shift in energy of the E_1 peak is thought to arise from exciton effects not considered in our work.

Although the height is very small, our result also reproduces the E_1 peak, the transition $L_{4,5}^v \rightarrow L_6^c$.

The index of refraction is shown in Fig. 3.2. The peak positions of the real part in Fig. 3.2(a), $n(\omega)$, show the similar structure as $\varepsilon_2(\omega)$, and the extinction coefficient, $k(\omega)$, shows excellent agreement in their peak positions with experiment. Although the calculated E_1 and $E_1 + \Delta_1$ peak heights are smaller than experiment, the main E_2 peak height shows good agreement with experiment.[59]

The reflectivity and absorption coefficient are plotted in Fig. 3.3. In both cases, our results show good agreement with experiment[59] in their peak positions as well as their peak heights.

3.3.2 InSb

Figure 3.4 presents our calculated (a) band structure and (b) imaginary dielectric constant for InSb, which has a smaller band gap than does InAs. In Fig. 3.4(a), we show the interband transitions, E_0, E_1, E_2 and E_0' and spin-orbit split energy at Γ, L and X with Δ_0,Δ_1

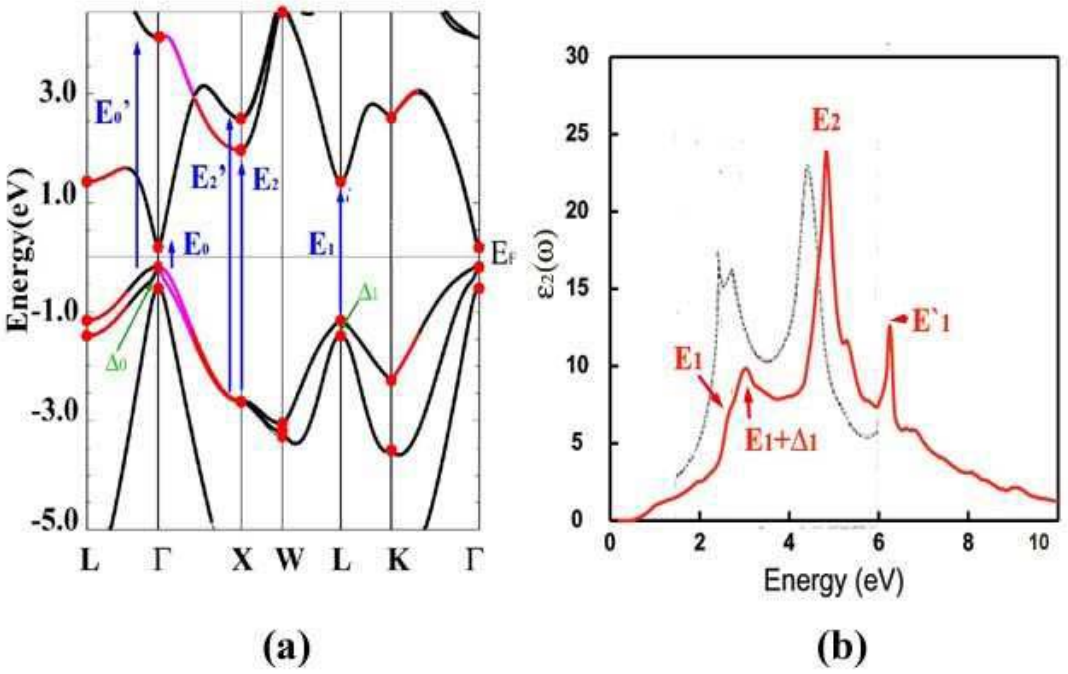

Figure 3.1: (a) Band structure of InAs. High symmetry points are shown in circles and important interband transitions are labeled as E_0 :$\Gamma_8^v \rightarrow \Gamma_6^c$, E_0' :$\Gamma_7^v \rightarrow \Gamma_7^c$, E_1:$L_{4,5}^v \rightarrow L_6^c$,$E_1 + \Delta_1$:$L_6^v \rightarrow L_6^c$,$E_2$:$X_7^v \rightarrow X_6^c$, and E_2': $X_7^v \rightarrow X_7^c$. (b) Imaginary dielectric constant. Solid line: sX-LDA plus SOC. Dashed line: Experiment[59]

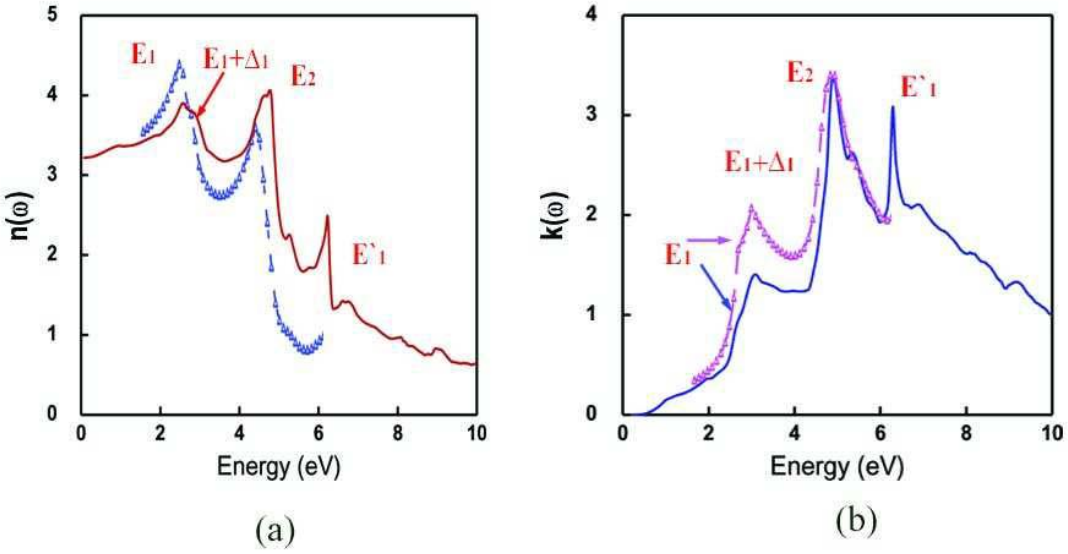

Figure 3.2: Index of refraction for InAs as a function of energy. (a) Real index of refraction, $n(\omega)$ and (b) extinction coefficient, $k(\omega)$. Solid line: this work. Small triangles: Plot from experimental data by Aspnes *et al*.[59]

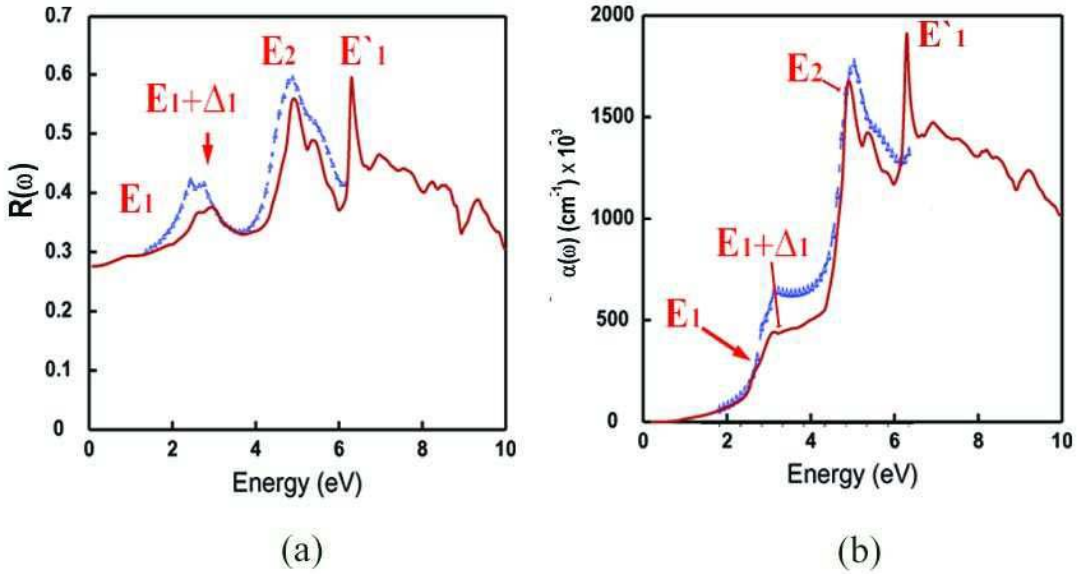

Figure 3.3: (a) Reflectivity, $R(\omega)$ and (b) absorption coefficient $\alpha(\omega)$ of InAs as a function of energy. Solid line: this work. Small triangles: Plot from experimental data by Aspnes *et al*.[59]

and Δ_2.

We find a similar peak structure to experiment, namely the clear structure of the E_1, $E_1+\Delta_1$ and E_2 peaks as in experiment. The shift in energy of the E_1 peak is thought to arise from exciton effects not considered in our work.They are 0.2 eV off from the experimental peak positions. The $E_1^{'}$ peak position matches experiment.

Figure 3.5 shows (a) the index of refraction[$n(\omega)$] and (b) the extinction coefficient[$k(\omega)$]. The E_1, $E_1 + \Delta_1$ and E_2 peak positions in $n(\omega)$ off by 0.3 eV as they are in $\varepsilon_2(\omega)$, while the peak positions of our extinction coefficient, $k(\omega)$, match very well with experiment.

The reflectivity and absorption coefficient are presented in Fig. 3.6. As in the InAs case, the peak positions of our result show good agreement with experiment.

In Table 3.3, we list the CP energies predicited by LDA, and the sX-LDA plus SOC and those from experiment. The E_0' energy ($\Gamma_8^v \rightarrow \Gamma_7^c$ transition) by the sX-LDA plus SOC is off by 0.3 eV from experiment but sX-LDA plus SOC in general gives good agreement of the CP energies with experiment.

3.3.3 GaSb

Figure 3.7 shows our calculated (a) band structure and (b) imaginary dielectric function. The GaSb band structure shows a similar dispersion as the previous InAs and InSb results, except their curvature and enegy scales are different. We show interband transitions E_0, E_0', E_1, and E_2 at Γ, L and X. Our $\varepsilon_2(\omega)$ shows excellent agreement with experiment[57] in their peak positions such as at the E_1,$E_1 + \Delta_1$ and E_2 peaks. In this case, the experimental values reported have been obtained with exciton contributions excluded.

The index of refraction and extinction coefficient are presented in Fig. 3.8 We pro-

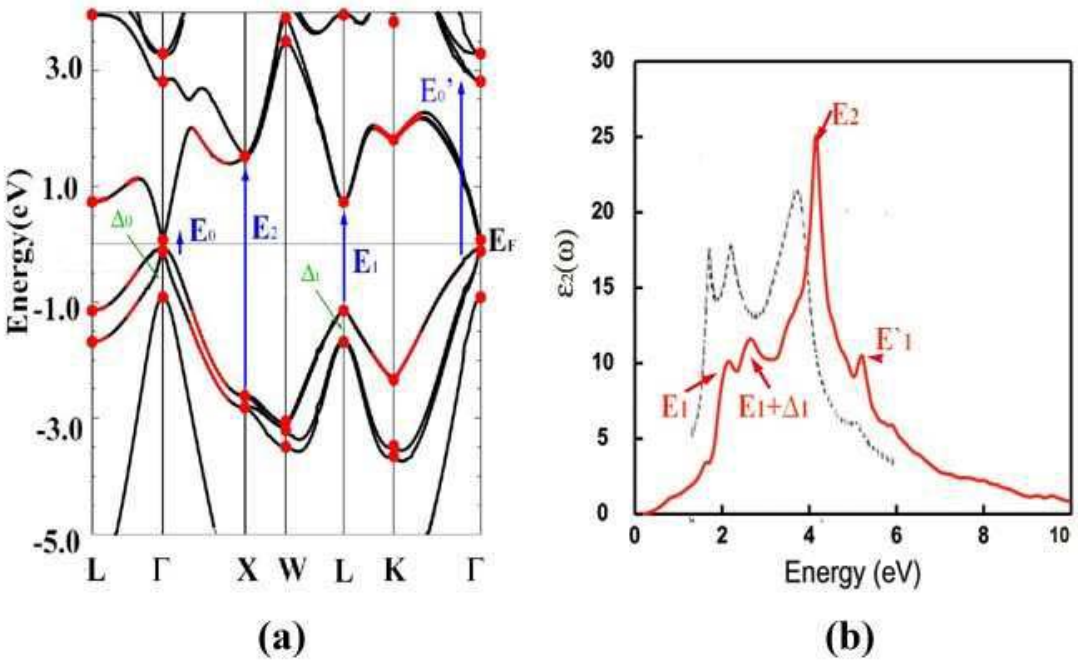

Figure 3.4: (a) Band structure of InSb. High symmetry points are shown in circles and important interband transitions are labeled as E_0 :$\Gamma_8^v \rightarrow \Gamma_6^c$, E_0' :$\Gamma_7^v \rightarrow \Gamma_7^c$, E_1:$L_{4,5}^v \rightarrow L_6^c$,$E_1+\Delta_1$:$L_6^v \rightarrow L_6^c$,$E_2$:$X_7^v \rightarrow X_6^c$, and E_2': $X_7^v \rightarrow X_7^c$. (b) Imaginary dielectric constant. Solid line: sX-LDA plus SOC. Dashed line: Experiment[59]

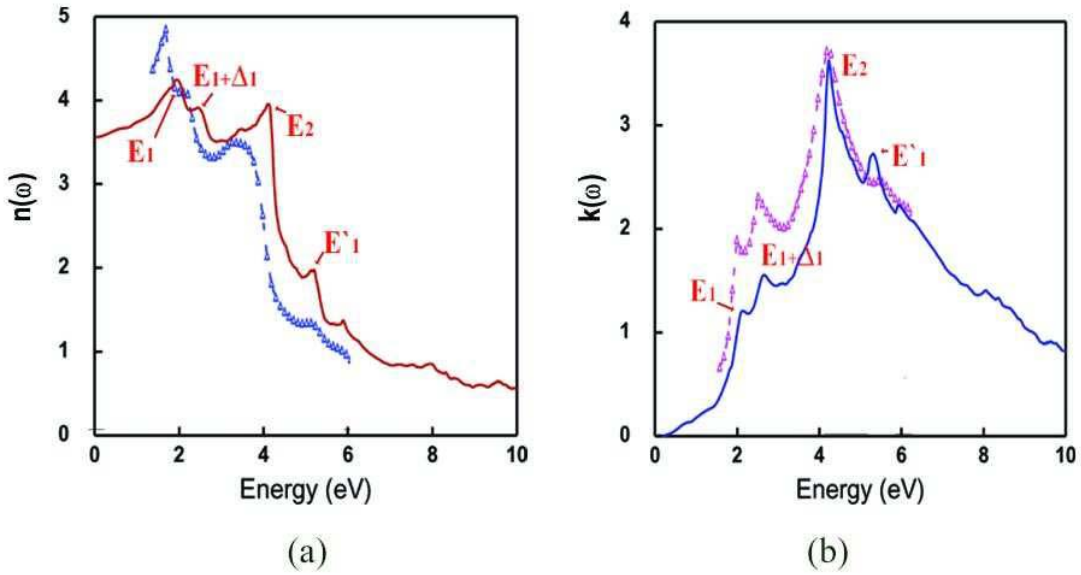

Figure 3.5: Index of refraction for InSb as a function of energy. (a) Real index of refraction, $n(\omega)$ and (b) extinction coefficient, $k(\omega)$. Solid line: this work. Small triangles: Plot from experimental data by Aspnes *et al*.[59]

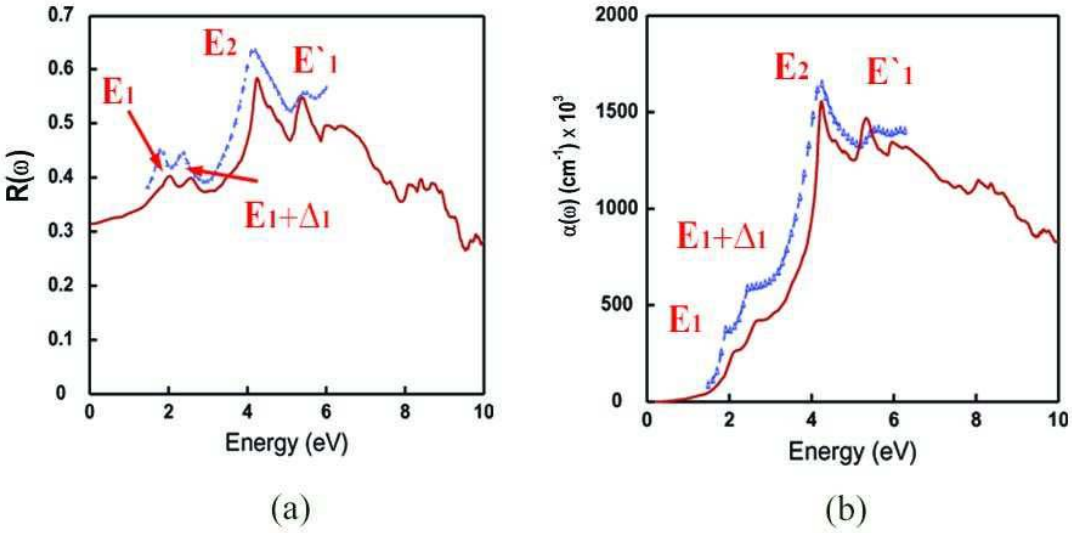

Figure 3.6: (a) Reflectivity, $R(\omega)$ and (b) absorption coefficient $\alpha(\omega)$ of InSb as a function of energy. Solid line: this work. Small triangles: Plot from experimental data by Aspnes *et al*.[59]

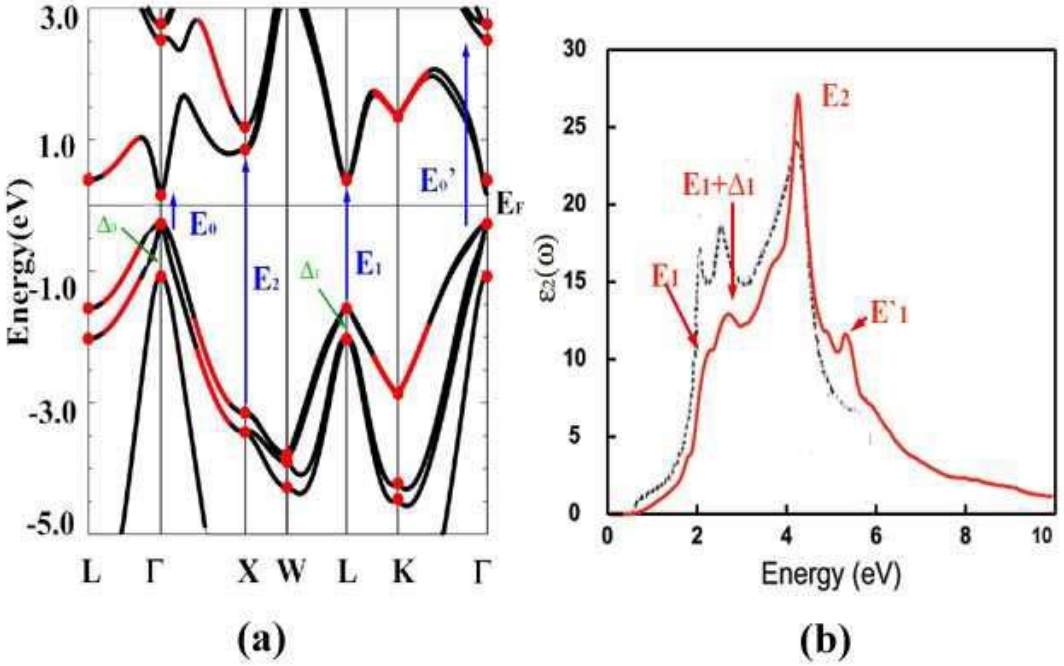

Figure 3.7: (a) Band structure of GaSb. High symmetry points are shown in circles and important interband transitions are labeled as E_0 :$\Gamma_8^v \rightarrow \Gamma_6^c$, E_0' :$\Gamma_7^v \rightarrow \Gamma_7^c$, E_1:$L_{4,5}^v \rightarrow L_6^c$,$E_1 + \Delta_1$:$L_6^v \rightarrow L_6^c$,$E_2$:$X_7^v \rightarrow X_6^c$, and E_2': $X_7^v \rightarrow X_7^c$. (b) Imaginary dielectric constant.Solid line: sX-LDA plus SOC. Dashed line: Experiment from Ref.[57]

duced a structure similar to that in the dielectric function. As E_1' is off by 0.36 eV from experiment in $\varepsilon_2(\omega)$, it is also in both the real and imaginary index of refraction.

Figure 3.9 presents (a) the reflectivity and (b) the absorption coefficient. In both cases, we reproduced a peak structure similar to experiment. As in the case of the dielectric function, we see good agreement in the peak positions.

In Table 3.4, CP energies are listed as obtained by LDA, sX-LDA plus SOC and experiment. The CP energies at Γ calculated by sX-LDA plus SOC are systematically underestimated by 0.3-0.4 eV compared to experiment. However, for the other transitions at L and X, the sX-LDA plus SOC gives good agreement with experiment.

3.3.4 AlSb

AlSb is the only indirect gap material in our study. The band structure and imaginary dielectric constant are shown in Fig. 3.10. We see an indirect band gap from the VBM at Γ to the CBM at a point along the $\Gamma - X$ direction.

Again in the band structure, we denoted the interband transitions by E_0, E_1 and E_2 and the spin-orbit split energies by Δ_0 and Δ_1. The calculated $\varepsilon_2(\omega)$ shows an almost negligible effect of the indirect band gap. The peak positions of sX-LDA plus SOC show good agreement with experiment at $E_0 + \Delta_0$, $E_1 + \Delta_1$, E_2 and E_1'(cf. Table 3.5).

The index of refraction [$n(\omega)$] and the extinction coefficient [$k(\omega)$] are shown in Fig. 3.11. In $n(\omega)$, the E_1 and $E_1 + \Delta_1$ peak positions agree well with experiment although their heights are different. For the E_2 peak, where experiment shows a rather suppressed peak, there is however good agreement with experiment for its calculated position. However, the peak positions in $k(\omega)$ show generally good agreement with experiment, especially

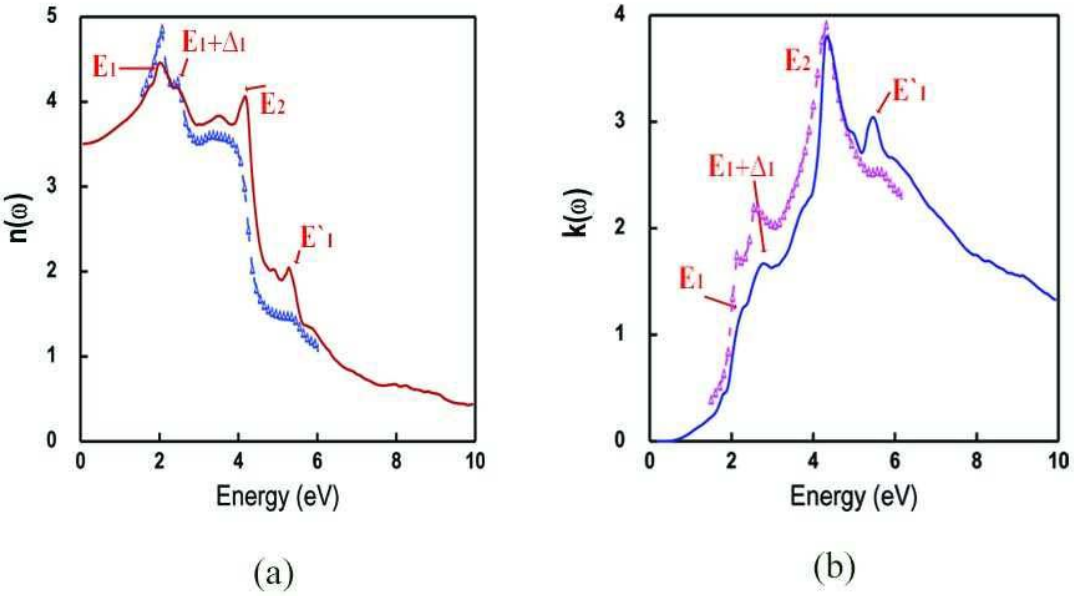

Figure 3.8: Index of refraction for GaSb as a function of energy. (a) Real index of refraction, $n(\omega)$ and (b) extinction coefficient, $k(\omega)$. Solid line: this work. Small triangles: Plot from experimental data by Aspnes *et al*.[59]

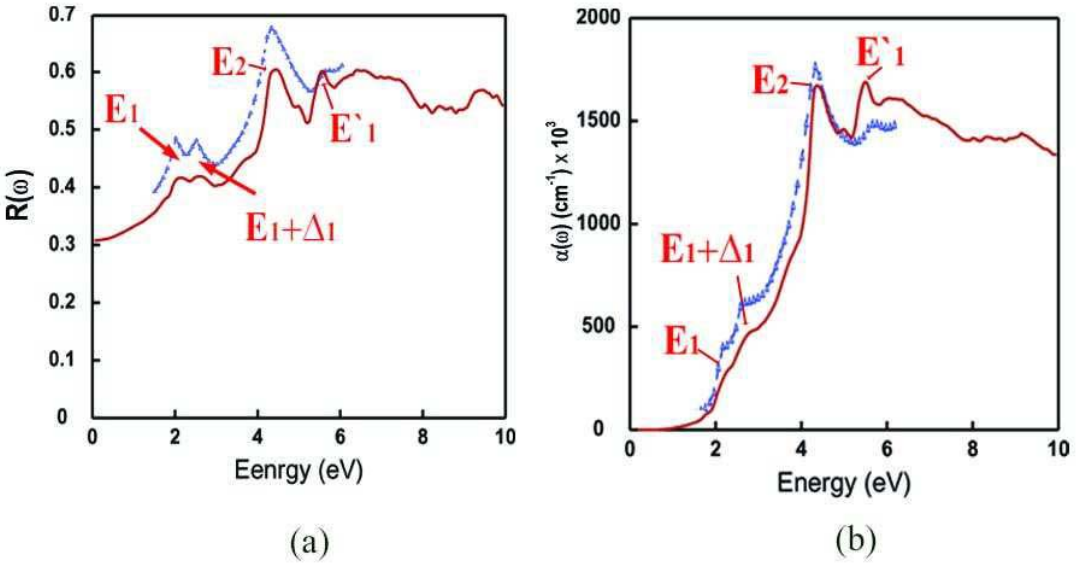

Figure 3.9: (a) Reflectivity, $R(\omega)$ and (b) absorption coefficient $\alpha(\omega)$ of GaSb as a function of energy. Solid line: this work. Small triangles: Plot from experimental data by Aspnes *et al*.[59]

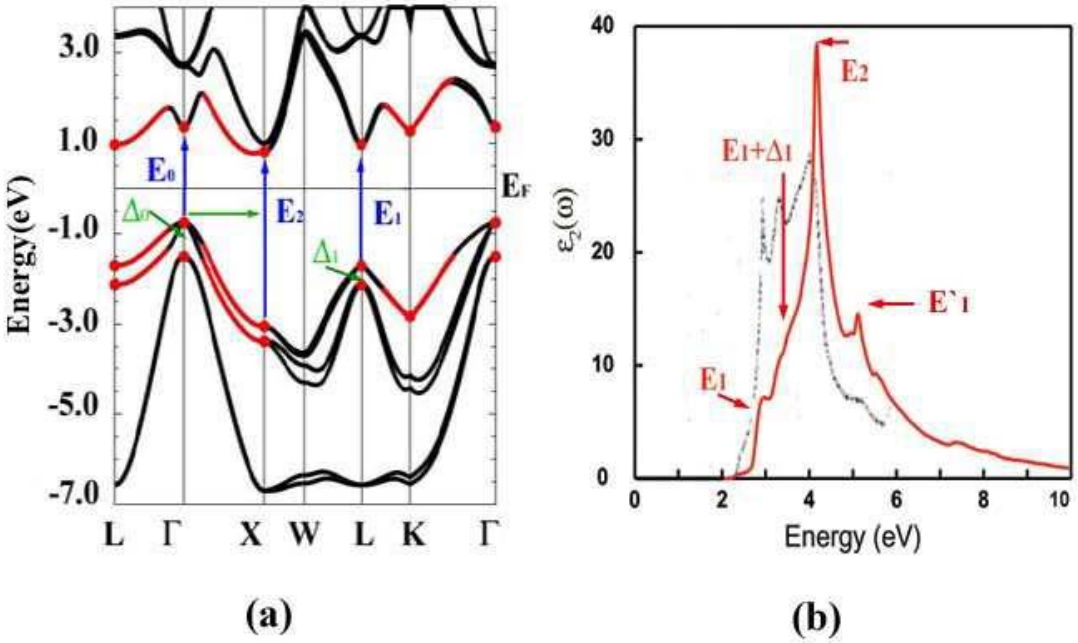

Figure 3.10: (a) Band structure of AlSb. High symmetry points are shown in circles and important interband transitions are labeled as E_0 :$\Gamma_8^v \rightarrow \Gamma_6^c$, E_0' :$\Gamma_7^v \rightarrow \Gamma_7^c$, E_1:$L_{4,5}^v \rightarrow L_6^c$,$E_1+\Delta_1$:$L_6^v \rightarrow L_6^c$,$E_2$:$X_7^v \rightarrow X_6^c$, and E_2': $X_7^v \rightarrow X_7^c$. (b) Imaginary dielectric constant. Solid line: sX-LDA plus SOC. Dashed line: Experiment[58]

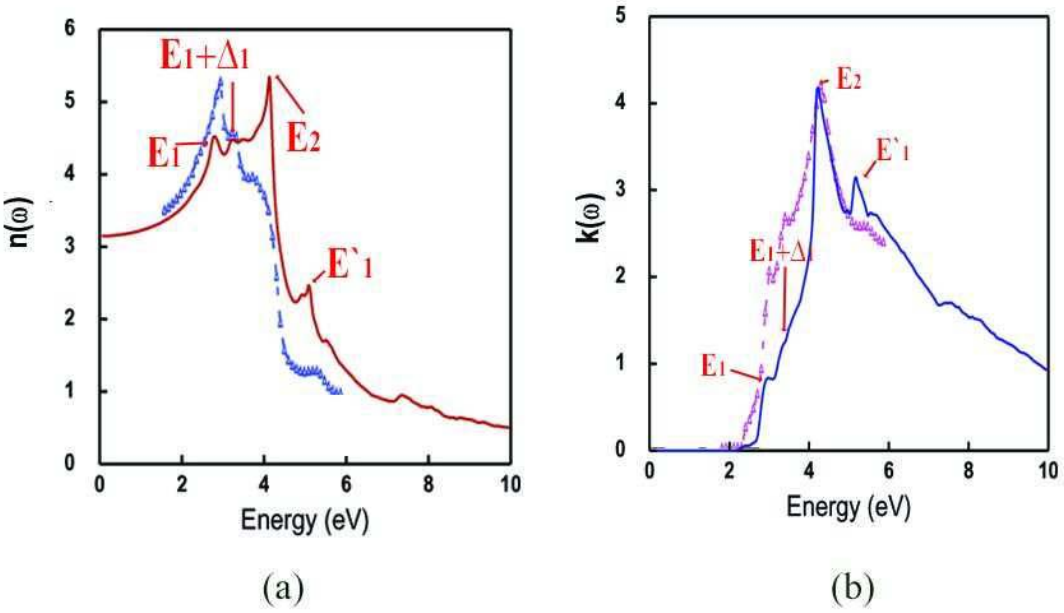

Figure 3.11: Index of refraction for AlSb as a function of energy. (a) Real index of refraction, $n(\omega)$ and (b) extinction coefficient, $k(\omega)$. Solid line: this work. Small triangles: Plot from experimental data by Aspnes *et al*.[59]

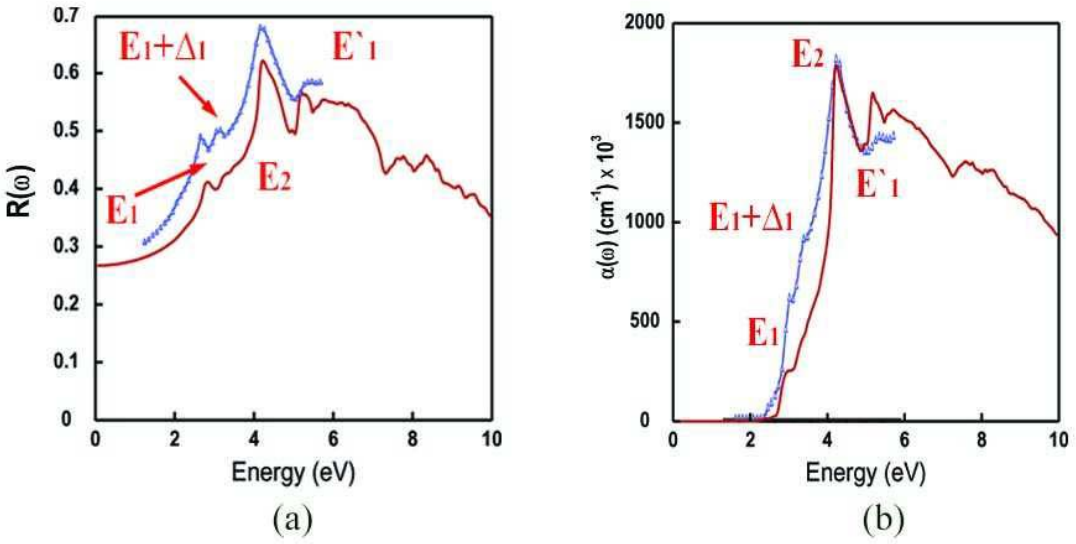

Figure 3.12: (a) Reflectivity, $R(\omega)$ and (b) absorption coefficient $\alpha(\omega)$ of AlSb as a function of energy. Solid line: this work. Small triangles: Plot from experimental data by Aspnes *et al*.[59]

for the main E_2 peak. Figure 3.12 presents (a) the reflectivity and (b) the absorption coefficient; excellent agreement with experiment is seen in their peak positions. Moreover, in the absorption coefficient, the E_2 peak shows a good match with experiment in both position and height.

We list CP energies in Table 3.5 determined by LDA, sX-LDA plus SOC and experiment. The sX-LDA plus SOC gives systematically lower values by 0.1$\sim$ 0.3 eV than experiment, however, we have a striking improvement over the LDA results given by sX-LDA plus SOC.

3.4 Summary

We have presented results of fully first-principles calculations of the electronic structures and optical properties of InAs, InSb, GaSb and AlSb as obtained with the sX-LDA plus spin-orbit coupling approach as implemented in the FLAPW method. The dielectric functions are evaluated with the longitudinal expression with full $e^{i\mathbf{q}\cdot\mathbf{r}}$ matrix elements. In general, comparisons with experiment show good agreement of our calculated dielectric functions in their peak positions. The sX-LDA plus SOC is found to give remarkable improvement over LDA in the critical-point energies and dielectric functions. The method employed to calculate the optical properties has the following features: (i) it is based *purely* on first-principles in that we do not use any artificial parameters to adjust the experimental results; it uses only the self-consistent eigenvalues and wavefunctions; (ii) the nonlocality of the Hamiltonian requires the longitudinal expression for the matrix elements. By comparison, using a scissor-operator to shift the conduction bands rigidly does not guarantee

preserving the band character at all k points; shifting the bands to match eigenvalues at one particular point does not neccessarily match the eigenvalue shift at all k points.

Chapter 4: Superconductivity

4.1 Historical Overview

After the discovery of superconductivity in mercury metals by K. Onnes in 1911,[62] superconductivity became an immense subject in physics. There has been enormous progress in understanding superconductivity theoretically and experimentally as well as in synthesizing superconducting materials. Research on superconductivity has two aspects: (i) the theoretical understanding and the experimental verification of the properties exhibited by this phenomenon, and (ii) the discovery and/or synthesis of specific superconducting materials. In Fig. 4.1, the interesting superconducting materials discovered are chronologically listed along with their T_C's. In early times, superconductivity was discovered mostly in metallic elements before the Nb compounds were discovered, which possessed the record high T_C until 1986, when cuprates were discovered. The Nb-related compounds can be further divided into two classes: those with A15 and those with B1 structures. A15 compounds, such as $\mathrm{Nb_3Al}$, $\mathrm{Nb_3(Al_{0.8}Ge_{0.2})}$, $\mathrm{Nb_3Sn}$, $\mathrm{Nb_3Ga}$, were reported T_C between 16.8$\sim$ 20 K. Vanadium compounds such as $\mathrm{V_3Si}$ and $\mathrm{V_3Ga}$ with A15 structure were also reported to have similar T_C to those of the Nb compounds. The B1 structure, which has NaCl-type face-centered cubic structure, such as NbC and NbN, have T_C's around 16 K. Cuprates have

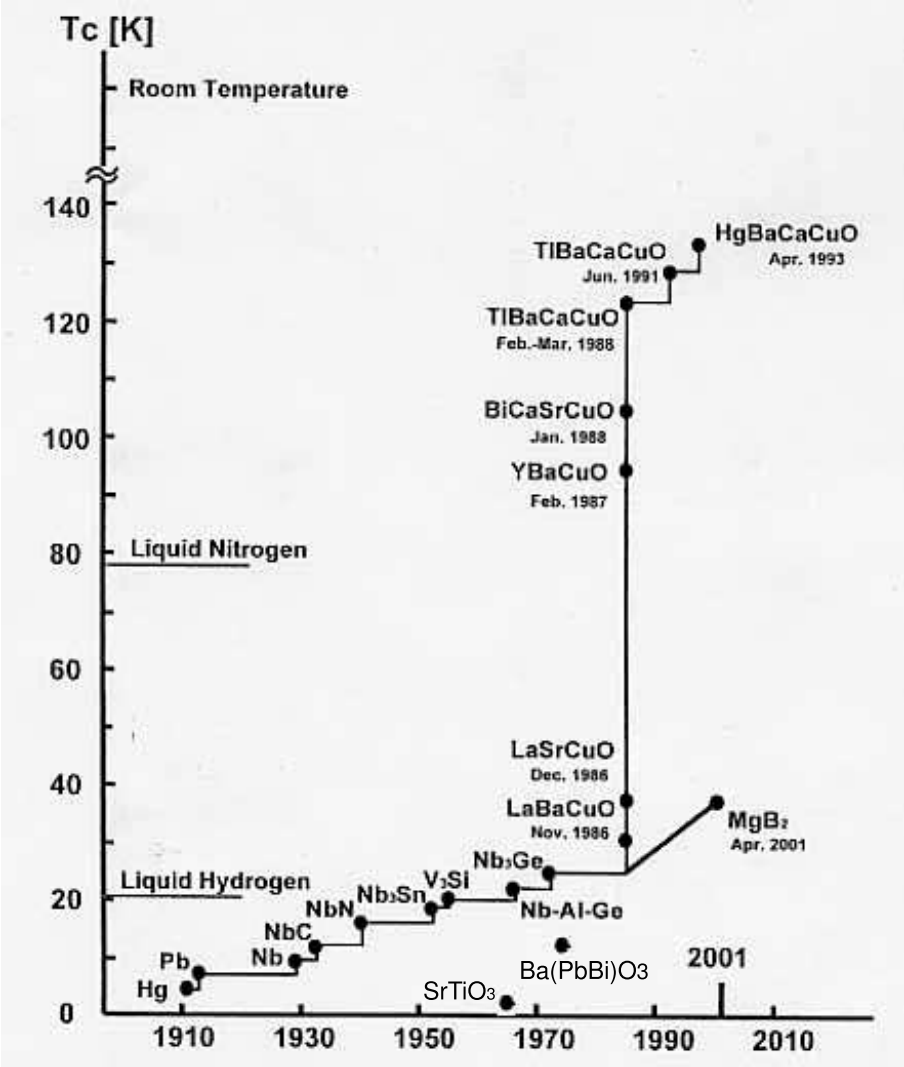

Figure 4.1: Historical development of critical temperatures in the superconducting materials. From Kamimura *et al*.[63]

drastically higher T_C's, and exist in various compounds, where the copper-oxide plane is the common attribute. There are other classes of superconducting materials, where T_C are not as high as the cuprates. In the 1960's, doped $\mathrm{SrTiO_3}$ was predicted and confirmed to be superconducting,[64,65] which was the first oxide material exhibiting superconductivity, although its T_C was very low ($< 1K$). The other oxide superconductors are $\mathrm{Ba(Pb,Bi)O_3}$ and $\mathrm{LiTiO_4}$. Finally, there is the most recently discovered $\mathrm{MgB_2}$, which is in a class by itself. Its constituents are light atoms which is quite against the conventional wisdom that compounds with heavier atoms would have higher T_C. Its T_C exceeds the limit of conventional phonon mediated superconductivity, with a multi-gap feature. In this thesis, we will not discuss $\mathrm{MgB_2}$.

In 1933 the Meissner effect[66] was discovered, showing that superconductivity is a thermodynamic phase.[67] In 1950, the isotope effect was discovered and a successful theory formulated: Two independent experiments succeeded in measuring the isotope effect in Hg.[7,8] This experiment had been done by Kammerling Onnes and Tuyn, but because the poor experimental accuracy of the time, it failed. Fröhlich studied the electron-phonon interaction in metals using a field-theoretical approach, where he demonstrated in second-order perturbation theory that electrons exhibit an effective attractive interaction via phonons, The theory, though incomplete, became the foundation for subsequent works. Bardeen also looked into the electron-phonon interaction.[68] However, Fröhlich and Bardeen, both failed to properly explain superconductivity, because they focused on the single-electron self-energies instead of taking into account the two-electron instability. Nonetheless, it was shown by Fröhlich that the energy lowering is proportional to $\exp(-1/\lambda)$ and that λ cannot be obtained by a perturbation expansion, where λ is the di-

mensionless electron-phonon coupling constant. Later, Pines along with Bardeen derived an *effective* electron-phonon interaction. They considered both electron-electron interactions *and* the lattice degrees of freedom.[69] The effective electron-phonon interaction of Pines and Bardeen was subsequently further simplified and used in the BCS[19] calculation. In 1957, the BCS theory[19] came out. BCS is undoubtedly one of the most successful theories in condensed matter physics. It applies universally, in a sense that it does not take into account for any particular mechanism of Cooper pairing, and it applies to almost all materials. Yet, the BCS theory has explained many phenomena in a rather simple way. After its appearance, alternative formalisms were invented, for example: (i) Anderson derived an RPA treatment of a reduced Hamiltonian;[70] (ii) a general method of Boguliubov[71] was later adapted to inhomogeneous superconductors by de Gennes;[72] (iii) Gor'kov developed a Green's function's method.[73] Landau-Ginzburg's phenomenological approach[74] was also developed, which can be derived from the Gor'kov formalism. In this thesis, only a brief review on BCS and Eliashberg theory will be given in the following sections.

4.2 BCS and Eliashberg theory

The BCS theory, by simplifying interactions, succeeded in establishing the pairing formalism. The elegance of the BCS theory is its universality: it does not distinguish one superconductor from another, and moreover, one mechanism from another. In the simplification of the interaction, pairing is assumed to be attractive for certain range of energies. This BCS interaction is schematically illustrated in Fig. 4.2 (a), where the energy cutoff of interaction is practically regarded as the Debye frequency, ω_D. Generally, the pairing

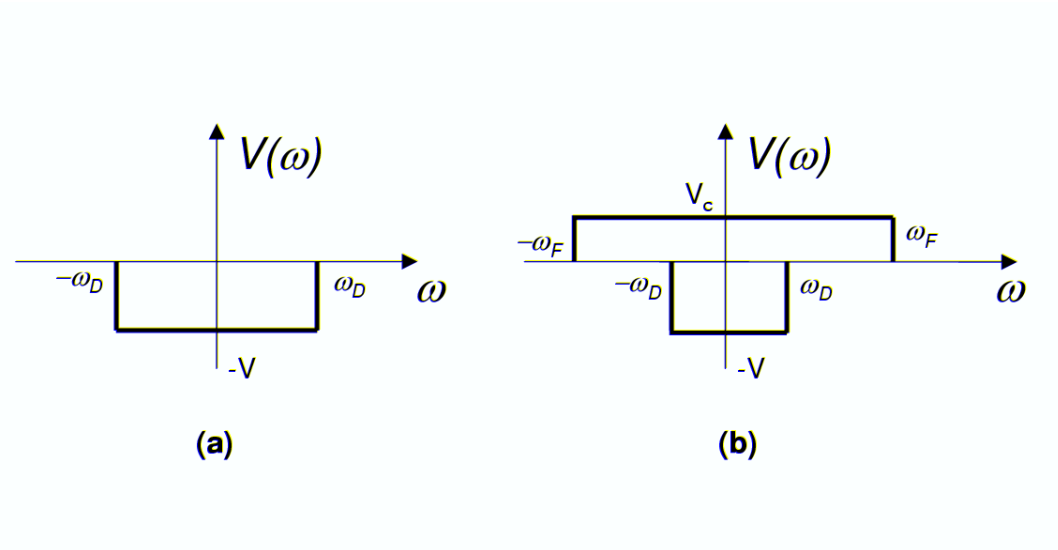

Figure 4.2: Schematic diagram of effective potential in (a) BCS theory and (b) in the more general case such as Eliashberg theory. It is approximated as a potential well for certain range of energies (frequencies).

interaction in the BCS theory is assumed to be phonon mediated, not because it is the sole one, but because it is the only mechanism so far confirmed by experiment.

In BCS theory, the gap equation is

$$\Delta_{\mathbf{k}} = -\sum_{\mathbf{k}'} V_{\mathbf{k}\mathbf{k}'} \frac{\Delta_{\mathbf{k}'}}{2E_{\mathbf{k}}} \tanh(\frac{\beta E_{\mathbf{k}'}}{2}), \tag{4.1}$$

where $E_{\mathbf{k}} = (\epsilon^2 + \Delta_{\mathbf{k}}^2)^{1/2}$ and the electron number is given by

$$n = 1 - \sum_{\mathbf{k}} \frac{\epsilon_{\mathbf{k}} - \mu}{E_{\mathbf{k}}} \tanh(\frac{\beta E_{\mathbf{k}'}}{2}). \tag{4.2}$$

Converting the above expression to an integral form with cutoff frequency, ω_D, it becomes

$$\frac{1}{\lambda} = \frac{1}{N(0)V} = \int_0^{\omega_D} \frac{d\epsilon}{\epsilon} \tanh(\frac{\beta}{2}\epsilon), \tag{4.3}$$

where $N(0)$ is density of states at E_F and V is the effective pairing interaction as illustrated in Fig. 4.2 (a). The strength of interaction is expressed by the dimensionless parameter $\lambda = N(0)V$, and the gap, Δ at T=0 is given by

$$\Delta(0) = \frac{2\omega_D \exp(-1/\lambda)}{1 - \exp(-1/\lambda)} = \begin{cases} 2\omega_D \cdot \exp(-1/\lambda), & \text{weak coupling} \\ 2\omega_D \lambda, & \text{strong coupling.} \end{cases} \tag{4.4}$$

We can evaluate T_C taking $\Delta = 0$ in Eq. (4.3), which can be done numerically. In the weak coupling limit ($\lambda \ll 1$), we get the BCS equation for T_C.

$$k_B T_C = 1.14\, \omega_D \exp(-1/\lambda), \quad \text{weak coupling} \tag{4.5}$$

In Eliashberg theory, extending from BCS theory, phonon mediation is again assumed as the pairing mechanism. Moreover, it includes the retardation effect due to "sluggishness" of the phonon responses. Furthermore, the effective interaction is no longer assumed to be

attractive as in BCS. In reality, the interaction between electrons is divided by two parts, attractive interactions and repulsive Coulomb interactions, as illustrated in Fig. 4.2(b), where ω_D is the Debye frequency as in BCS model, and ω_F is the Fermi frequency of the whole system. Instead of working with two frequencies, Coulomb repulsion (μ) is renormalized to $\mu^\star$ so that we deal with one frequency,[75]

$$\mu^\star = \frac{\mu}{\mu + \log(E_F/\omega_D)}. \tag{4.6}$$

We will not give a detailed derivation of Eliashberg theory, since the more sophisticated and pedagogical reviews can be found in articles by Marsiglio and Carbotte,[76] Allen and Mitrovic,[77] and Abrikosov *et al.*[78] Eliashberg theory does not distinguish weak and strong coupling limits, while the weak coupling limit solution reduces to the BCS equation; it has been proved adequate for the strong-coupling case where the BCS interpretation shows some discrepancies with experiment. There have been attempts to solve Eliashberg theory for strong-coupling materials; however, solving the Eliashberg equations self-consistently is not trivial. There are many approaches but the formulation by Choi *et al.*[79] will be used here. In Eliashberg theory, the starting point is the Nambu formalism[80] with the electron Green's function and the anomalous amplitude in the finite-temperature Matsubara representation. The self-energy, $\Sigma(\mathbf{k}, i\omega_m)$, which contains the information of the electron-phonon interaction, can be separated into its even and odd components in momentum space. Eliashberg equations at frequency $i\omega_n = i(2n+1)\pi T$, where n is an integer, are expressed as

$$Z(\mathbf{k}, i\omega_n) = 1 + \frac{1}{(2n+1)} \sum_{\mathbf{k}',n'} W_{\mathbf{k}'} \lambda(\mathbf{k}, \mathbf{k}', n-n') \frac{\omega_{n'}}{\sqrt{\omega_{n'}^2 + \Delta(\mathbf{k}', i\omega_{n'})}}, \tag{4.7}$$

$$Z(\mathbf{k}, i\omega_n)\Delta(\mathbf{k}, i\omega_n) = \pi T \sum_{\mathbf{k}',n'} W_{\mathbf{k}'} [\lambda(\mathbf{k}, \mathbf{k}', n-n') - \mu^\star(\omega_c)] \frac{\omega_{n'}}{\sqrt{\omega_{n'}^2 + \Delta(\mathbf{k}', i\omega_{n'})}}, \tag{4.8}$$

where ω_c is the cutoff frequency to restrict integer n' summation only for $|\omega_{n'}| \leq \omega_c$, and $W_{\mathbf{k}}$ is the fraction of the density of states (DOS) of $\mathbf{k}$ points on the Fermi surface. The $Z(\mathbf{k}, i\omega_n)$ function in Eq. (4.7) is known to reflect the renormalization of the electron-phonon interaction, while the gap function $\Delta(\mathbf{k}, i\omega_n)$ is simply the superconducting gap. T_C is determined by the temperature at which $\Delta(\mathbf{k}, i\omega_n)$ vanishes. The imaginary frequency can be analytically converted to the real axis, so that we get the gap function $\Delta(\mathbf{k}, \omega)$.[81] Further details of the Eliashberg formalism are not given in this thesis, and can be found in articles by Allen and Mitrovic,[77] and Carbotte and Marsiglio.[76]

4.3 McMillan-Allen-Dynes formula and RMTA

In this section, we discuss the widely used McMillan T_C formula and the rigid muffin-tin approximation (RMTA), which is a crude but easier way to estimate T_C than by solving Eliashberg equations. McMillan derived this T_C formula for strong-coupling regime[20] by solving Eliashberg equation numerically for well-known *d* electron superconducting materials. Later, Allen-Dynes[82] analyzed McMillan's formula to give the correct result for $\lambda \geq 2$ with a modified prefactor and the correct asymptotic behavior $T_C \sim (\lambda\langle\omega^2\rangle)^{1/2}$ for large λ. McMillan, in his derivation, took the point of view that the theory of superconductivity is accurate, and T_C, with an accuracy of $\sim$1% can be calculated given the following properties of the normal state: (a) the bands near the Fermi energy, (b) the phonon dispersion (c) the screened electron-phonon interaction matrix elements, and (d) the screened Coulomb interaction between electrons. These four normal state properties were not all known for any given metal; however, by utilizing the known properties of metals he determined em-

pirical values for the electron-phonon coupling constants λ. First, using an approximation to the analytic equations, he then obtained a numerical solution. The analytic expression and its approximation are based on the Eliashberg formalism as in Eq. (4.7) and Eq. (4.8). Finally, he showed that an expression for T_C can be obtained as a simple analytic function of the coupling constants λ and $\mu^\star$:

$$T_C = \frac{\Theta_D}{1.45} \exp\Big[- \frac{1.04(1+\lambda)}{\lambda - \mu^\star(1+0.62\lambda)}\Big], \tag{4.9}$$

Taking into account the asymptotic behavior for large λ, the prefactor can be calculated as $\langle\omega\rangle/1.20$, where

$$\langle\omega\rangle = \frac{2}{\lambda}\int d\omega\ \alpha^2F(\omega), \tag{4.10}$$

and $\alpha^2F(\omega)$ is the electron-phonon spectral function.

Although this T_C formula, as given by McMillan and Allen-Dynes, is used in calculations, it is necessary to evaluate λ and $\mu^\star$. To this end, Gaspary and Gyorffy (GG)[21] proposed the rigid muffin-tin approximation (RMTA). The main idea is that the electron-electron interactions result from the exchange of phonons. The muffin-tin sphere is considered to be a rigid scattering center and this scattering results in only a potential change. In this picture, both incoming and outgoing electronic waves are taken into account using the partial wave technique from scattering theory. From McMillans' strong coupling theory,[20] GG obtained the electron-phonon coupling constant using this rigid muffin-tin (ion) approximation (RMTA) as

$$\lambda = \frac{n(E_F)\langle I^2\rangle}{M\langle\omega^2\rangle}, \tag{4.11}$$

where M is the atomic mass, $\langle\omega^2\rangle$ is the square average of the renormalized phonon frequency, and $\langle I^2\rangle$ is the square of the electron-phonon interaction matrix element averaged

at the Fermi energy. We note that in Eq. (4.11), the electronic and phonon degrees of freedom are separated into numerator and denominator, respectively. GG obtained the wave function by expanding the Bloch function in the angular momentum representation,

$$\psi_{\mathbf{k}}(\mathbf{r}) = \sum_{\ell,m} a_{\ell,m}(\mathbf{k}) R_\ell(r, E_{\mathbf{k}}) Y_{\ell,m}(\hat{r}), \tag{4.12}$$

where for the muffin-tin radius a, the radial part $R_\ell(r, E_{\mathbf{k}})$ is the usual scattering solution of the radial Schrödinger equations for $r > a$, $R_\ell = j_\ell \cos\delta_\ell - n_\ell \sin\delta_\ell$ with δ_ℓ the phase shifts. Instead of GG's original form, in this thesis, we use the form by Skriver and Mertig[83,84] to evaluate the spherically averaged Hopfield parameter[85]

$$\eta = 2N(E_F) \sum_\ell (\ell+1) M^2_{\ell,\ell+1} \frac{f_\ell f_{\ell+1}}{(2\ell+1)(2\ell+3)}, \tag{4.13}$$

where $f_\ell = N_\ell(E_F)/N(E_F)$ is a fractional partial density of states (pDOS) of a given atom and $M_{\ell,\ell+1}$ is an electron-phonon matrix element given by

$$M_{\ell,\ell+1} = \int_0^R r^2 dr \; R_\ell \frac{dV}{dr} R_{\ell+1}. \tag{4.14}$$

Although the RMTA scheme is approximate compared to the Eliashberg equations, it has been relatively successful at predicting superconductivity and the order of T_C.

4.4 Excitonic mechanism

As mentioned in Sec. 4.2, the electron-electron interaction is assumed to be attractive in BCS theory to be in the form of a rectangular well [Fig. 4.2(a)]. In general, the BCS T_C formula has the form

$$T_C = \theta e^{-1/\lambda}, \tag{4.15}$$

where the dimensionless parameter λ characterizes the electron-phonon interaction strength in phonon mediation scheme [$\lambda = N(0)V$] and the depth of the rectangular potential well. The prefactor θ, on the other hand, characterizes the "width" of the potential well. Eq. (4.15) is obtained in the "weak-coupling", i.e. $\lambda \ll 1$, where detailed pairing mechanism behind this is not specified. In the phonon mediation scheme, the prefactor θ is generally taken from the Debye temperature, Θ_D. Ginzburg,[86,87] estimated that with the Debye temperature, $\Theta_D = 100 \sim 500K$, $\lambda \leq 1/3$, so even for $\Theta_D = 500K$, the critical temperature $T_C \leq 500e^{-3} \leq 25K$. The higher the Debye temperature, the weaker the electron-phonon interaction, hence the lower λ. Therefore the argument given by Ginzburg is generally valid. To a considerable extent, we can say that

$$T_C \leq 30 \sim 40K \quad (\text{phonon mechanism of superconductivity}). \tag{4.16}$$

Noting the sensitivity of the exponential function to λ, raising the value of T_C would be impossible for the usual value of Θ_D even for $\lambda \approx 1 \sim 2$. An "excitonic mechanism" *or* "electronic mechanism" was proposed by Little[9] and Ginzburg[10] in 1960's, which was believed to overcome the restriction on T_C of Eq. (4.16). In the excitonic mechanism, the attraction of electrons is due to excitons or . other waves not the lattice degrees of freedom (phonons). There can be longitudinal excitons, for example plasmons. If the damping of such excitons is weak, they can replace phonons as the pairing mechanism. For excitons, the prefactor θ_{ex}, is of order $10^3 \sim 10^5$ K so a larger T_C can be obtained even with a relatively small value of λ.

Later ABB (Allender, Bray, Bardeen) studied a metal-semiconductor interface model

[0a] MgB2, an electron-phonon superconductor, which has $T_C \approx 40K$, is an exception but it is a superconductor with multi-gap features.

in detail, claiming the excitonic mechanism can enhance T_C much more than the phonon mechanism.[11] The basic idea is that the metallic electrons penetrate into the semiconductor gap region creating virtual excitons which scatter other metallic electrons. For this process to be effective, metallic electrons have to live long enough in the semiconductor gap region. To estimate the interaction strength, λ_{ex}, of this exciton mechanism, ABB followed the technique of Cohen and Anderson[88] used in the phonon mediation scheme, and obtained an electron-exciton interaction strength

$$\begin{aligned} \lambda_{ex} &= N(0)\langle V_{ex}\rangle \\ &\approx [\, N(0)\langle s(4\pi e^2/q^2)\rangle]\langle s\rangle\gamma b(\omega_p^2/\omega_g^2) \\ &= s\gamma b\mu(\omega_p^2/\omega_g^2), \end{aligned} \tag{4.17}$$

where ω_p and ω_g are the plasma frequency and average band gap of semiconductor, respectively, b is the fraction of time the electron spends in the semiconductors, μ is the density of states times an average of the screened Coulomb interaction, and γ is the fraction of the tail of the metallic density of states at the interface. The angular bracket in Eq. (4.17) denotes a *k* space summation and s is the average of the screening, $\langle 1/\epsilon(\mathbf{q},\omega)\rangle$. Making favorable estimates for the parameters ($b \sim \frac{1}{4},\ \gamma \sim \frac{1}{2},\ s\mu \sim \frac{1}{3},\ s \sim \frac{1}{2},\ \omega_p \sim 10eV, \omega_g \sim 2eV$), ABB obtained $\lambda_{ex} \leq 0.5$.

Inkson and Anderson (I-A).[89] objected to the ABB theory by considering the $\mathbf{q}$ dependence of the dielectric functions for both the metallic and semiconducting regions. I-A argued that the effective interaction is screened by $1/\varepsilon_s(\mathbf{q},\omega)$. This would give the interaction screened by the metal plus the interaction screened by $1/\varepsilon_0$, where the second term would give a repulsive contribution. I-A concluded that the metallic region is much more favorable than the semiconductor for superconductivity. However, in reply to I-A,[90]

ABB questioned the detailed structure of the I-A semiconductor dielectric function and its appropriateness, which was highly approximate. Later, Cohen and Louie considered the ABB problem in IA's perspective.[91] They considered a metal-semiconductor interface, and evaluated the kernel function with three different kinds of dielectric functions: (1) I-A's dielectric functions for each metallic and semiconductor region, (2) the Lindhard dielectric function for the metal kernel, and (3) $\epsilon(\mathbf{q}, \omega)$ of Ge for the semiconductor. A repulsive interaction was obtained in Cohen and Louie's work; however, it was rather a simplified geometry and local-field effects were completely ignored. Nevertheless, it was shown that the attractive interaction could exist, though not sufficient to give a net attractive interaction from the kernel estimation for the entire frequency range. Later, Zakharov *et. al*[92] extended Louie and Cohen's work to a Si-jellium multilayer with *ab initio* dielectric functions including local-field effects. An attractive interaction was found for a certain frequency range, but it was concluded from their kernel calculation that there was no superconductivity. The geometry Zakharov studied, however, with jellium sandwiched by semiconductors, is not realizable in real material.

In summary, the exploration of the excitonic mechanism is still proceeding. Unlike phonon mediation, using the exciton concept the specific character of the boson being exchanged between electrons is not identified. In Chapter 6, we will describe our work although it is still at an early stage.

Chapter 5: 2D interface metallicity and possible superconductivity

In this chapter, two dimensional (2D) metallicity and possible superconductivity at the interfaces of two different semiconductors is discussed. First, we review the properties of bulk CuCl, its electronic structure and peculiar physics, such as phonon anomaly and speculated, but not confirmed, superconductivity, once hot topics in condensed matter physics. Second, the results on CuCl/Si superlattices for both [111] and [001] growth directions are presented, as are results on other superlattices of hetero-bonded semiconductors, namely ZnS/Si and GaP/Si. For all these materials, we estimate the electron-phonon coupling constant, λ, using the crude rigid muffin-tin approximation (RMTA). As we shall see, the electron-phonon coupling is present mostly at the interfaces. However, what makes the CuCl/Si superlattices special is that only they show possible superconductivity even in the framework of phonon mediated pairing, while the others do not.

5.1 Introduction

Recent advances in materials synthesis and epitaxial growth techniques have attracted much interest in the physics of hetero-interfaces between materials with either different polarity or oxidation states. The polarity discontinuity in semiconductor hetero-interfaces such as GaAs/Ge [001][93,94,95] or III-V alloys on Si [001][96] has been well studied. For oxide hetero-interfaces, the layer-by-layer growth of the $LaTiO_3/SrTiO_3$ and $LaAl_3/SrTiO_3$ superlattices have attracted recent attention.[97,98,99,100] Despite the fact that these consist of two insulators in their bulk form, metallic conductivity was observed in the experiments.[97,99]

Actually, interest in superlattices and hetero-interfaces, goes back several decades. A possible superconducting state in a metal sandwiched by dielectric materials was proposed in the early 1960's advancing the so-called "excitonic mechanism" of superconductivity.[9,10] It was emphasized that a much higher transition temperature (T_C) might be achieved by excitonic mediation. Several geometries were suggested as candidates for the excitonic mechanism: (a) metallic "chains" or strings with polarizers placed alongside them[9] and, (b) dielectric-metal-dielectric sandwiches, where the conduction electron states are surrounded by a dielectric medium.[10] The dielectric-metal-dielectric geometry was studied theoretically by Allender, Bray and Bardeen (ABB)[11] with a model metal-dielectric interface. Following ABB, some experimental efforts to observe superconductivity in several systems include: (a) clean PbTe surfaces,[101] (b) ultra-thin Al films on Si,[102] (c) eutectic alloys[103] (Al-Ge and Al-Si), (d) ultra-thin Pb, In, and Tl-layer deposited on PbTe.[104] However, superconductivity was not confirmed in any of them. Then in 1978, nearly ideal diamagnetism was observed in bulk CuCl by Brandt *et al.*[105] and Chu *et al.*.[106] Shortly thereafter, Abrikosov proposed the formation of "metallic excitonium"[107,108] to ex-

plain their observation, but again this was never fully confirmed. Later, Mattes and Foiles studied epitaxially grown CuCl on a Si [111] substrate.[12] They found that it is diamagnetic when the applied field is perpendicular to the interface while it is paramagnetic when the applied field is parallel to the interface. Moreover, the diamagnetism was nearly ideal between 60 and 150 K. In a following work, Mattes speculated further on the possible superconducting origin of the observation because of a sudden drop of resistivity by 5 orders of magnitude at 77 K.[109]

After the work by Mattes and Foiles, a preliminary first-principles investigation on the possible interfacial superconductivity in CuCl/Si was reported by Yu and Freeman.[13] From the results of electronic structure calculations with a $(CuCl)_1/(Si)_4$ superlattice model, the existence of 2D metallic states at the interface was considered to be plausible. The present work is a continuation and extension of this first study. We consider first the [111] superlattices $(CuCl)_n/(Si)_{4n}$, with $n = 1$ to $n = 3$.[a] We also consider [001] superlattices, $(CuCl)_n/(Si)_m$,[b] namely $(CuCl)_2/(Si)_8$ $[2/8]$, $(CuCl)_4/(Si)_8$ $[4/8]$, and $(CuCl)_4/(Si)_{12}$ $[4/12]$. The presence of 2D metallic states localized at the CuCl/Si interfaces is shown by the band structures, Fermi surfaces and charge densities. Thus, the CuCl/Si superlattices can be viewed not only as the hetero-interfaces of two different semiconductors but also as the dielectric-metal-dielectric sandwich structure proposed by Ginzburg for excitonic superconductivity.[10]

As a step toward understanding the physics of the interface metallic states and to in-

[0a] In the $n = 2$ [111] superlattice, we found that the CuCl becomes unstable. Thus, we exclude the $n = 2$ case in this work.

[0b] n is an integer and m is an even integer. $2n + m$ should be a multiple of 4 to satisfy the periodicity along the [001] direction.

vestigate a possible superconductivity at the CuCl/Si hetero-interface, we carried out first-principles electronic structure calculations for the CuCl/Si superlattices using the highly precise all-electron full potential linearized augmented plane wave (FLAPW) method,[14,15] and also estimated T_C considering the electron-phonon mechanism. In Sec. 5.3, the geometry of the [111] and [001] CuCl/Si superlattices and computational details are described. The results for relaxed superlattices are discussed in Sec. 5.3.2. The two dimensional metallicity is presented in Sec. 5.3.3, along with an analysis of the band structure, Fermi surfaces and charge densities. The projected density-of-states (pDOS) of the superlattices around E_F is provided in Sec. 5.3.4 to identify conduction carriers. These comparisons give a basic idea as to how the bonding character is changed. The interface charge of superlattices is discussed in Sec. 5.3.5. Finally, in Sec. 5.3.6, to discuss the possible superconductivity in these superlattices, T_C is estimated using the conventional electron-phonon interaction in the crude rigid muffin-tin approximation (RMTA).[21] Most of the electron-phonon coupling responsible for superconductivity is present at the interfaces, and results in a T_C of 0.03$\sim$4.40 K

5.2 Bulk CuCl

In the late 70's and early 80's, CuCl was one of the hottest materials in condensed matter physics for its possible high temperature superconductivity. More specifically, it was debated whether it revealed ideal diamagnetism under hydrostatic pressure. In addition to this speculated superconductivity, CuCl has attracted a lot of interest due to its unusual physical properties, such as a complicated pressure-driven phase diagram, phonon anomalies, and

negative compressibility. Furthermore, CuCl has a direct band-gap (3.4 eV) at the Γ point with a 60 meV spin-orbit splitting energy.[110,111] The valence top results from the hybridization of highly localized Cu *d* and Cl *p* states. In addition, spin-orbit splitting in CuCl at Γ different from that in other tetrahedrally coordinated direct band-gap semiconductors. The uppermost valence band is twofold degenerate with Γ_7 symmetry, while the next lower is fourfold degenerate with Γ_8 symmetry. This is in big contrast to other tetrahedrally coordinated direct band gap semiconductors, where most of them exhibit fourfold (Γ_8 symmetry) degeneracy for the uppermost valence band state and twofold degeneracy (with Γ_7 symmetry) for the next lower states. The rest of this section is devoted to a summary of some interesting physics of CuCl.

Structural instability with respect to pressure

High pressure studies of CuCl has led to interesting observations of a peculiar sequence of phase transitions.[112,113,114] At ambient temperature and pressure, CuCl crystallizes into a zinc-blende(ZB) structure with a lattice constant of 5.42Å. As pressure increases, the ZB-structure undergoes a phase transition via an intermediate phase called CuCl-IIa, to a CuCl-IV cubic structure phase, and finally to the NaCl structure of CuCl-V at pressures above $\sim$10 GPa. These are connected to the complex anomalous behavior of the optical properties and to the claims of high-temperature superconductivity.

Phonon anomalies

In the mid 1990's, the phonon anomalies of CuCl in Raman spectra were very controversial.[115,111,116] The unusual double-peak structure of the optical phonon modes, where the TO mode is broadened or has multiple peaks, initiated a series of studies in both experiment and theory. Two different explanations have been suggested for the anomalous

phonon structure. (i) the Fermi resonance model[115,117,111,118,119] and (ii) the off-center DX model.[120,121,122] The Fermi resonance model suggested an anharmonic coupling of the transverse optical phonon to the resonant acoustic two-phonon states, which results in a shift and broadening of the optical phonon mode and a transfer of oscillator strength to two-phonon scattering. On the other hand, in the off-center DX model, the anomaly is attributed to the local vibrations of the Cu ions occupying the off-center positions along [111] anti-bonding directions, which is often observed as a DX-center defect in ZB semiconductors. To our knowledge, the debate on this phonon anomaly is not resolved yet.

Superconductivity?

In the late 70's, diamagnetism in CuCl was observed under hydrostatic pressure,[105,106] which was followed by many experiments but never fully confirmed. It was then believed that CuCl was an indirect band gap material, and based on this false band structure, Abrikosov proposed "metallic excitonium" to explain a possible electron-hole interacting pairing mechanism,[107] which is an analogue to electron-phonon mediation replacing the mass of nuclei with the mass of a hole. Although it was once very controversial whether CuCl was direct or indirect band gap material, it turns out that CuCl is a direct band gap material.[123] However, Abrikosov's idea is interesting in the sense that it provided one possible theoretical picture of an exciton mechanism. The vibration of the lattice of heavy holes would behave exactly in the same way as in lattice vibrations *or* phonons.

There has been abundant theoretical[124,125] and experimental[114,126,127] efforts to investigate superconductivity; or at least diamagnetism in CuCl, but no confirmation was ever made on superconductivity.

5.3 CuCl/Si superlattices

5.3.1 Geometry and computational aspects

CuCl and Si crystallize in the zinc-blende and diamond structures, respectively, with similar lattice constants, 5.42Å (CuCl) and 5.43Å (Si). In the [111] case, the superlattice is constructed to satisfy the periodicity along the [111] direction in the zinc-blende structure. The resulting hexagonal crystal structure is shown schematically in Fig. 5.1 for the $n = 3$ case with the hexagonal lattices in the *ab* plane. For the [001] case, on the other hand, the superlattice forms a square lattice in the *ab* plane as shown in Fig. 5.2.[c] Four atomic layers is one unit of the *c* direction periodicity, which results in $(CuCl)_n/(Si)_m$. We performed structural optimizations, *i.e.* of the volume and internal coordinates, for all cases, and we employed the highly precise full-potential linearized augmented plane wave (FLAPW)[14,15] method in the local density approximation (LDA), with the exchange-correlation potential formulated by Hedin and Lundqvist.[3] We used muffin-tin (MT) radii of 2.15 a.u. (Cu), 2.00 (Si and Cl), and spherical harmonics with $\ell \leq 8$ inside the MT spheres. The cut-off energy of the plane wave basis was 3.8 a.u, while that of the potential representations were 14.4 a.u. and 12.0 a.u. for the [111] and the [001] cases, respectively. The improved tetrahedron method[23] is used for *k* point integrations, with 119 ($n = 1, 3$), 98 ($2/8$), 128 ($4/8$), and 243 ($4/12$) points in the irreducible Brillouin zone. The optimized lattice constants for all superlattices are tabulated in Table 5.3.1, where the numbers in parentheses are the change (in %) relative to those of the bulk zinc-blende structure.[d]

[c] In the [001] superlattice, the first four layers are labeled as Si[1], Si[2], Si[3], and Si[4]. We put CuCl layers on top of the first four Si layers and then put the rest of the Si layers on the CuCl layers.

[d] The a used for the comparison is 5.43Å.

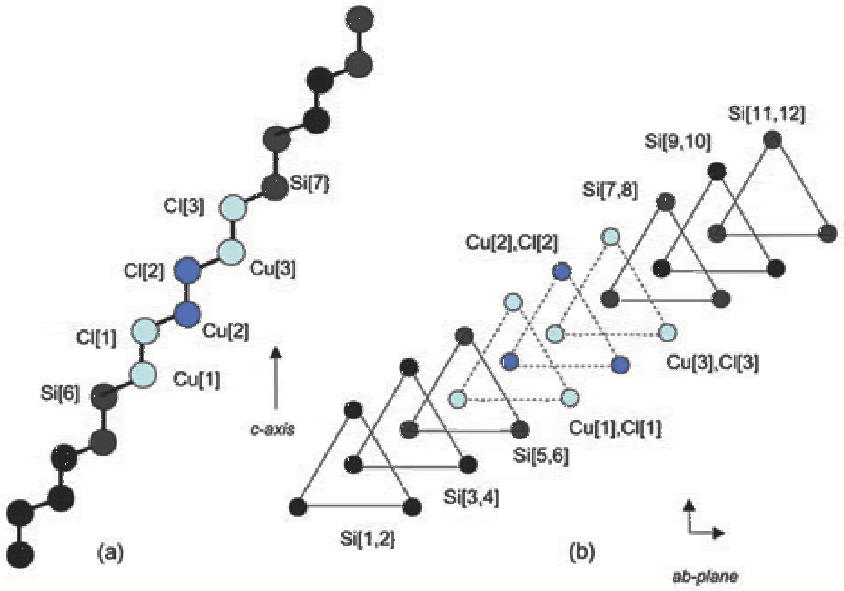

Figure 5.1: Schematic drawing of the $n = 3$ CuCl/Si superlattice: (a) side view; (b) top view.

	n=1	n=3	$2/8$	$4/8$	$4/12$
a(Å)	5.59 (3.06%)	5.44 (0.45%)	5.38 (-0.8%)	5.30 (-2.22%)	5.34 (-1.45%)
c/a	2.28 (-7.02%)	7.06 (-3.99%)	3.02 (+0.77%)	4.16 (+3.92%)	5.11 (+6.83%)

Table 5.1: Optimized lattice constants (a) and c/a ratio for the superlattices. For the [111] superlattices, lattice constants are converted to those of zinc-blende. The numbers in parentheses are the relative change (in %) of a and c/a to those of the zinc-blende structure without relaxation.

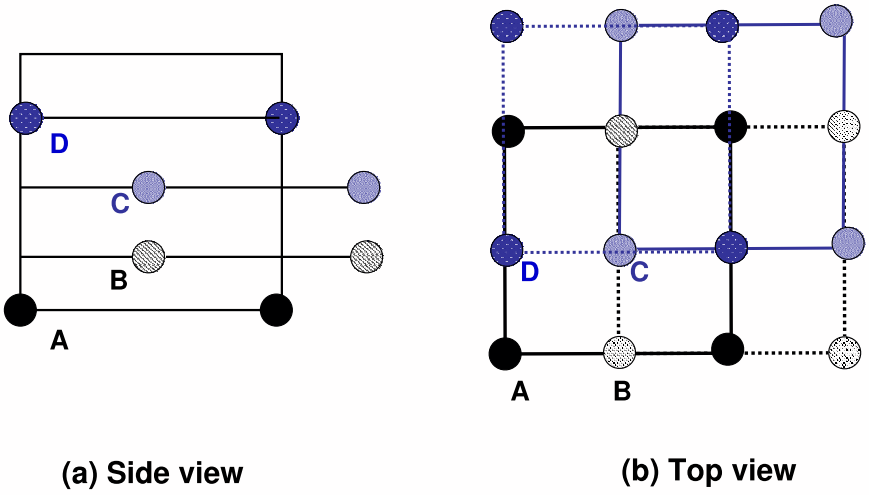

Figure 5.2: Schematic drawing of the [001] CuCl/Si superlattice: (a) side view of one zinc-blende cell; (b) top view. Stacking order is A-B-C-D type as indicated in figure, and represent, e.g., Si[1], Si[2], Si[3], and Si[4], or Cu[1], Cl[1], Cu[2] and Cl[2].

n=1	change(%)	n=3	change(%)
Si[4]-Si[3]	5.14	Si[7]-Cl[3]	-30.75
Si[3]-Cl	-39.27	Cl[3]-Cu[3]	7.13
Cl-Cu	15.69	Cu[3]-Cl[2]	-41.97
Cu-Si[2]	-33.51	Cl[2]-Cu[2]	11.65
Si[2]-Si[1]	4.00	Cu[2]-Cl[1]	-56.83
Si[1]-Si[4]	-1.71	Cl[1]-Cu[1]	10.38
		Cu[1]-Si[6]	-6.61

Table 5.2: The [111] superlattice: percentage change of layer distances before and after relaxation. The changes of layer distances not listed are less than 5%.

Layer	$2/8$	Layer	$4/8$	$4/12$
Si[5]-Cl[2]	6.71	Si[5]-Cl[4]	43.84	43.88
Cl[2]-Cu[2]	0.95	Cl[4]-Cu[4]	-10.91	-11.58
Cu[2]-Cl[1]	-16.85	Cu[2]-Cl[1]	-9.99	-11.05
Cl[1]-Cu[1]	15.13	Cl[1]-Cu[1]	11.29	11.74
Cu[1]-Si[6]	-4.31	Cu[1]-Si[6]	-1.00	-0.40

Table 5.3: The [001] superlattice: percentage changes of layer distances before and after relaxation. The changes of layer distances not listed is less than 5%.

In the following, we show in detail the band structure and Fermi surfaces (FS), as well as the density-of-states (DOS) around E_F. Then we discuss charge transfer in relation to the origin of the 2D metallic states at both the Cu/Si and Cl/Si interfaces.

5.3.2 Structural relaxation

The layer-by-layer distances after relaxation with optimized lattice constant a, and the c/a ratio are compared with those of the zinc-blende structure without relaxation. The percentage changes of layer distance are tabulated in Table 5.3.1 for the [111] case and in Table 5.3 for the [001] case.

First, in the [111] superlattices, the Si-Si layer distance changes are within 5% relative to the zinc-blende structure, but are much larger for the other layers: in the $n = 1$ case, the Si[3]-Cl, Cu-Si[2], Cu-Cl distance changes indicate that the Cl/Si and Cu/Si interfaces are strongly affected by relaxation, suggesting that an increase of bonding between them occurs with relaxation, while the Cu-Cl bonding is weakened. In the $n = 3$ case, the Si[7]-Cl[3] distance change is much larger than the Cu[1]-Si[6] distance change. The Cu-Cl distance changes in the CuCl region are driven by the increase of the Cu-Cl distance in the bonds along the [111] direction.

Second, in the [001] superlattices, the Cl-Si layer distance increases by 6.7%, 43.8%, and 43.9%, for the $2/8$, $4/8$, and $4/12$ cases, respectively; the Cu-Si distances decrease by much less than in the [111] case and are not as systematic. However, the fact that the CuCl region is more affected than the Si region is similar to that of the [111] superlattices.

5.3.3 2D metallic states

The band structures for the two growth directions, i.e. [111] and [001], are shown in Figs. 5.3 and 5.6, respectively. It is notable that metallic states are found in both cases to arise at the interface of two semiconductors with band gaps 3.4 eV (CuCl) and 1.14 eV (Si) in their bulk. In the [111] superlattices, two bands cross E_F, where the hole (electron) band is labeled as $h(e)$ in Fig. 5.3. The character of the hole band is mostly Cu(*d*)-Si(*p*), while that of the electron band is mostly Cl(*p*)-Si(*p*), which clearly characterizes and distinguishes the two interfaces: in the $n = 1$ case, one can see a tendency to low dispersion along the $M - L$ and $A - \Gamma$ directions; in the $n = 3$ case, the dispersion along these directions almost vanishes, indicating strong two dimensionality.

The Fermi surfaces of the [111] superlattices are depicted in Fig. 5.4. The inner sheet from the hole band (labeled as h) forms an open cylindrical shape centered at the Γ point, while the outer sheets from the electron band (labeled as e) are located at the corners of the Brillouin zone. For $n = 1$, the electron band sheet is connected, whereas for $n = 3$ there are multiple sheets. The low dispersion of the Fermi surfaces along the *c* direction reflects the two dimensionality of the superlattices, and the 2D interface metallicity is further illustrated in a charge density plot [*c.f.* Fig. 5.5].

For the charge density, only the electronic states within an energy slice of 0.025 eV below E_F are taken into account. In both the $n = 1$ and $n = 3$ cases, most of the charge is located at the Cu/Si and Cl/Si interfaces. The 2D character of the conducting charge is clearly manifested in the $n = 3$ case. Note that the superlattice is divided into metallic plane (the Cu/Si and the Cl/Si interfaces) and dielectric regions (the CuCl and the Si regions).

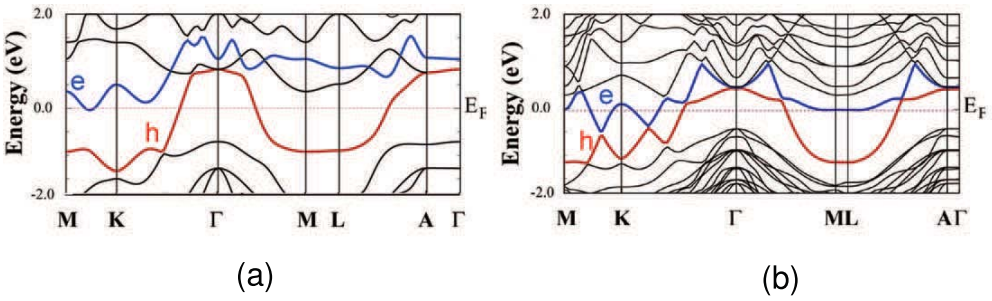

Figure 5.3: Band structure of the [111] superlattice: (a) $n = 1$ and (b) $n = 3$. The hole (electron) band, in red (blue), is labeled as h (e). $L = (\pi/a, 0, \pi/c)$ and $A = (0, 0, \pi/c)$, respectively.

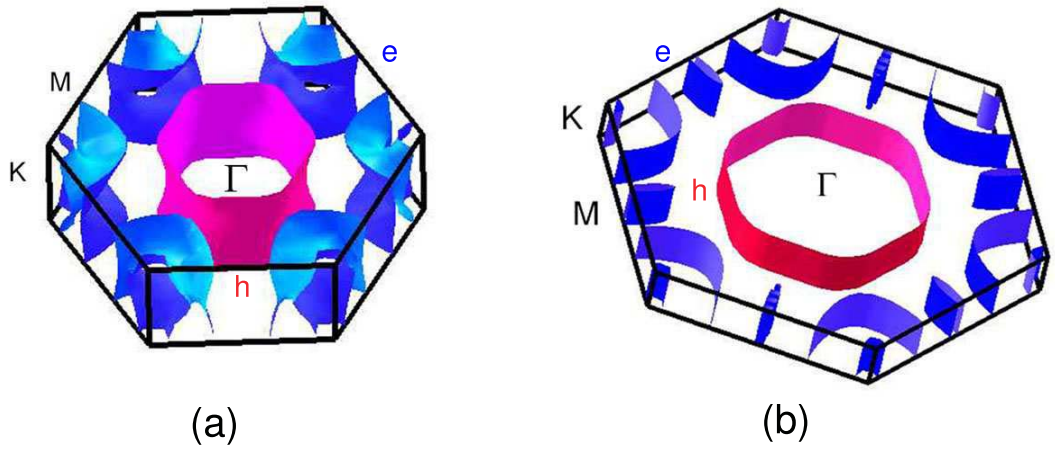

Figure 5.4: Fermi surfaces of the $[111]$ superlattice: (a) $n = 1$ and (b) $n = 3$. Sheets from the hole (electron) band, in red (blue), is located at the zone center (zone corner) and labeled as $h(e)$.

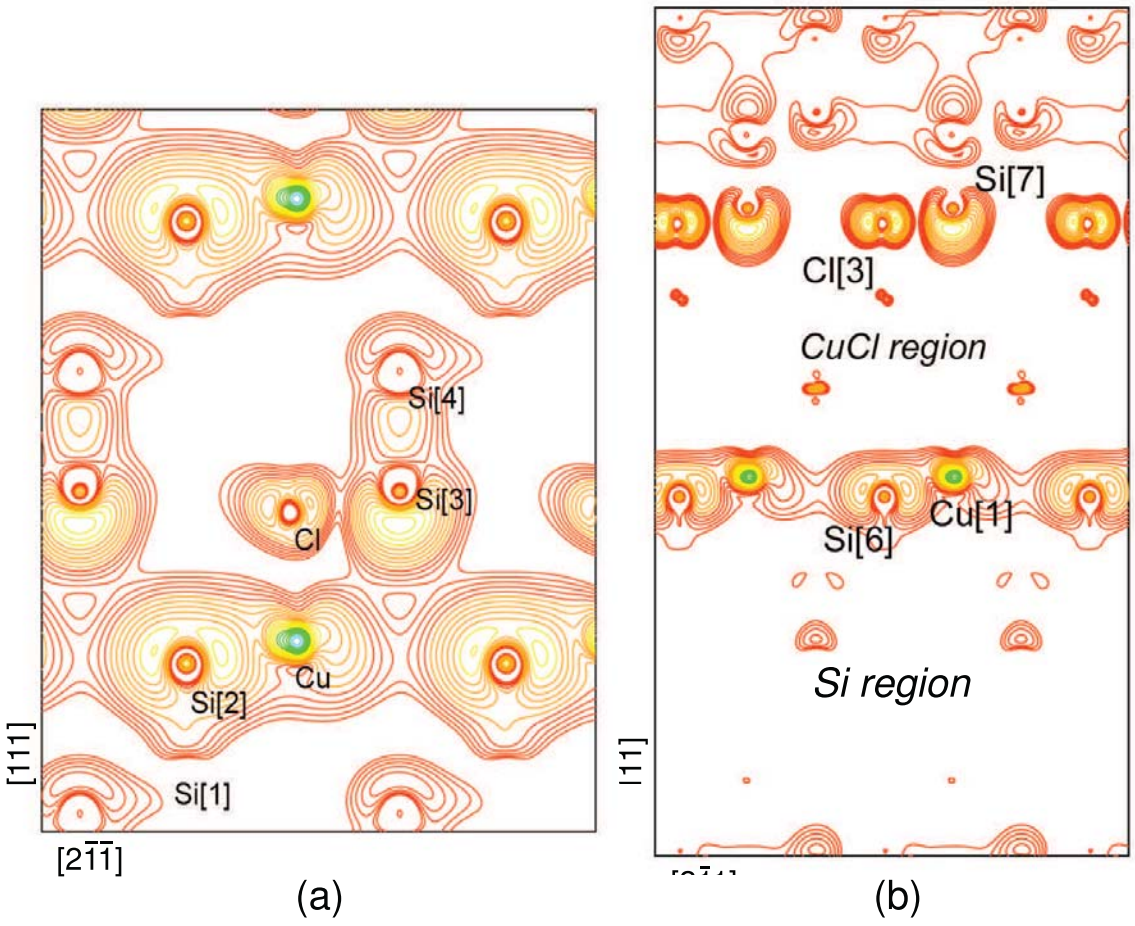

Figure 5.5: Charge density contour plot of the (a) $n = 1$ and (b) $n = 3$ superlattice around E_F within an energy slice of 0.025 eV; the starting density is 1.0×10^{-4} e/a.u.^{3} and subsequent lines increase by factor of 1.25.

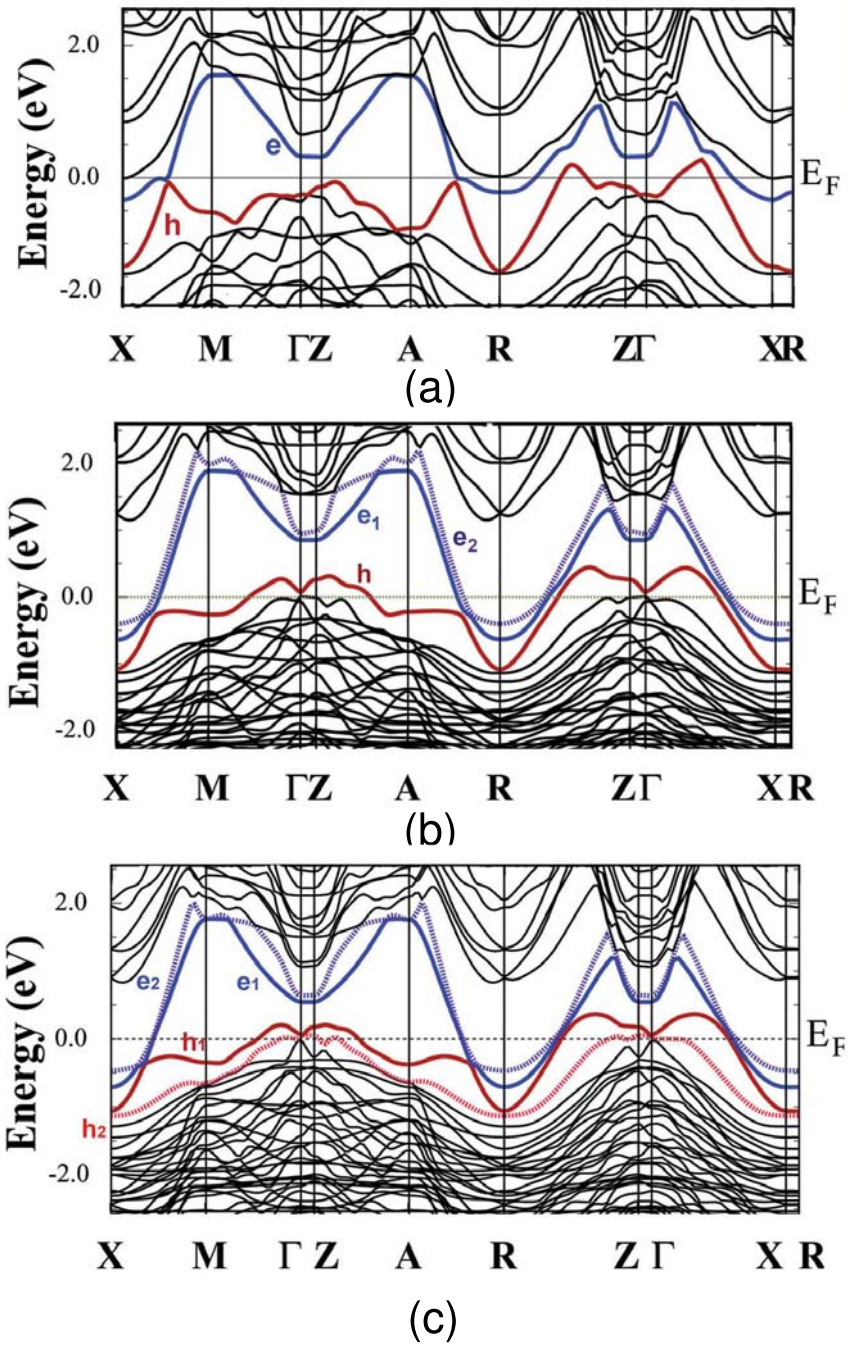

Figure 5.6: Band structure of the [001] superlattice: (a) $2/8$, (b) $4/8$, and (c) $4/12$. The hole (electron) band, in red (blue), is labeled as h (e). The symmetry points are $M = (\pi/a, \pi/a, 0)$, $Z = (0, 0, \pi/c)$, $R = X + (0, 0, \pi/c)$, and $A = M + (0, 0, \pi/c)$, respectively.

The band structures of the [001] superlattices are shown in Fig. 5.6 for the: (a) $2/8$, (b) $4/8$, and (c) $4/12$ cases. Again metallic states are found in all cases, with the hole (electron) bands again labeled as h (e). In the $2/8$, two bands cross E_F, while in the $4/8$ and the $4/12$ cases, three and four bands cross E_F, respectively. The band dispersions in the three cases are similar, but the positions of the bands with respect to E_F are different: compared to the $2/8$ case, the electron bands are pushed downward along the $X - R$ line in the two other cases; in contrast, the hole bands are pushed upward along the $\Gamma - Z$ line. As in the [111] superlattice, the band character is mostly Cu(*d*) -Si(*p*) for the hole bands, and Cl(*p*)-Si(*p*) for the electron bands. The dispersion along the *c* direction (along $\Gamma - Z$ and $X - R$) is weak but not as weak as in the [111] case for the hole bands, in particular.

The Fermi surfaces of the [001] superlattices are shown in Fig. 5.7. In the $2/8$ case, the inner sheet which is from the hole band, has a double lip structure symmetric with respect to the $\Sigma - \Gamma - \Sigma$ line, whereas the outer sheet, which is from the electron band, is centered around the corner points (X) and parallel along the *c* direction. In the $4/8$ and $4/12$ cases, the inner hole band sheet has a simply connected structure centered at Γ, whereas the outer electron band sheets are centered around the corner points (X) and parallel along the *c* direction, as in the $2/8$ case. In the $4/12$ case, however, an additional sheet with connected ribbon-shape in the zone center is found, which is from hole band $h2$ in Fig. 5.6(c). The 2D character of the [001] superlattices is well manifested in the Fermi surfaces as in the [111] case.

The charge density plot of the [001] superlattice is given in Fig. 5.8 for the: (a) $2/8$, (b) $4/8$, and (c) $4/12$ cases, respectively; the interfaces are labeled for both the Cu/Si and Cl/Si interfaces. Again, most of the charge is found at the interfaces, but is spread out more

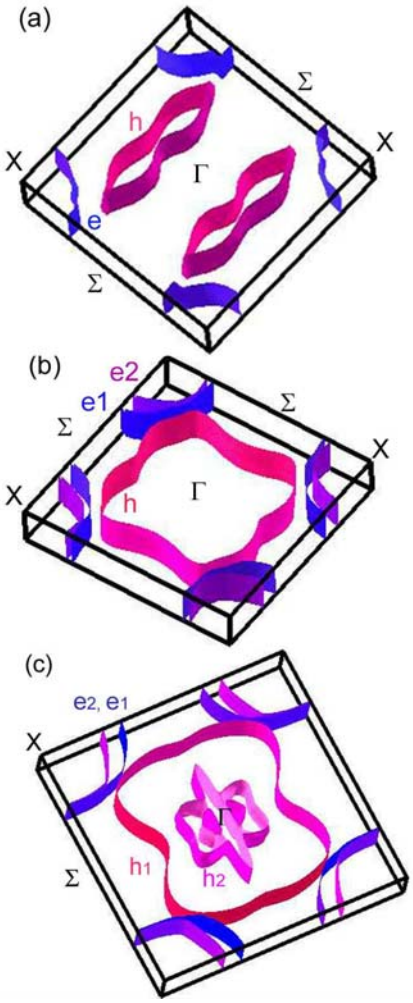

Figure 5.7: Fermi surfaces of the [001] superlattice: (a) $2/8$, (b) $4/8$, and (c) $4/12$. Sheets from the hole (electron) band, in red (blue) is located at zone center (zone corner) and labeled as $h(e)$. Corner point of the BZ is denoted by its label. Corner point of the BZ is denoted by its label, where $\Sigma = M/2 = (\pi/2a, \pi/2a, 0)$.

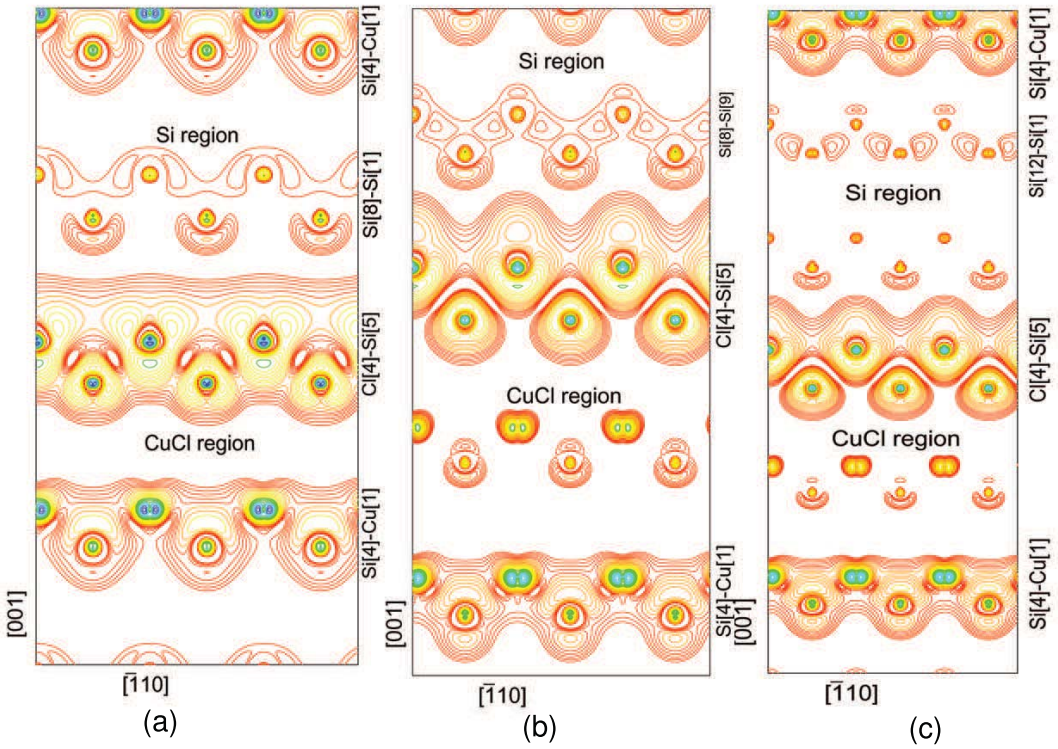

Figure 5.8: Charge density contour plot of the (a) $2/8$, (b) $4/8$, and (c) $4/12$ superlattice around E_F within an energy slice of 0.025 eV. The interface, CuCl and Si regions are labeled. The starting density is 5.0×10^{-4} e/a.u.^{3} and subsequent lines increase by a factor of 1.25.

from the interfaces compared to the [111] case. The metallicity in the Cu/Si interface is confined to the interface, whereas the Cl/Si interface has some conducting charge spread to the Si region. Clearly, in the [001] case as in the [111] case, the interfaces form metallic slabs with the CuCl and Si region remaining essentially dielectrics.

5.3.4 Density of States

As expected from the band structures, Fermi surfaces and charge densities, the interface atoms contribute differently from the other atoms to the partial density of states (pDOS) at E_F. We present the DOS of the $n = 3$ [111] and $4/12$ [001] cases only since the trends of the DOS in the other cases [$n = 1$ (111) and $2/8$, and $4/8$ (001)] are the same.

First, in the $n = 3$ case , the pDOS of Si[5], Si[6], Cu[1], Cl[1] are shown in Figs. 5.9 (a)-(d); these correspond to the Cu/Si interface. The pDOS of Cu[3], Cl[3], Si[7], Si[8] are shown in Figs. 5.9 (e)-(h); these correspond to the Cl/Si interface. Both Cl[1] and Si[5] have negligible DOS at E_F, while Cu[1] and Si[6] have high DOS at E_F. Conversely, for atoms at the Cl/Si interface, Cl[3] and Si[7] have a strong DOS at E_F, while that of Cu[3] and Si[8] are negligible.

Second, in the $4/12$ [001] case, the pDOS of Si[3], Si[4], Cu[1], and Cl[1], corresponding to the Cu/Si interface are shown in Figs. 5.10(a)-(d); the pDOS of Cu[4], Cl[4], Si[5], and Si[6], corresponding to the Cl/Si interface are shown in Figs. 5.10(e)-(h). At the Cu/Si interface side, the DOS at E_F of Cu[1] and Si[4] is large, while that of Si[3] is not negligible but smaller than those at the interfaces. The Cl/Si interface exhibits a pattern similar to the Cu/Si interface: the interface atoms (Si[5] and Cl[4]) have a large DOS value at E_F, while the Si[6] has a non-negligible DOS at E_F but is smaller than those at the in-

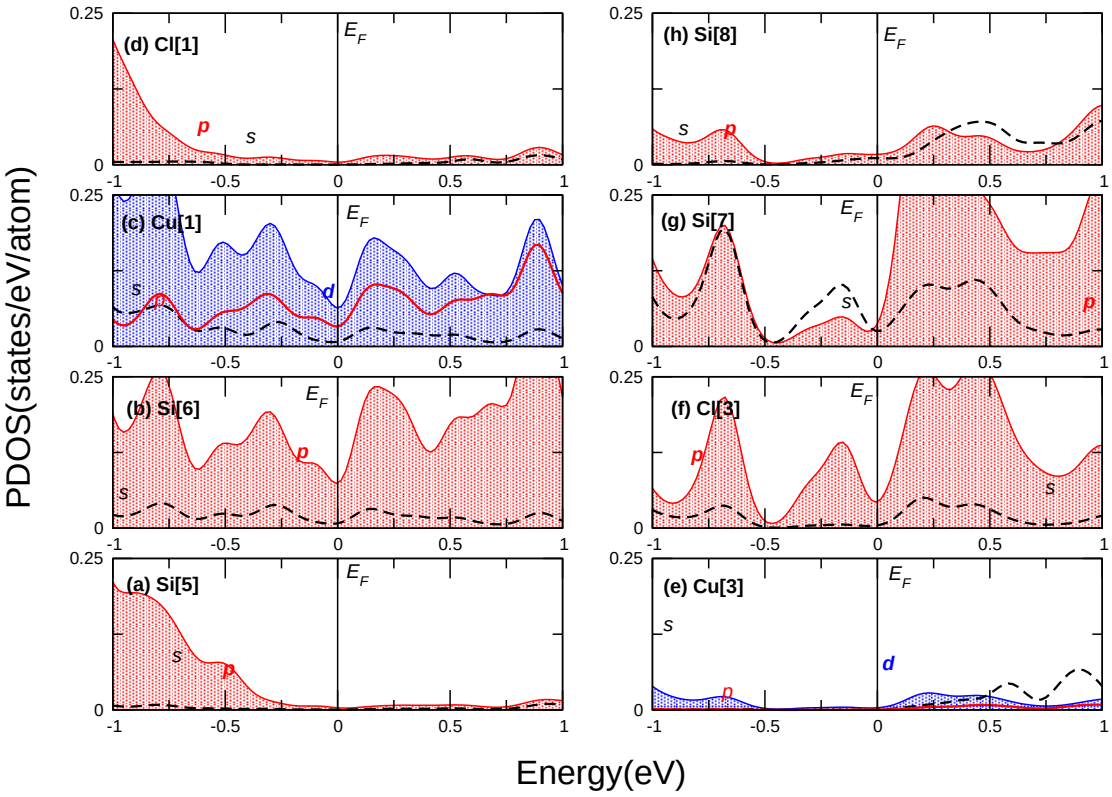

Figure 5.9: PDOS around the Fermi energy of the $n = 3$ superlattice. The pDOS of the interface atoms (Si[4],Cu[1], Cl[2],Si[5]) and of some of other atoms are shown. (a) Si[5], (b) Si[6], (c) Cu[1], (d) Cl[1], (e) Cu[3], (f) Cl[3], (g) Si[7], and Si[8]. The *s* orbitals pDOS are shown by the black dotted line; the *p* by the red solid line. For Si and Cl atoms, the area below the pDOS of *p* orbitals is shown lightly shaded (in red); for Cu atoms, the area below the pDOS of *d* orbitals is shown heavily shaded (in blue).

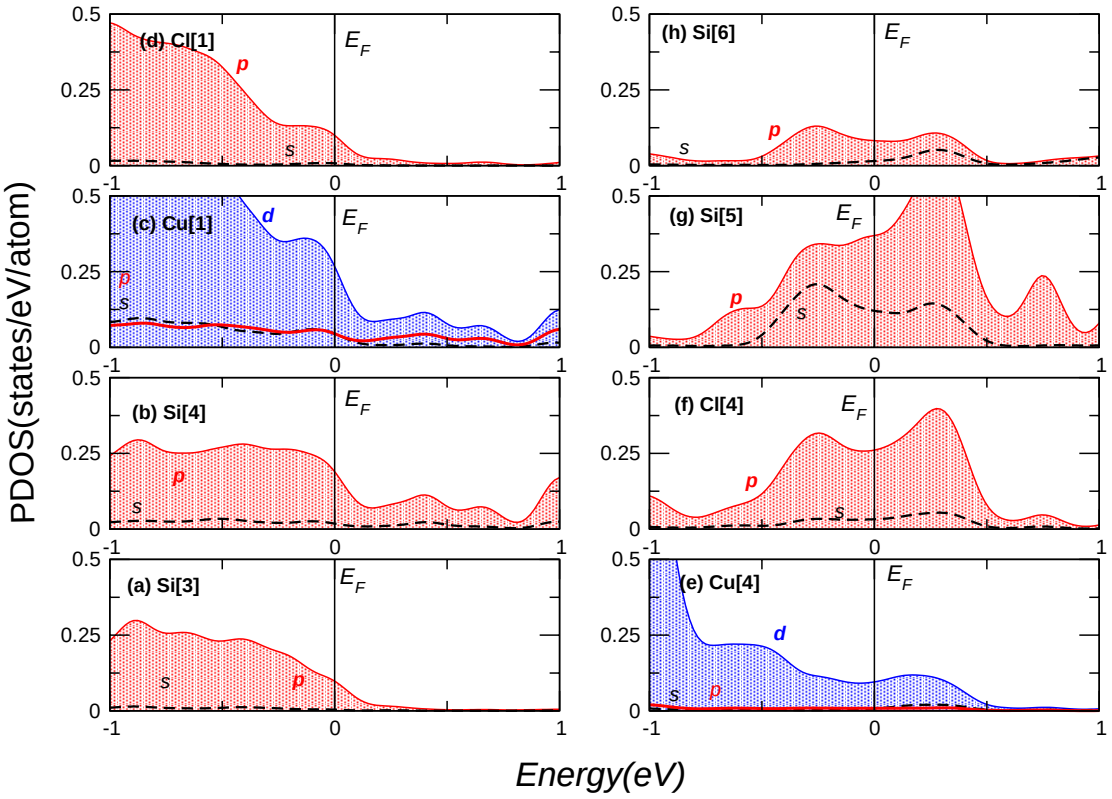

Figure 5.10: PDOS around the Fermi energy of the $4/12$ superlattice. The pDOS of the interface atoms (Si[4],Cu[1], Cl[2],Si[5]) plus some of other atoms are shown. (a) Si[3], (b) Si[4], (c) Cu[1], (d) Cl[1], (e) Cu[4], (f) Cl[4], (g) Si[5], and Si[6]. The *s* orbitals are given by the black dotted line; the *p* by the red solid line. For Si and Cl atoms, the area below the pDOS of *p* orbitals are shown lightly shaded (in red); for Cu atoms, the area below the pDOS of *d* is shown heavily shaded (in blue).

terfaces. Both Cl[1] and Cu[4], however, as in the $n = 3$ case, have negligible DOS at E_F. The non-negligible DOS at E_F of Si atoms (Si[3] and Si[6]) is consistent with the charge density plot: charge is more spread away from the interface to the Si region compared to the [111] superlattice.

5.3.5 Interface charge

For the quantitative analysis of interface charge, changes of the MT charges (in %) relative to their bulk counterparts are listed in Table 5.4 for the $n = 3$ and $4/12$ cases. The interface Si atoms lose their charge while the interface Cu and Cl gain charge. One thing common to [111] and [001] is that the interface Cu loses its *d* charge but gains *s* charge, while the interface Si gains *s* charge but loses *p* charge. While the bonding nature of bulk Si (CuCl) is covalent (ionic), new bondings are formed at the interfaces - as seen in the change of layer distances and charge densities.

A schematic of bonding is illustrated in Fig. 5.11 for the: (a) [111] and (b) [001] superlattices. Since all atoms are tetrahedrally coordinated, there are four bonds per atom. For simplicity, we present only three arms for the [111] case. According to the two-electron-per-bond counting rule, each atom, Si, Cu, and Cl has $1,\ 1/4$, and $7/4$ electrons per bonding arm, respectively. The Cu-Si arm lacks $3/4$ electrons, whereas the Cl-Si arm has an excess of $3/4$ electrons. This simple electron counting per bond explains very well why the Cu/Si interface is p-type and the Cl/Si interface is n-type.

$n=3$	s	p	d	$4/12$	s	p	d
Si[6]	3.67	-8.18		Si[4]	2.09	-4.97	
Cu[1]	2.10	0.43	-2.02	Cu[1]	1.54	0.21	-1.60
Cl[3]	1.29	-1.01		Cl[4]	0.48	-0.45	
Si[7]	10.55	-14.31		Si[5]	2.96	-3.38	

Table 5.4: Relative changes (in %) of the orbital resolved MT charges of the interface atoms in the $n=3$ [111] and $4/12$ [001] superlattices with respect to bulk Si and CuCl.

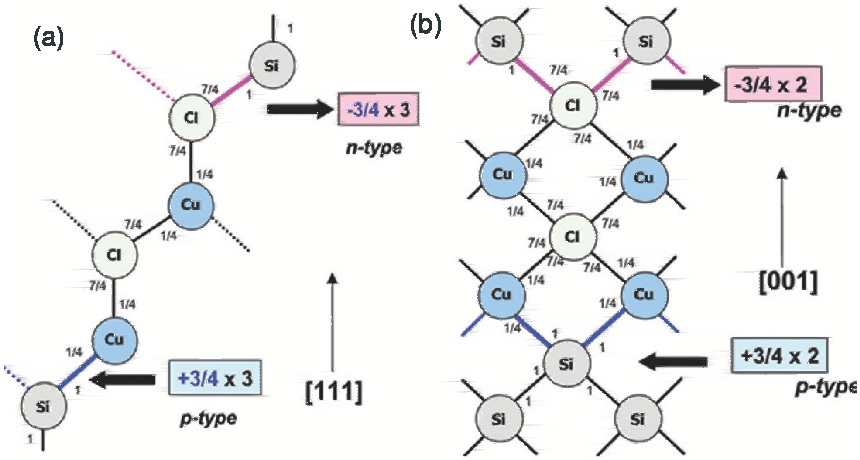

Figure 5.11: Schematic illustration of bondings in superlattices (a) [111], and (b) [001]. The average number of electrons per bond is shown for each bond. The p-type interface lacks $3/4$ e^- charge per bond and the n-type interface has an excess of $3/4$ e^- electronic charge per bond. In the [111] case, one bond is not shown.

5.3.6 Superconductivity

The presence of the 2D metallic states surrounded by dielectric layers can provide a system close to the model for excitonic superconductivity originally suggested by Ginzburg[10] and ABB.[11] The experiment by Mattes and Foiles, where a large diamagnetic signal for epitaxially grown CuCl on a Si [111] substrate was observed between 60∼150 K, motivates us to first estimate T_C for our CuCl/Si superlattices based on the BCS-type electron-phonon coupling mechanism. Although a 2D formulation of superconductivity would be more appropriate for the present system, it would be beyond the scope of this work. In the following, we use a standard 3D approach because it can still shed some light on electron-phonon coupling and superconductivity in our system. Thus, we estimate the McMillan-Hopfield[20,85] electron-phonon coupling constant, λ_{ep}, which can be written $\lambda_{ep} = \sum_t \eta_t / M_t \langle \omega^2 \rangle$.[128] The spherically averaged Hopfield parameter for each atom type, η_t, calculated in the crude RMTA[21,83] is

$$\eta = 2N(E_F) \sum_l (l+1) M_{l,l+1}^2 \frac{f_l f_{l+1}}{(2l+1)(2l+3)}, \tag{5.1}$$

where $f_l = N_l(E_F)/N(E_F)$ is a fractional pDOS of a given atom and $M_{l,l+1}$ is an electron-phonon matrix element given by

$$M_{l,l+1} = \int_0^R R_l \frac{dV}{dr} R_{l+1} r^2 dr, \tag{5.2}$$

with the gradient of the potential and radial functions R_l and R_{l+1} calculated at E_F. According to Pettifor[129] and Glözel *et al.*,[130] Eq. (5.2) can be rewritten [see also Skriver *et al.*[83,84]] as

$$\begin{aligned} M_{l,l+1} &= -\phi_l(E_F)\phi_{l+1}(E_F) \\ &\times \{[D_l(E_F) - l][D_{l+1}(E_F) + l + 2] + [E_F - V(S)]S^2\} \end{aligned} \tag{5.3}$$

where $V(S)$ is the one-electron potential and $\phi_l(E_F)$ the amplitude of the l partial wave at the sphere-boundary (radius $= S$) evaluated at E_F. The average phonon frequency can be estimated by $\langle\omega_t^2\rangle^{1/2} = 0.69\ \Theta_D^t$, where Θ_D^t is the Debye temperature and t is the atom type index. We took experimental values for Θ_D, 625 K for Si[54] and 180 K for CuCl,[131] and evaluated the electron-phonon coupling constant as

$$\lambda_{ep} = \sum_{Si} \frac{\eta(Si)_t}{M_{Si}\langle\omega_{Si}^2\rangle} + \sum_t \frac{\eta(Cu)_t + \eta(Cl)_t}{\frac{1}{2}M_{CuCl}\langle\omega_{CuCl}^2\rangle}, \tag{5.4}$$

where the average mass of CuCl was used for Cu and Cl.[132,e] To estimate T_C we used McMillan's formula[20]

$$T_c = \frac{\langle\omega^2\rangle^{1/2}}{1.2} \exp\Big[-\frac{1.04(1+\lambda_{ep})}{\lambda_{ep} - \mu^\star(1+0.62\lambda_{ep})}\Big]. \tag{5.5}$$

The average phonon frequency is again evaluated with $\langle\omega^2\rangle^{1/2} = 0.69\langle\Theta_D\rangle$, where Θ_D is the weighted-average of Θ_D for Si and CuCl. The electron-phonon coupling constant (λ_{ep}), the Coulomb pseudopotential ($\mu^\star$),[133] and T_C of the superlattices are given in Table 5.5. The calculated Hopfield parameters(η) and the electron-phonon coupling constants (λ_t) per atom type are tabulated in Table 5.6 ($n = 1$), Table 5.7 ($n = 3$), Table 5.8 ($2/8$), Table 5.9 ($4/8$), and Table 5.10 ($4/12$). In the $n = 1$ case, all atoms are listed, whereas only the atoms with the largest contribution are listed for the other cases. The $n = 1$ (111) and $2/8$ (001) cases, have $\lambda = 0.411$ and 0.406, respectively, which result in T_C to be 2.09 K and 4.40 K, respectively. The higher T_C in the $2/8$ case is due to the lower value of $\mu^\star$. The other cases ($n = 3$, $4/8$, and $4/12$), have a T_C of 0.03 K, 0.45 K, and 0.06 K, respectively.

[0e] There are several choices of evaluating λ from the individual Hopfield parameters. For compounds, we follow the way suggested in Ref. [127].

	λ	$\mu^\star$	$T_C\ (K)$
$n=1$	0.411	0.09	2.09
$n=3$	0.155	0.02	0.03
$2/8$	0.406	0.05	4.40
$4/8$	0.253	0.04	0.45
$4/12$	0.210	0.05	0.06

Table 5.5: Calculated electron-phonon coupling constant (λ), Coulomb pseudopotential ($\mu^\star$), and T_C for [111] ($n=1$ and $n=3$) and [001] ($2/8$, $4/8$, and $4/12$) superlattices.

	Si[1]	Si[2]	Cu	Cl	Si[3]	Si[4]
$\eta\ (eV/\text{Å}^2)$	0.003	0.036	0.368	0.172	0079	0.007
λ	0.000	0.004	0.271	0.127	0.008	0.000

Table 5.6: Hopfield parameter(η) and the electron-phonon coupling constant (λ) in the $n=1$ superlattice. The total electron-phonon coupling constant, λ_{ep}, is 0.411.

	Si[6]	Cu[1]	Cl[3]	Si[7]
$\eta\ (eV/\text{Å}^2)$	0.048	0.064	0.128	0.042
λ	0.005	0.047	0.094	0.004

Table 5.7: Hopfield parameter(η) and the electron-phonon coupling constant (λ) in the $n=3$ superlattice of some interface atoms. The total electron-phonon coupling constant, λ_{ep}, is 0.155.

	Si[4]	Cu[1]	Cl[2]	Si[5]	Si[6]	Si[7]	Si[8]
$\eta\,(eV/\text{Å}^2)$	0.023	0.028	0.458	0.303	0.010	0.012	0.014
λ	0.002	0.020	0.338	0.033	0.001	0.001	0.001

Table 5.8: Hopfield parameter(η) and the electron-phonon coupling constant (λ) in the $2/8$ superlattice. The total electron-phonon coupling constant, λ_{ep}, is 0.406.

	Si[4]	Cu[1]	Cl[4]	Si[5]	Si[6]	Si[7]
$\eta\,(eV/\text{Å}^2)$	0.013	0.014	0.254	0.358	0.024	0.019
λ	0.001	0.010	0.187	0.039	0.003	0.002

Table 5.9: Hopfield parameter(η) and the electron-phonon coupling constant (λ) in the $4/8$ superlattice. The total electron-phonon coupling constant, λ_{ep}, is 0.253.

	Si[4]	Cu[1]	Cl[1]	Cl[4]	Si[5]	Si[6]	Si[7]
$\eta\,(eV/\text{Å}^2)$	0.019	0.037	0.020	0.161	0.206	0.015	0.016
λ	0.002	0.027	0.015	0.119	0.022	0.002	0.002

Table 5.10: Hopfield parameter(η) and the electron-phonon coupling constant (λ) in the $4/12$ superlattice. The total electron-phonon coupling constant, λ_{ep}, is 0.210.

In the $n = 1$ case, Cu has the largest value of λ and η. For the other cases, on the contrary, λ and η values are small for the interface Cu; the interface Cl atom has the largest value of λ. The interface Cl [$2/8$] and Si [$4/8$, $4/12$] of the Cl/Si interface have the largest η values. The fact that the interface Cl atom has the largest η value indicates superconductivity is indeed an interface effect in the electron-phonon mediation scheme. In the [111] superlattice, the larger λ value in the interface Cl than the interface Cu in the $n = 3$ case, while the opposite happens in the $n = 1$ case, implies that the addition of CuCl and Si layers changes the electron-phonon interaction. Furthermore, the large η and λ values of the interface Cl in the $n = 3$ case and the [001] superlattices, indicates that it is the Cl/Si interface which plays a more important role for superconductivity. The electron-phonon interaction matrix elements, $M_{l,l+1}$, change very little for a given atom type within a superlattice. The drastic changes of η values [see Eq. (5.1)] show that the fractional pDOS, f_l's, play the leading role in determining the Hopfield parameters. In particular, the different η values for the same atom kind within a superlattice, arise from the gain or loss of charge.

For the other cases, the lower T_C is due to the reduction of the η values, hence smaller values of λ. The DOS contribution of interface atoms, f_l in Eq. (5.1), gets smaller as the total number of layers increases since there are only two interfaces for any number of layers; therefore the fractional DOS, f_l, of interface atoms also diminishes as the number of layer increases. Finally, we note that the McMillan formula used for the T_C estimation is a numerical solution of the "isotropic" Eliashberg equation. However, the electron-phonon coupling in the CuCl/Si superlattices is highly anisotropic; thus, T_C might be higher if anisotropy of the electron-phonon coupling is rigorously taken into account in the T_C estimation.

Regarding experiment, we mentioned in Sec. 5.1, a nearly ideal diamagnetic signal believed to be due to superconductivity was observed between 60 and 150 K in CuCl over Si [111].[12] Thus if this system is superconducting as speculated by Mattes and Foiles, our investigation indicates that the electron-phonon interaction alone would not be able to account for it. In this sense, to study superconductivity further on these superlattices, the electronic (or excitonic) mechanism needs to be pursued.

5.4 ZnS/Si and GaP/Si superlattices

In previous sections, the electronic structure of CuCl/Si superlattice exhibited the 2D interface metallicity and possible superconductivity. One natural question is how other semiconductor superlattices would do. To answer this question, ZnS and GaP were explored. These have similar lattice constants to Si and CuCl. On the other hand, while CuCl is a strongly ionic compound [I-VII], ZnS and GaP are II-VI and III-V semiconductors, respectively, which would have different polarity at the interface from CuCl and Si.

ZnS and GaP crystallize in the zinc-blende structure with lattice constants, 5.40Å and 5.45Å, respectively. We consider the [111] growth direction, and superlattices A_n/Si_{4n} (A=GaP, ZnS) with $n = 2, 3$ layer, of which schematic model is sketched in Fig. 5.1, replacing Cu and Cl with Zn/Ga and S/P, respectively. Full structural optimization, *i.e.* of the volume and internal coordinates was done using FLAPW with the local density approximation (LDA) for the exchange-correlation potential as parametrized by Lundqvist and Hedin.[3] We used muffin-tin (MT) radii of 2.15 a.u. (Zn/Ga) and 2.00 a.u. (S/P, and Si), and spherical harmonics with $\ell \leq 8$ inside the MT spheres. The cut-off energy of plane

wave basis is 6.48 htr and that of the potential representation is 103.68 htr. The improved tetrahedron method[23] is used for k point summations with 119 points in the irreducible wedge of the Brillouin zone. The optimized lattice constants for all cases are tabulated in Table 5.11, where the numbers in parentheses are the relative change (in %) to those of the bulk zinc-blende structure.

5.4.1 Results for ZnS/Si and GaP/Si superlattices

Structure and Layer-Layer distances

First, the optimized lattice constants, a and c/a ratios of the superlattices are shown in Table 5.11. The lattice constants are converted to those of the conventional zinc-blende structure for better comparison. The c/a ratio without relaxation would be $\sqrt{6} \times n$ for n layers of ZnS or GaP. The numbers in parentheses are percentage changes with respect to non-relaxed structures. In general, the changes in a and c/a are small. However, note that the changes in ZnS are bigger than those in GaP. Second, comparisons of the layer-by-layer distances (in %) before and after relaxation are summarized for ZnS/Si and GaP/Si in Tables 5.12 and 5.13, respectively. Percentage changes of less than 4% are not listed, except for Ga[3]-P[3] in the $n = 3$ of GaP/Si superlattice. In the $n = 2$ superlattices, both ZnS/Si and GaP/Si exhibit large changes in layer distance at the interfaces, which implies that cation-Si move apart while anion-Si move closer. Moreover, cation-anion distances in ZnS or GaP region reduce a lot. In the $n = 3$, a similar trends are observed in layer-by-layer distances but the changes in ZnS/Si superlattice is much larger than those in GaP/Si.

Two dimensional interface metallicity

Two dimensional (2D) metallicity is found in all superlattices. Plots of their band structure

superlattice	n=2		n=3	
	a (Å)	c/a	a (Å)	c/a
GaP/Si	5.41 (-0.03)	4.89 (-0.17)	5.40 (-0.11)	7.35 (-0.02)
ZnS/Si	5.40 (0.13)	4.79 (-2.28)	5.40 (-1.37)	7.30 (-0.73)

Table 5.11: Optimized lattice constant, a, and c/a ratio. The lattice constants are converted to those of zinc-blende. The numbers in parentheses are the relative change (in%) of a and c/a with respect to those of zinc-blende structure without relaxation.

$n=2$		$n=3$	
Layer	change(%)	Layer	change(%)
Si[5]-S[2]	-26.97	Si[7]-S[3]	-28.75
Zn[2]-S[1]	-25.06	Zn[3]-S[2]	-17.15
Zn[1]-Si[4]	10.28	Zn[2]-S[1]	-14.26
		Zn[1]-Si[6]	20.41

Table 5.12: Percentage change in layer distances before and after relaxation for the ZnS/Si superlattices. The changes less than 4% are not listed here.

and Fermi surfaces are shown in Figs. 5.12 and 5.13 for the ZnS/Si and GaP/Si superlattices, respectively.

The character of the electron band is mostly anion(*sp*)-Si(*p*), while that of the hole band is cation(*d*)-Si(*p*). The dispersion of their bands look quite similar at first glance, but there are some noticeable differences. In the ZnS/Si case, both electron and hole bands have a dip along $M-K$ which is not present in the GaP/Si case. The valley of the hole band in the ZnS/Si superlattice along $K-\Gamma$ is in the vicinity of E_F, whereas those of GaP/Si seen along $K-\Gamma$ and $\Gamma-M$, are well above E_F. This difference introduces six small hole pockets between Γ and K in the Fermi surface in the ZnS/Si superlattice, which is not present in the GaP/Si superlattices. In the GaP/Si case, there are valleys in both electron and hole bands between L and A, which are not seen in the ZnS/Si case. These valleys in the GaP/Si superlattices cross E_F for the $n=3$ case, which introduces extra hole pockets around the Γ point in the Fermi surface plot, while in the $n=2$ case these valleys do not cross E_F. Another difference is that in the ZnS/Si case, the electron band does not cut the $\Gamma-M$ line. In other words, it is above E_F along the $M-L$ line, whereas in the GaP/Si case it cuts the $\Gamma-M$ line and is well below E_F along the $M-L$ line. This difference results in a different number of electronic sheets in the Fermi surface. The electron pockets (in blue) are of the two sheets with six-fold symmetry in the ZnS/Si superlattice, while in the GaP/Si superlattice they are of the single sheet around M. Above all, the 2D character is clearly displayed in the shape of the Fermi surfaces. This is evidenced more strongly in the charge density plots. The charge density in the vicinity of E_F, within 0.075 eV is shown in Figs. 5.14 and 5.15 for the ZnS/Si and GaP/Si superlattices, respectively, for the (a) $n=2$ and (b) $n=3$ cases; high concentrations of charges are at the interfaces. The

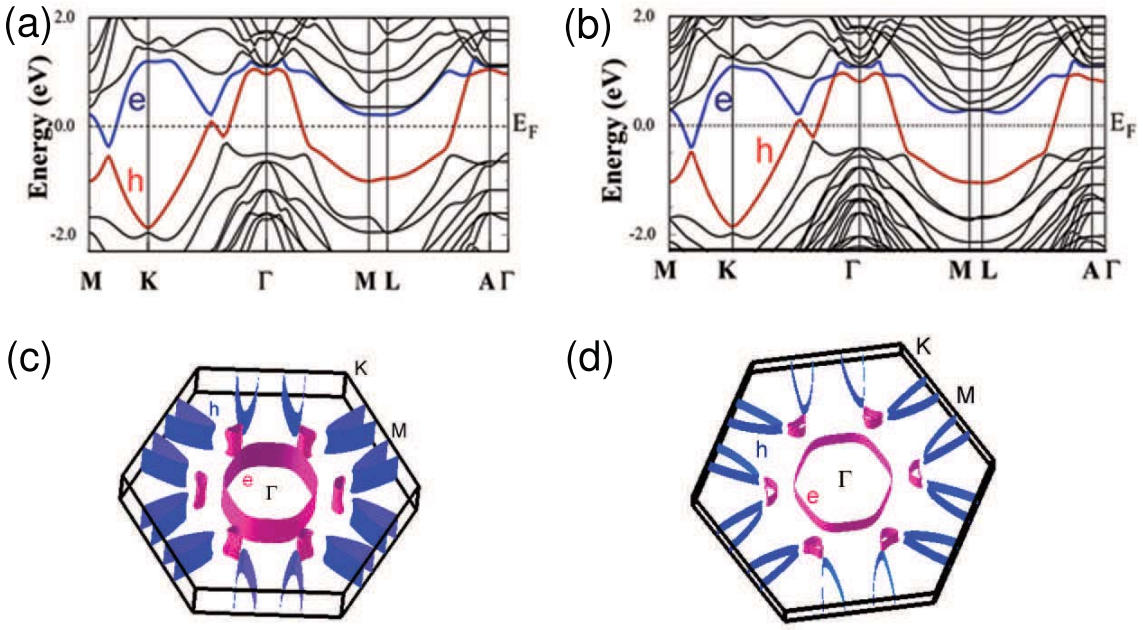

Figure 5.12: ZnS/Si superlattices: band structure of (a) $n = 2$, (b) $n = 3$ and corresponding Fermi surface plots of (c) $n = 2$ and (d) $n = 3$, respectively. Label h (e) indicates hole (electron) band for each case. High symmetry points, Γ, M, and K are shown in the Fermi surface plots.

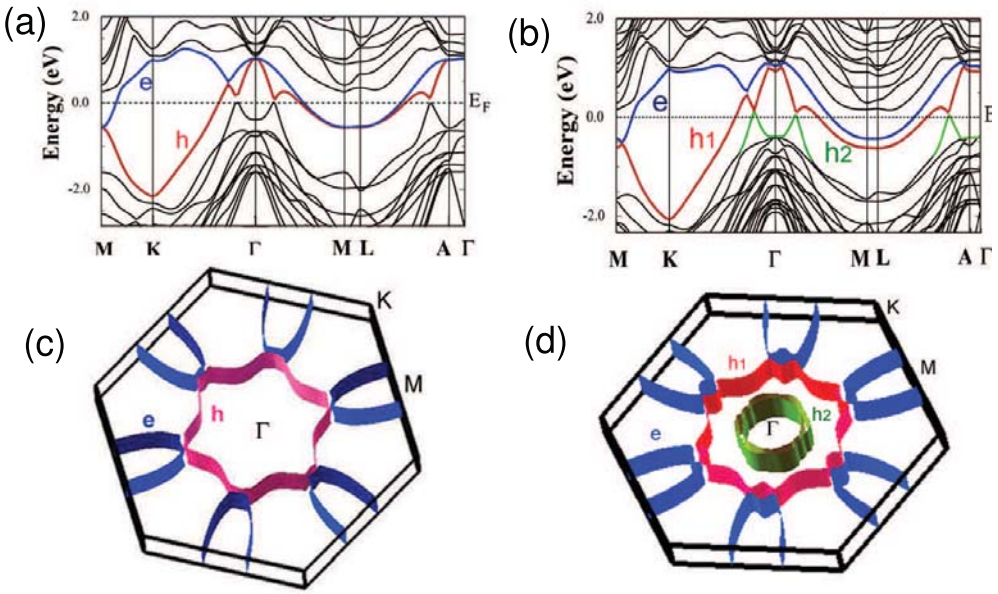

Figure 5.13: GaP/Si superlattices: band structure of (a) $n = 2$, (b) $n = 3$ and corresponding Fermi surface plots of (c) $n = 2$ and (d) $n = 3$, respectively. Label h (e) indicates hole (electron) band for each case. High symmetry points, Γ, M, and K are shown in the Fermi surface plots.

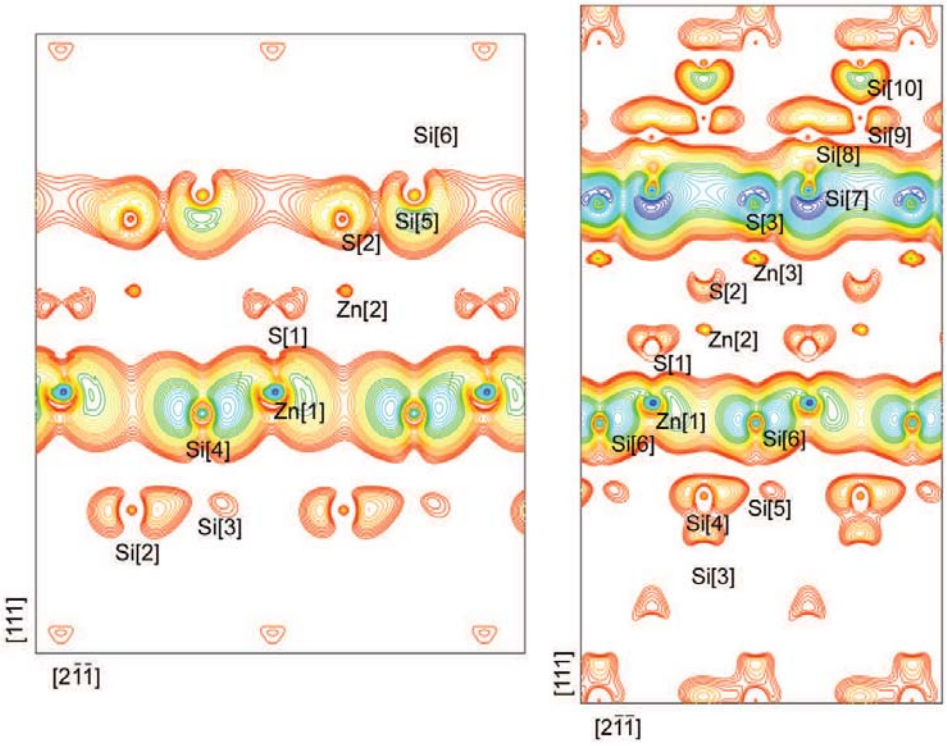

Figure 5.14: Charge density contour plots of (a) $n = 2$ and (b) $n = 3$ ZnS/Si superlattices around E_F within an energy slice of 0.075 eV. The starting density is $5.0 \times 10^{-4} e/\mathrm{Bohr}^3$ and subsequent lines increase by a factor of 1.15.

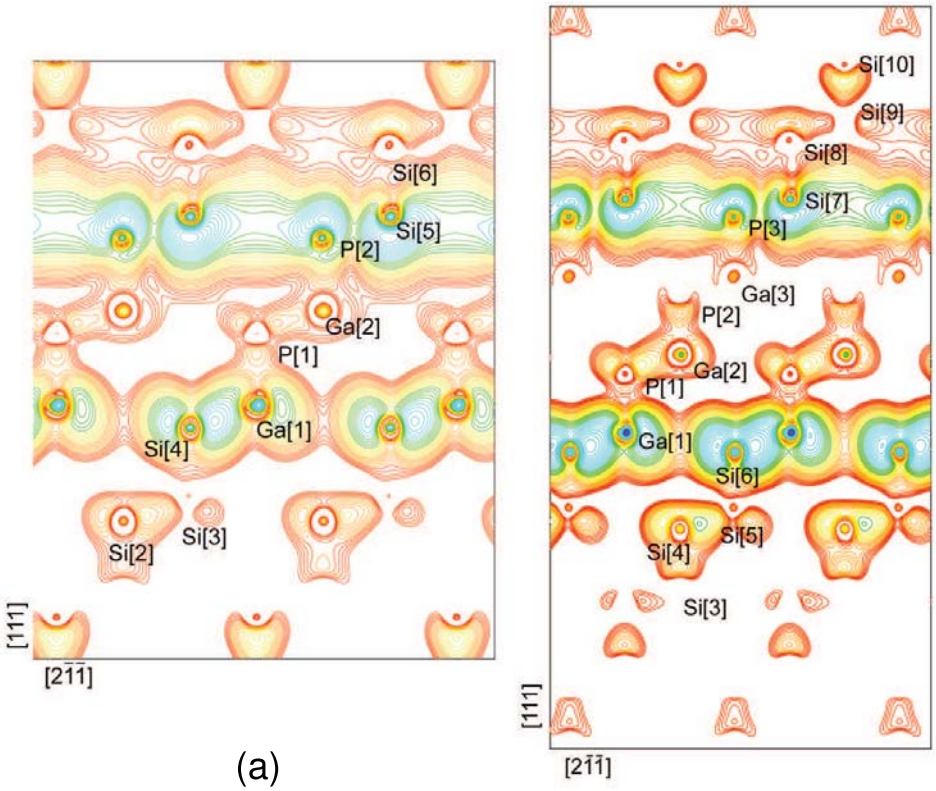

Figure 5.15: Charge density contour plots of (a) $n = 2$ and (b) $n = 3$ GaP/Si superlattices around E_F within an energy slice of 0.075 eV. The starting density is $1.0 \times 10^{-3} e/\mathrm{Bohr}^3$ and subsequent lines increase by a factor of 1.15.

charges in the GaP/Si are more spread out in the *c* direction from the interfaces than in ZnS/Si. However, the charge density plots in both cases exhibit qualitatively the similar trends, i.e. the interfaces can be thought as a metallic slab sandwiched by dielectric layers (the ZnS or GaP region).

Interface Charge

For the quantitative analysis of the interface charge, relative changes (in %) of the MT charge with respect to their bulk counterpart are listed in Tables 5.14 and 5.15 for the ZnS/Si and GaP/Si superlattices, respectively. The interface Si atoms lose charge while the interface Zn/Ga and S/P atoms gain charge. What is interesting is that the interface cation atoms (Zn,Ga) lose *d* charge but gain *s,p* charge, whereas the interface Si atoms gain *s* charge but lose *p* charge. The changes in the ZnS/Si superlattices are generally larger than in the GaP/Si superlattices. If one assumes the two-electron-per-bond counting rule, as depicted in Fig. 5.11, the Si-Zn (Si-Ga) bond lacks 2/4(1/4) electron per bond, while the Si-S (Si-P) bond has an excess of 2/4(1/4) electrons. This simple counting rule again explains the *p*-type character of the Si-Zn (Si-Ga) interfaces and the *n*-type character of the Si-S (Si-P) interfaces. The larger charge imbalance in the ZnS/Si superlattices compared to the GaP/Si, due to the larger polarity mismatch with Si atoms, yields larger changes in the MT charge as well as stronger confinement of the conducting electrons at the interfaces.

Superconductivity

As in the case of the CuCl/Si superlattices, to explore superconductivity, first the McMillan-Hopfield[85,20] electron-phonon coupling constant, λ_{ep}, is estimated within the crude rigid muffin-tin approximation (RMTA). The average phonon frequency is estimated by $\langle\omega^2\rangle^{1/2} = 0.69\langle\Theta_D\rangle$, where Θ_D is the weighted-average of Θ_D for Si and ZnS (GaP). The experi-

$n=2$		$n=3$	
Layer	change(%)	Layer	change(%)
Si[5]-P[2]	-26.89	Si[7]-P[3]	-5.85
Ga[2]-P[1]	-24.98	Ga[3]-P[3]	2.02
Ga[1]-Si[4]	10.40	P[2]-Ga[3]	4.91
		Ga[1]-Si[6]	5.36

Table 5.13: Percentage change in layer distances before and after relaxation for the GaP/Si superlattice. The changes less than 4% are not listed here.

$n=2$	*s*	*p*	*d*	$n=3$	*s*	*p*	*d*
Si[4]	7.83	-9.51		Si[6]	8.18	-11.81	
Zn[1]	28.51	16.93	-0.66	Zn[1]	26.25	11.76	-0.63
S[2]	4.33	-2.93		S[3]	4.46	-2.88	
Si[5]	11.62	-17.38		Si[7]	11.95	-17.68	

Table 5.14: Relative change (in%) of the orbital resolved MT charge of the interface atoms in ZnS/Si superlattices with respect to bulk Si and ZnS.

$n=2$	*s*	*p*	*d*	$n=3$	*s*	*p*	*d*
Si[4]	4.55	-2.13		Si[6]	4.75	-2.82	
Ga[1]	7.56	8.38	-0.18	Ga[1]	7.34	7.93	-0.18
P[2]	2.04	-3.51		P[3]	2.14	-3.46	
Si[5]	3.27	-11.28		Si[7]	3.39	-11.02	

Table 5.15: Relative change (in%) of the orbital resolved MT charge of the interface atoms in the GaP/Si superlattices with respect to bulk Si and GaP.

	ZnS/Si		GaP/Si	
	$n=2$	$n=3$	$n=2$	$n=3$
λ	0.075	0.098	0.043	0.042
$\mu^\star$	0.04	0.028	0.029	0.023
T_C (K)	0.0	10^{-5}	0.0	0.0

Table 5.16: Calculated electron-phonon coupling constant (λ), Coulomb pseudopotential ($\mu^\star$), and T_C for ZnS/Si and GaP/Si superlattices.

mental Debye temperatures taken for the calculation are 625 K,[54] 440K, [Ref.[134]] and 445 K [Ref.[135]] for Si, ZnS, and GaP, respectively. The estimated electron-phonon coupling constants λ and Coulomb pseudopotentials $\mu^\star$ are given in Table 5.16. T_C is again evaluated using Eq. (5.5).[20] The strongest electron-phonon coupling is present at the interfaces. However, as seen in Table 5.16 resulting T_C's are less than 10^{-5} K.[f] Acknowledging the crudeness of RMTA, definite conclusion cannot be drawn.

5.5 Conclusion

In this chapter, a study of superlattices of hetero-bonded semiconductor is presented. All superlattices clearly exhibit 2D metallicity at the interfaces, as shown by the band structures, Fermi surfaces, and charge density plots. All superlattices show the largest electron-phonon coupling at the interfaces. The CuCl/Si superlattices, in particular, show a possible superconductivity within the BCS electron-phonon mediated scheme with T_C between 0.4 and 6 K. In the case of the ZnS/Si and GaP/Si superlattices, it is hard to conclude there is superconductivity. Although ZnS/Si and GaP/Si also exhibit 2D metallicity and a largest electron-phonon at the interfaces, the electron-phonon coupling is not strong enough to cause a pairing, which make CuCl/Si more special.

[0f] $T_C = 10^{-5}$K is for the n=3 of ZnS/Si case. T_C of others is much less than 10^{-13} K.

Chapter 6: Excitonic (electronic) mechanism of superconductivity

6.1 Introduction

In this chapter, the excitonic (*or* electronic) mechanism of superconductivity is discussed. In order to understand effective pairing in the excitonic mechanism, we discuss the dielectric function and its inverse, and the kernel function formalism is reviewed. As discussed in Chapter 4, it is essential to investigate the fully screened *effective* interaction between electrons to explore the excitonic (*or* electronic) mechanism of superconductivity in more detail. This screening is primarily expressed by the inverse dielectric function (IDF) or dielectric function. Throughout this thesis, the contribution of the lattice degrees of freedom (phonons) are completely excluded; thus the screening considered here is *purely* electronic and its resulting pairing, if any, would also be electronic. Formally, the *effective* interaction is written as

$$\begin{aligned} V^{scr} &= V_{eff}(\mathbf{q}+\mathbf{G},\omega) \\ &= V_C(\mathbf{q}+\mathbf{G}')\cdot\varepsilon^{-1}_{\mathbf{G},\mathbf{G}'}(\mathbf{q},\omega), \end{aligned} \tag{6.1}$$

where $V_C(q) = 4\pi e^2/q^2$ is the bare Coulomb interaction, and $\varepsilon^{-1}_{\mathbf{G},\mathbf{G}'}(\mathbf{q},\omega)$ is the inverse dielectric function. To have an attractive interaction, it is necessary to have a negative value of $\varepsilon^{-1}_{\mathbf{G},\mathbf{G}'}(\mathbf{q},\omega)$ for a certain range of energies (frequencies). While it is often assumed that a negative value of the dielectric function (DF) would violate the stability requirement of the system, since it has been long believed that the DF satisfies (*or* should satisfy) the causality requirement, i.e. the Kramers-Kronig relation, which states that $\varepsilon(\omega)$ must be greater than unity for any frequency, Kirzhnits,[136] in his seminal paper, showed that it is the inverse dielectric function, not the ordinary dielectric function, which should satisfy the causality requirement. This is quite opposite to the generally understood intuition. The rest of this section illustrates two points: (i) the IDF indeed satisfies the causality requirement and is the proper response function for all cases; (ii) the DF can have negative values without violating the stability condition. To discuss the two above mentioned features, we borrow an important physics argument from Kirzhnits.[136]

In the linear response scheme, a response function describes the reaction (response) of the system to an external perturbation, i.e.

$$(\text{result of perturbation}) = (\text{response function}) \times (\text{external perturbation}). \tag{6.2}$$

This relationship has a definite causal character: "cause always precedes effect in time". For the dielectric functions, the external perturbation is usually an external charge ρ_{ext}, and its effect is an induced charge ρ_{ind} or total charge ρ_{tot}. Formally,

$$\nabla \cdot \mathbf{D} = 4\pi\, \rho_{\text{ext}}\ , \tag{6.3}$$

$$\nabla \cdot \mathbf{E} = 4\pi\, \rho_{\text{ind}}\ . \tag{6.4}$$

The momentum and frequency space representation of Eq. (6.3) and Eq. (6.4) are

$$\mathbf{D}(\mathbf{q},\omega) = \varepsilon(\mathbf{q},\omega)\mathbf{E}(\mathbf{q},\omega), \tag{6.5}$$

$$\rho_{\rm ext}(\mathbf{q},\omega) = \varepsilon(\mathbf{q},\omega)\rho_{\rm ind}\ . \tag{6.6}$$

If we take $\rho_{\rm ind}$ as a result of an external perturbation, then

$$\rho_{\rm ind} = \frac{1}{\varepsilon(\mathbf{q},\omega)}\rho_{\rm ext}\ \ , \tag{6.7}$$

which implies that the IDF, $1/\varepsilon$, is the true response function. At first glance, the DF and the IDF in Eq. (6.6) and Eq. 6.7, seem to be response functions. However, if the DF in Eq. (6.6) is the response function, then the induced charge is the perturbation and the external charge is the result of it. Using a capacitor argument, Kirzhnits pointed out that the precise concept of the external charges is by definition the charges that do not appear in the composition of the system. For the general variation of $q \neq 0$, it is necessary to fix the external source, otherwise one cannot distinguish the induced and external source of the system. If this external charge is in the system with $q \sim L^1 \rightarrow 0$, where L is the macroscopic size of the system, one can associate it with the long wavelength limit of the dielectric function.

By contrast, the IDF is the response function in any case since the external charge is a well-defined perturbation. Kirzhnits showed that the DF is only a proper response function in the long wavelength limit. Thus, for general spatial variations of $\mathbf{q}$, the IDF $[1/\varepsilon(\mathbf{q},\omega)]$ is the response function of the system, whereas the ordinary dielectric function $[\varepsilon(\omega)]$ can be a response function only in the long wavelength limit, i.e. $q \rightarrow 0$. Asserting the above arguments, the IDF always obeys causality, and therefore the Kramers-Kronig

relation applies:

$$\frac{1}{\varepsilon(\mathbf{q},\omega)} = 1 + \frac{1}{\pi}\int_0^\infty d\omega'^2 \, \frac{\mathrm{Im}\; 1/\varepsilon(\mathbf{q},\omega')}{\omega'^2 - \omega^2 - i\eta} \;\; . \tag{6.8}$$

Additionally, the fact that the DF is a response function in the long wavelength limit implies that it also satisfies causality:

$$\varepsilon(q=0,\omega) = 1 + \frac{1}{\pi}\int_0^\infty d\omega'^2 \, \frac{\mathrm{Im}\; \varepsilon(q=0,\omega')}{\omega'^2 - \omega^2 - i\eta} \;\; . \tag{6.9}$$

One fundamental property of the IDF is that it can be related to the form factor for the inelastic scattering of electrons,

$$\mathrm{Im}\left[\frac{1}{\varepsilon(\mathbf{q},\omega)}\right] = -\frac{4\pi^2 e^2}{q^2}\, F(\mathbf{q},\omega) \;\; , \tag{6.10}$$

where $F(\mathbf{q},\omega) > 0$ is the form factor, which characterizes the probability of electron energy loss with respect to the frequency, ω, and momentum,$\mathbf{q}$. If $\mathrm{Im}\; 1/\varepsilon < 0$, and $\mathrm{Im}\; \varepsilon > 0$, Eq. (6.8) gives the inequalities

$$\varepsilon(\mathbf{q},\omega) > 1, \qquad \varepsilon(\mathbf{q},\omega) < 0. \tag{6.11}$$

Eq. (6.11) holds for the static case [$\omega = 0$], allowing a negative value of the dielectric function, and resulting in an attractive interaction between electrons. For general $\mathbf{q}$ vectors, Eq. (6.10) implies that the inverse dielectric function, $\varepsilon^{-1}(\mathbf{q},\omega)$ is of more fundamental importance since it is directly related to an experimentally measurable quantity.

6.2 Dielectric function

The dielectric function in the RPA scheme is found by rewriting Eq.(3.1) in Chapter 3:

$$\varepsilon_{\mathbf{G},\mathbf{G}'}(\mathbf{q},\omega) = \delta_{\mathbf{G},\mathbf{G}'} - \mathrm{V}(\mathbf{q}+\mathbf{G})\chi^0_{\mathbf{G},\mathbf{G}'}(\mathbf{q},\omega), \tag{6.12}$$

where $\mathrm{V}(\mathbf{q}+\mathbf{G}) = 4\pi e^2/|\mathbf{q}+\mathbf{G}|^2$ is already diagonal in $\mathbf{G}$ space and χ^0 is the polarization function, or susceptibility (superscript 0 will be dropped hereafter). To obtain the screened Coulomb interaction, the inverse dielectric function, $\varepsilon^{-1}_{\mathbf{G},\mathbf{G}'}(\mathbf{q},\omega)$, is needed. Without local field effects, inverting ε_{00} to get ε^{-1}_{00} is calculated using a simple numerical inversion. However, when local field effects are included, the inversion of the dielectric function for limited number of $\mathbf{G}$ vectors will result in a huge truncation error. Therefore, it is more effective numerically to work directly on the inverse dielectric function.[137] For the inverse dielectric function, $\varepsilon^{-1}_{\mathbf{G},\mathbf{G}'}(\mathbf{q},\omega)$, the expression is given by Adler:[138]

$$\varepsilon^{-1}_{\mathbf{G},\mathbf{G}'}(\mathbf{q},\omega) = \delta_{\mathbf{G},\mathbf{G}'} + \sum_{\mathbf{G}_2} \mathrm{V}(\mathbf{q}+\mathbf{G}_2)\chi_{\mathbf{G},\mathbf{G}_2}\varepsilon^{-1}_{\mathbf{G}_2,\mathbf{G}'}(\mathbf{q},\omega), \tag{6.13}$$

where $\chi_{\mathbf{G},\mathbf{G}'}(\mathbf{q},\omega)$ is the electronic susceptibility given by

$$\begin{aligned} \chi_{\mathbf{G},\mathbf{G}'}(\mathbf{q},\omega) &= \sum_{\mathbf{k},m,n} \frac{f(E_{\mathbf{k}+\mathbf{q},m}) - f(E_{\mathbf{k},n})}{E_{\mathbf{k}+\mathbf{q},m} - E_{\mathbf{k},n} - \omega - i\eta} \\ &\times \langle \mathbf{k}+\mathbf{q}, m\,|e^{i(\mathbf{q}+\mathbf{G})\cdot\mathbf{r}}|\,\mathbf{k}, n\rangle\langle \mathbf{k}, n\,|e^{-i(\mathbf{q}+\mathbf{G}')\cdot\mathbf{r}'}|\,\mathbf{k}+\mathbf{q}, m\rangle\ . \end{aligned} \tag{6.14}$$

$f(E_{\mathbf{k}+\mathbf{q},m})$ is the Fermi-Dirac distribution function of a particular $\mathbf{k}$ point and band index n. Eq. (6.13) is a summation of infinite terms; rewriting the summation up to second-order of the Coulomb interaction V_C, it becomes

$$\begin{aligned} \varepsilon^{-1}_{\mathbf{G},\mathbf{G}'}(\mathbf{q},\omega) = \delta_{\mathbf{G},\mathbf{G}'} &+ \mathrm{V_C}(\mathbf{q}+\mathbf{G}')\chi_{\mathbf{G},\mathbf{G}'}(\mathbf{q},\omega) \\ &+ \sum_{\mathbf{G}_2} \mathrm{V_C}(\mathbf{q}+\mathbf{G}_2)\chi_{\mathbf{G},\mathbf{G}_2}\mathrm{V_C}(\mathbf{q}+\mathbf{G}')\chi_{\mathbf{G}_2,\mathbf{G}'}(\mathbf{q},\omega) \\ &+ O(\mathrm{V_C}^3), \end{aligned} \tag{6.15}$$

Although it is highly desirable to work on the local-field effects as well as in terms of higher-order of V_C in Eq. (6.15), in this thesis local-field effects are ignored. Instead of

working on the inverse dielectric function directly following in Eq. (6.13), the dielectric function is numerically inverted to obtain its inverse because the dielectric function is more easily calculated. Another reason to work on the dielectric function first is that it has not been systematically studied how many terms of V_C are required in Eq. (6.15) to obtain the inverse dielectric function . which satisfies $\varepsilon^{-1}(\mathbf{q},\omega)\cdot\varepsilon(\mathbf{q},\omega)=1$

6.3 Effective screened potential

In BCS theory, an attractive interaction is already assumed in the pairing potential, which is denoted by $V_{\mathbf{k},\mathbf{k}'} = -V$ ($V > 0$) as depicted in Fig. 4.2 (a). In a practical *ab initio* approach, however, it is essential to evaluate the *effective* interaction between electrons without invoking any *a priori*. The first formulation of the screened interaction was suggested by Zakharov *et al.*[92] Here is a reformulation of their formulation of the pairing potential and the kernel function for the the LAPW basis.

Suppose two Bloch electrons of states $|\mathbf{k},n\rangle$ and $|-\mathbf{k},m\rangle$ form a Cooper pair and scatter off another Cooper pair of states $|\mathbf{k}',n'\rangle$ and $|-\mathbf{k}',m'\rangle$. In the presence of screening, the *effective* interaction between electrons,

$$V^s(\mathbf{q},\omega) = V_C\cdot\frac{1}{\varepsilon(\mathbf{q},\omega)} = \frac{4\pi e^2}{\Omega|\mathbf{q}+\mathbf{G}|^2}\frac{1}{\varepsilon(\mathbf{q},\omega)}. \tag{6.16}$$

In a real space representation, the screened Coulomb interaction becomes

$$V^s(\mathbf{r},\mathbf{r}') = \frac{4\pi e^2}{\Omega}\sum_{\mathbf{G},\mathbf{G}'} e^{i(\mathbf{q}+\mathbf{G})\cdot\mathbf{r}}\frac{\varepsilon^{-1}_{\mathbf{G},\mathbf{G}'}(\mathbf{q},\omega)}{|\mathbf{q}+\mathbf{G}|^2}e^{-i(\mathbf{q}+\mathbf{G}')\cdot\mathbf{r}'}. \tag{6.17}$$

The pairing potential in the presence of a screened interaction is

$$V^p_{\mathbf{k},\mathbf{k}'} = \langle\mathbf{k}',-\mathbf{k}',\varepsilon'|V^s(\mathbf{r},\mathbf{r}')|\mathbf{k},-\mathbf{k},\varepsilon\rangle \tag{6.18}$$

$$
\begin{aligned}
&= \frac{4\pi e^2}{\Omega} \sum_{\mathbf{G},\mathbf{G}'} \langle \mathbf{k}', -\mathbf{k}', \varepsilon' | e^{i(\mathbf{q}+\mathbf{G})\cdot\mathbf{r}} \frac{\varepsilon^{-1}_{\mathbf{G},\mathbf{G}'}(\mathbf{q},\omega)}{|\mathbf{q}+\mathbf{G}|^2} e^{-i(\mathbf{q}+\mathbf{G}')\cdot\mathbf{r}'} | \mathbf{k}, -\mathbf{k}, \varepsilon \rangle \\
&= \frac{4\pi e^2}{\Omega} \sum_{\mathbf{G},\mathbf{G}'} \langle \mathbf{k}', \varepsilon' | e^{i(\mathbf{q}+\mathbf{G})\cdot\mathbf{r}} | \mathbf{k}, \varepsilon \rangle \frac{\varepsilon^{-1}_{\mathbf{G},\mathbf{G}'}(\mathbf{q},\omega)}{|\mathbf{q}+\mathbf{G}|^2} \langle -\mathbf{k}', \varepsilon' | e^{-i(\mathbf{q}+\mathbf{G}')\cdot\mathbf{r}'} | -\mathbf{k}, \varepsilon \rangle \\
&= \frac{4\pi e^2}{\Omega} \sum_{\mathbf{G},\mathbf{G}'} P(\mathbf{k},\mathbf{q},\mathbf{G}) \cdot \frac{\varepsilon^{-1}_{\mathbf{G},\mathbf{G}'}(\mathbf{q},\omega)}{|\mathbf{q}+\mathbf{G}|^2} \cdot P^*(\mathbf{k},\mathbf{q},\mathbf{G}'),
\end{aligned}
$$

where ε and ε' are the initial and final energies of the Bloch states, respectively, and the band summation is suppressed. Eq. (6.18) is simply the scattering amplitude of a Cooper pair from states $|\mathbf{k},\varepsilon\rangle$ and $|-\mathbf{k},\varepsilon\rangle$ to $|\mathbf{k}',\varepsilon'\rangle$ and $|-\mathbf{k}',\varepsilon'\rangle$. Assuming the spatial variables $\mathbf{r}$ and $\mathbf{r}'$ are separable, then $P(\mathbf{k},\mathbf{q},\mathbf{G}) = \langle \mathbf{k}', \varepsilon' | e^{i(\mathbf{q}+\mathbf{G})\cdot\mathbf{r}} | \mathbf{k}, \varepsilon \rangle$, and $\mathbf{k}' = \mathbf{k} + \mathbf{q}$ from momentum conservation.[a] [1] Invoking time-reversal symmetry, $\Psi_{-\mathbf{k}}(\mathbf{r}) = \Psi^*_{\mathbf{k}}(\mathbf{r})$, it is easy to show that

$$
\begin{aligned}
P(-\mathbf{k},\mathbf{q},\mathbf{G}') &= \langle -\mathbf{k}', \varepsilon' | e^{i(\mathbf{q}+\mathbf{G})\cdot\mathbf{r}} | -\mathbf{k}, \varepsilon \rangle \\
&= \int d\mathbf{r}\ \Psi^*_{-\mathbf{k}'}(\mathbf{r}) e^{i(\mathbf{q}+\mathbf{G})\cdot\mathbf{r}} \Psi_{-\mathbf{k}}(\mathbf{r}) \\
&= \int d\mathbf{r}\ \Psi_{\mathbf{k}'}(\mathbf{r}) e^{i(\mathbf{q}+\mathbf{G})\cdot\mathbf{r}} \Psi^*_{\mathbf{k}}(\mathbf{r}) \\
&= P^*(\mathbf{k},\mathbf{q},\mathbf{G}').
\end{aligned}
\tag{6.19}
$$

In the long wavelength limit [$q \to 0$], $P(\mathbf{k},\mathbf{q},\mathbf{G})$ is simply the optical matrix as appeared in Eq. 3.2. Thus, in the excitonic (electronic) mechanism, the pairing potential already contains the nature of electronic excitation for general $\mathbf{q}$ values, and the energy transfer corresponds to the difference of energies, ε and ε', of the two Cooper pairs as in Eq. (6.18). One noteworthy point in the excitonic mechanism is that the energy transfer of the scattering of two Cooper pair would be of the order of the excitation gap (ω_g) or plasma frequency

[1] [a] $\mathbf{k}' = \mathbf{k} + \mathbf{q}$ is true if we ignore the translational symmetry of the crystal. In fact, it is $\mathbf{k}' = \mathbf{k} + \mathbf{q} + \mathbf{G}_o$, where $\mathbf{G}_o$ is reciprocal lattice vector. This relation is proved in Appendix A.

(ω_p) whereas in the phonon mediation, the energy transfer of Cooper pair scattering is restricted to the narrow shell of Fermi surface with the thickness of the Debye frequency, Ω_D. This picture is consistent with the ABB picture as explained in Chapter 4: electrons in the metallic region penetrate into the semiconductor gap region where they exchange virtual excitons whose momentum and energy correspond to those of the Cooper pair.

6.4 The kernel function, formalism and past work

One distinct feature of superconductivity is the presence of the superconducting gap, Δ, the energy required to excite a Cooper pair. The gap vanishes with the disappearance of superconductivity and has its maximum value at zero temperature. The BCS gap equation is a central part to BCS theory, as in Eq. 4.1. We rewrite the self-consistent gap equation (Eq. 4.1),

$$\Delta_{\mathbf{k}} = -\underbrace{\sum_{\mathbf{k}'} V_{\mathbf{k},\mathbf{k}'}}_{\text{kernel part}} \underbrace{\frac{\Delta_{\mathbf{k}'}}{2E_{\mathbf{k}'}} \tanh(\frac{\beta E_{\mathbf{k}'}}{2})}_{\text{gap dependent part}}, \tag{6.20}$$

where $E_{\mathbf{k}}^2 = \xi_{\mathbf{k}}^2 + \Delta_{\mathbf{k}}^2$, and $\xi(\mathbf{k}) = \varepsilon(\mathbf{k}) - E_F$. The pairing potential is approximated by $V_{\mathbf{k},\mathbf{k}'} = -V, \ \ (V > 0)$ and after the summation over $\mathbf{k}$ for both sides, we obtain Eq. 4.3 in Chapter 4. As clearly illustrated in Eq. (6.20), the BCS gap equation is comprised of a gap dependent and a gap independent part. The gap-independent part of this equation involves the summation of the potential, a measure of the attractive interaction between electrons. Cohen,[64] while proposing possible superconductivity in many-valley semiconductors, first examined this gap-independent potential part. It was later renamed the kernel function of superconductivity. In Cohen's first derivation, the *k* summation in Eq. (6.20) was converted

to an integral:

$$\begin{aligned} \sum_{\mathbf{k}'} &\rightarrow \int d\xi_{\mathbf{k}'}\, N(\xi) \\ &= \int d\xi_{\mathbf{k}'}\, \frac{\sigma \cdot \Omega}{(2\pi)^3} \int \frac{d\mathbf{S}}{|\nabla \xi_{\mathbf{k}'}|}, \end{aligned} \tag{6.21}$$

where σ stands for the spin degeneracy (2 for the spin unpolarized case), Ω is the unit cell volume, and $d\mathbf{S}$ represents a surface integration over *k* space. Within the parabolic band approximation, $\nabla \xi_{\mathbf{k}'} = \hbar \mathbf{v}$, where $\mathbf{v}$ is the velocity of the electron in *k* space. Further, the surface integral can be converted to a $\mathbf{q}$ integration, noting that $\mathbf{k}' = \mathbf{k} + \mathbf{q}$,

$$\int d\mathbf{S} \rightarrow \int_{|k-k'|}^{k+k'} q dq \int_0^{2\pi} d\theta. \tag{6.22}$$

Thus, the gap-independent part of Eq. (6.20) becomes

$$K(k,\omega) = \frac{\sigma \Omega}{2(2\pi)^2} \frac{1}{\hbar v} \int_{|k-k'|}^{k+k'} q dq\, V_{\mathbf{k},\mathbf{k}'}, \tag{6.23}$$

where $\omega = \xi_{\mathbf{k}} - \xi_{\mathbf{k}'}$. The form of Eq. (6.23) was further expressed by scaling momentum k and energy ω for convenience. Nevertheless, Eq. 6.23 uses the parabolic band approximation, which is reliable for doped semiconductors in the vicinity of high symmetry points in Brillouin zone. Later, Ihm *et al.*,[139] investigated the possibility of acoustic demon pairing, using the following kernel function

$$K(\omega) = \left(\frac{4}{9\pi}\right)^{1/3} r_s \frac{k_F}{k'} \int_{|k-k'|}^{k+k'} \frac{dq}{q} Re\left[\frac{1}{\varepsilon(q,\omega)}\right]. \tag{6.24}$$

They evaluated this function for a model system, where heavy *d* and light *s* and *p* electrons in a transition metal were considered. The density of the system was parametrized by r_s, and a bare Coulomb interaction $V_C = 4\pi/q^2$ was employed. Ihm *et al.* showed that

the demon contribution generally reduces the Coulomb interaction, but is not dominant in transition metals and transition-metal compounds.

Ginzburg also used the kernel function,[140] when discussing the excitonic (electronic) mechanism. He considered two kinds of model dielectric functions,

$$\varepsilon(q,\omega) = \varepsilon_r(\omega) = 1 + \frac{\omega_r^2(\varepsilon_0 - 1)}{\omega_r^2 - \omega^2}, \tag{6.25}$$

$$\varepsilon(q,\omega) = 1 + \frac{K^2}{q^2} - \frac{\omega_i^2}{\omega^2}. \tag{6.26}$$

The first model function consists of non-interacting harmonic oscillators, $\omega_r^2(\varepsilon_0 - 1) = (4\pi e^2/m)n_r$ where n_r is the concentration of the oscillators. This model function is negative when the frequency falls in the range $\omega_r < \omega < \sqrt{\epsilon_0}\omega_r$, as is $V(q,\omega) < 0$. The second model is the "jellium" model including some structureless electronic-ionic plasma with damping neglected ($\omega \ll qv_F$), and where $\omega_i^2 = 4\pi e^2 Z^2 n_i/M$, the plasma frequency for the ions with density n_i and $K^2 = 6\pi e^2 n/E_F$ ($1/K$ is the screening radius). For the "jellium" model, the *effective* interaction is

$$V_{eff}(q,\omega) = \frac{4\pi e^2}{\varepsilon(q,\omega)q^2} = \frac{4\pi e^2}{q^2 + K^2}\Big(1 + \frac{\omega_q^2}{\omega^2 - \omega_q^2}\Big), \tag{6.27}$$

where ω_q is the frequency of the longitudinal waves which can propagate in a medium with dielectric function, Eq. (6.26) . It is already evident that an attractive interaction can exist even in this simple isotropic model. Ginzburg further extended it to a generalized "jellium" model

$$\varepsilon(q,\omega) = 1 + \frac{k^2}{q^2} - \frac{\omega_i^2}{\omega^2} + \frac{\Omega^2(\varepsilon_0 - 1)}{\Omega^2 - \omega^2}, \tag{6.28}$$

where the ionic contribution with Ω is included and $\Omega \gg \omega_i$ is assumed. By setting $\varepsilon(q,\omega) = 0$, two branches of eigen-frequencies are obtained; one is phonon-like and the

other exciton-like with longitudinal character. By evaluating the kernel function *or* the *effective* interaction, $V_{eff} = V_c/\varepsilon(q,\omega)$, he obtained

$$K(\omega) = \bar{V_c}\left[1 + \frac{\omega_i^2/\varepsilon_0^2}{\omega^2 - \omega_i^2/\varepsilon_0^2} + \frac{(\varepsilon_0 - 1)\Omega^2}{\omega^2 - \varepsilon_0\Omega}\right], \tag{6.29}$$

where $\bar{V_c}$ is the averaged value of the Coulomb interaction with respect to $\mathbf{q}$. He further investigated the pairing of the generalized "jellium" model in a more general aspect, following the analogous technique of the electron-phonon coupling scheme. The two quantum well model in Eliashberg theory is modified with a three-quantum-well state, for which the cutoff frequencies correspond to ω_{ph}, Ω_e, and ω_F, respectively ($\omega < \Omega_e < \Omega_F$). One remarkable achievement in the review by Ginzburg is that the possibility of an excitonic mechanism relies on obtaining the required exciton band; i.e. finding real material systems with the desired $\varepsilon(\mathbf{q},\omega)$.

In the mid 70's, Cohen and Louie (CL)[91] also used the kernel function in studying the metal-semiconductor interface: they explored the possibility of an excitonic mechanism proposed by ABB.[11] CL considered electron densities appropriate to Al and Si, roughly $r_s \sim 2$ and a static dielectric constant of $\varepsilon_0 \sim 10$. CL worked on the kernel function $K(\delta)$

$$K(\delta) \sim \int_{|\vec{k}-\vec{k'}|}^{|\vec{k}+\vec{k'}|} qV_t(q,\delta)dq, \tag{6.30}$$

$$V_t(\mathbf{q},\omega) = \frac{4\pi e^2}{q^2\varepsilon_s(\mathbf{q},\omega)}, \tag{6.31}$$

where V_t is the *screened total* interaction with dielectric function, $\varepsilon_s(\mathbf{q},\omega)$, and $\delta = \omega/E_F$. As mentioned in Section 4.4, CL considered three types of dielectric functions: first, the model by Inkson and Anderson (IA),

$$\varepsilon_s^{IA} = 1 + \frac{A}{1 + AB} \tag{6.32}$$

$$A = \varepsilon_0 - 1, \quad B = \frac{q^2}{K^2} - \frac{\omega^2}{\omega_p^2},$$

where K and ω_p are the inverse of the screening length and the plasmon energy of metal; second, the Lindhard dielectric function for a metal; and, third, the calculated $\varepsilon(\mathbf{q}, \omega)$ of Ge. CL found that the I-A dielectric function was attractive in a region of the frequency, but both the Lindhard and the Ge dielectric functions were repulsive for all frequencies. CL had focused on the metal-semiconductor model, not a real system, with approximate dielectric functions of different characters.

Later, a rigorous *ab initio* evaluation of the kernel function was performed by Zakharov *et al.* (ZK).[92] ZK calculated the electronic structure of a non-relaxed Si-jellium-Si superlattice, and the dynamic dielectric function with and without the local-field effect using a jellium density of $r_s = 2.07$. Their superlattice consists of 6 Si monolayers along the [001] direction and a jellium layer of two silicon bond lengths (2×2.45Å). Further, the kernel function $K(\omega)$ was calculated using the LDA wave functions and eigenvalues for 15 q points. The results by ZK show that the Si-jellium-Si system is metallic with a low DOS at E_F, showing some signs of charge transfer from jellium to the Si interface. For the kernel evaluation, ZK used the following expression

$$K(\varepsilon, \varepsilon') = N(\varepsilon_{\mathbf{k}}) \frac{\int\int d\mathbf{k}\, d\mathbf{k}'\, V_{\mathbf{k},\mathbf{k}'}\, \delta(\varepsilon - \varepsilon_{\mathbf{k}})\delta(\varepsilon' - \varepsilon_{\mathbf{k}'})}{\int d\mathbf{k} \int d\mathbf{k}'\, \delta(\varepsilon - \varepsilon_{\mathbf{k}})\delta(\varepsilon' - \varepsilon_{\mathbf{k}'})} \ , \tag{6.33}$$

where the pairing potential $V_{\mathbf{k},\mathbf{k}'}$ in a plane wave basis is given as

$$V^p_{\mathbf{k},\mathbf{k}'} = \frac{4\pi e^2}{\Omega} \sum_{\mathbf{q},\mathbf{G},\mathbf{G}'} Z^*_{\mathbf{G}} \frac{\varepsilon^{-1}_{\mathbf{G},\mathbf{G}'}(\mathbf{q}, \omega)}{|\mathbf{q} + \mathbf{G}|^2} Z_{\mathbf{G}'} \tag{6.34}$$

$$Z_{\mathbf{G}} = \sum_{\mathbf{G}_2} c^*_{\mathbf{G}_2 + \mathbf{G}}\, c_{\mathbf{G}_2} \ , \tag{6.35}$$

where $c_{\mathbf{G}}$ is a the Fourier expansion coefficient. Derivation of Eq. (6.34) and the relations among $\mathbf{k}$, $\mathbf{k}'$ and $\mathbf{q}$ are shown in Appendix A. Although the inverse dielectric function

showed a negative region in the frequency, the kernel function by ZK was repulsive for an entire frequency range. From a real materials perspective, it is suspicious that the Si-jellium-Si could be realized. In calculational sense, however, the reliability of calculations with a $\mathbf{k}$ point mesh of $(12 \times 12 \times 1)$ and 15 $\mathbf{q}$ points by ZK is questionable, noting that most dielectric function calculations incorporate a large number of $\mathbf{k}$ points. Nevertheless, ZK's work provided a good guideline on how to establish a screened interaction and pairing potential between electrons using a first-principles approach.

6.5 Kernel function of CuCl/Si superlattices

The result of CuCl/Si superlattices were given in Chapter 5, where the 2D interface metallicity and possible superconductivity was discussed in the electron-phonon mediation scheme using the RMTA method. In this section, we focus on the excitonic (electronic) pairing due to the electronic screening. We follow Zakharov *et al.*'s approach to evaluate the pairing potential and the kernel functions. First, the dielectric functions are calculated in the long wavelength limit, by *k* point summation in the irreducible wedge using 533 and 500 points for the [111] and [001] cases, respectively. Only interband transitions are taken into account. Further, plasma frequencies are obtained by applying the optical sum rule

$$\int_0^\infty d\omega \, \mathrm{Im}\, \varepsilon(\omega) = \frac{\pi}{2}\omega_{pl}^2. \tag{6.36}$$

The plasma frequencies indicate where the negative value of the pairing potential appears. The calculated plasma frequencies and static dielectric constants are summarized in Table 6.1.

For the pairing potential evaluations, 1625 *k* points in the full Brillouin zone ($19 \times$

Table 6.1: The plasma frequencies (in eV) and the static dielectric constants for the CuCl/Si superlattices. The plasma frequencies are the average of all three (xx, yy, zz) directions.

	ω_{av}^{pl}	ε_0^{xx}	ε_0^{yy}	ε_0^{zz}
$n=1$	11.02	22.32	22.97	12.97
$n=3$	14.04	16.87	16.55	13.51
2×8	23.18	85.48	82.10	49.52
4×8	21.00	120.98	135.19	79.60
4×12	20.81	68.72	71.08	80.19

19×9 mesh)are taken using the tetrahedron method. For the finite $\mathbf{q}$ values, $P(\mathbf{k}, \mathbf{q}, \mathbf{G})$ are no longer invariant under symmetry operations, *k* point summations should be in the full Brillouin zone.

The pairing potential of a particular $\mathbf{k}$ and $-\mathbf{k}$ is further summed up for a given $\mathbf{q}$ value, i.e.

$$\begin{aligned} V^p(\mathbf{q},\omega) &= \sum_{\mathbf{k}} V^p_{\mathbf{k},\mathbf{k}'} \\ &= \frac{4\pi e^2}{\Omega} \sum_{\mathbf{k},\mathbf{G},\mathbf{G}'} P(\mathbf{k},\mathbf{q},\mathbf{G}) \cdot \frac{\varepsilon^{-1}_{\mathbf{G},\mathbf{G}'}(\mathbf{q},\omega)}{|\mathbf{q}+\mathbf{G}|^2} \cdot P^*(\mathbf{k},\mathbf{q},\mathbf{G}')\delta(\varepsilon_{\mathbf{k}} - \varepsilon'_{\mathbf{k}'} - \hbar\omega) \ , \end{aligned} \tag{6.37}$$

where the *k* point summation is done using the tetrahedron method. For pairing potential evaluations, we chose two kinds of $\mathbf{q}$ point set: (i) 4 points along the high symmetry lines ($\Gamma - M$, $\Gamma - K$, $\Gamma - A$, and $\Gamma - L$) for a total of 16 points, (ii) $\mathbf{q}$ points which correspond to $4 \times 4 \times 2$ Monkhorst-Pack *k* points. First, the pairing potential $V_{\mathbf{k},\mathbf{k}'}(\mathbf{q},\omega)$ of the $n=1$ superlattice is shown in Fig. 6.1, where $\mathbf{q}$ is along the high symmetry lines: (a) $\Gamma - M$, (b) $\Gamma - K$, (c) $\Gamma - A$, (d) $\Gamma - L$. The curves in black, red, green, and blue correspond

to $\mathbf{q}$ points from Γ to point of high symmetry of interest. For most $\mathbf{q}$ values, the pairing potentials are repulsive, whereas the $\mathbf{q}$ points near the M and A points show some pairing. In Fig. 6.2, pairing potentials of the $n = 1$ superlattice for the $4 \times 4 \times 2$ Monkhorst-Pack $\mathbf{q}$ points are presented. Attractive regions are well illustrated in all $\mathbf{q}$ points in the energy of $10 \sim 15$ eV.

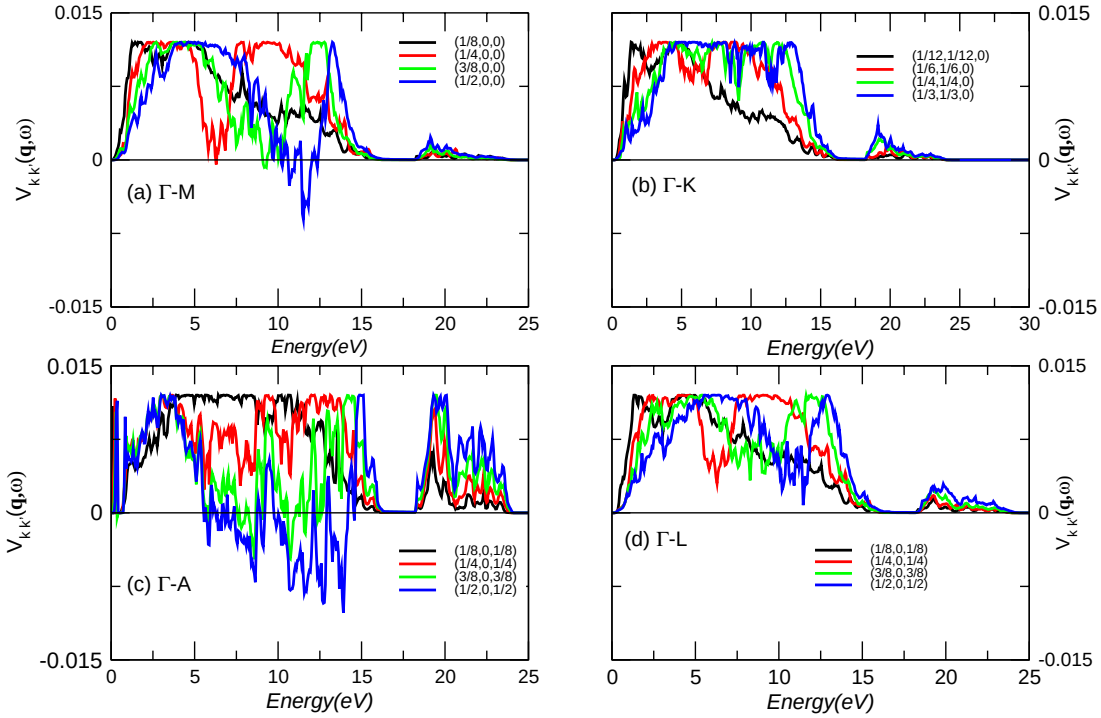

Figure 6.1: Pairing potential of the $n = 1$ superlattice: (a) $\Gamma - M$, (b) $\Gamma - K$, (c) $\Gamma - A$, and $\Gamma - L$.

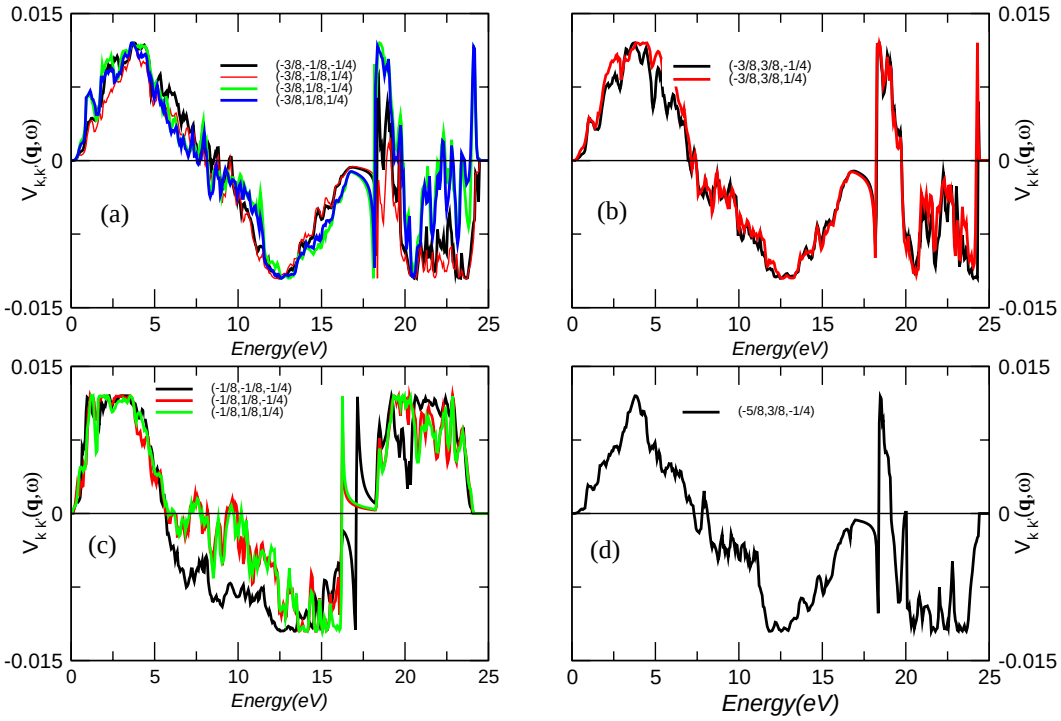

Figure 6.2: Pairing potential of the $n = 1$ superlattice with $\mathbf{q}$ points of $4 \times 4 \times 2$ Monkhorst-Pack mesh.

Second, pairing potentials of the $n = 3$ superlattice are shown in Fig. 6.3 for high symmetry line $\mathbf{q}$ points and Fig. 6.4 for $4 \times 4 \times 2$ Monkhorst-Pack $\mathbf{q}$ points. As seen in Fig. 6.3, some $\mathbf{q}$ points near Γ along $\Gamma - M$ and $\Gamma - K$ show a repulsive pairing potential, whereas the rest of $\mathbf{q}$ points shows an attractive potential. For $\mathbf{q}$ points of the $4 \times 4 \times 2$ Monkhorst-Pack, all $\mathbf{q}$ points show an attractive pairing potential, as shown in Fig. 6.4. The attractive region occurs in all cases in energies of roughly $11 \sim 15$ eV.

Finally, we evaluated the kernel function for $\mathbf{q}$ points from the Monkhorst-Pack mesh as shown in Fig. 6.5 (a) $n = 1$, (b) $n = 3$ of the [111] and (c) $2/8$ of the [001] superlattice.

We use the following expression for the kernel function,

$$K(\omega) = \sum_{\mathbf{q}} w_{\mathbf{q}} V^p(\mathbf{q}, \omega) \tag{6.38}$$

where $w_{\mathbf{q}}$ is the weight of the $\mathbf{q}$ point in the Monkhorst-Pack mesh. The kernel function in Eq. (6.38) is not normalized by the density of states as in Eq. (6.33). Therefore, the values of the kernel functions of each case: $n = 1,\ n = 3$ and $2/8$ do not necessarily represent the strength of the interaction. As seen in Fig. 6.5, the [111] superlattices show an attractive region for $7.5 \sim 16$ eV and $10 \sim 17.5$ eV for the $n = 1$ and $n = 3$ case, respectively. However, $2/8$ (Fig. 6.5(c)) does not show any attractive region in the entire frequency range. The energy where the attractive interaction occurs is a good indication of the pairing energy of Cooper pairs. For pairing energy $\omega = 10$ eV, which corresponds to $12,000$ K in temperature, T_C would be about 80 K for $\lambda_{ex} = 0.2$ and 428 K for $\lambda_{ex} = 0.3$, if we use the simple BCS T_C formula of Eq. 4.15.

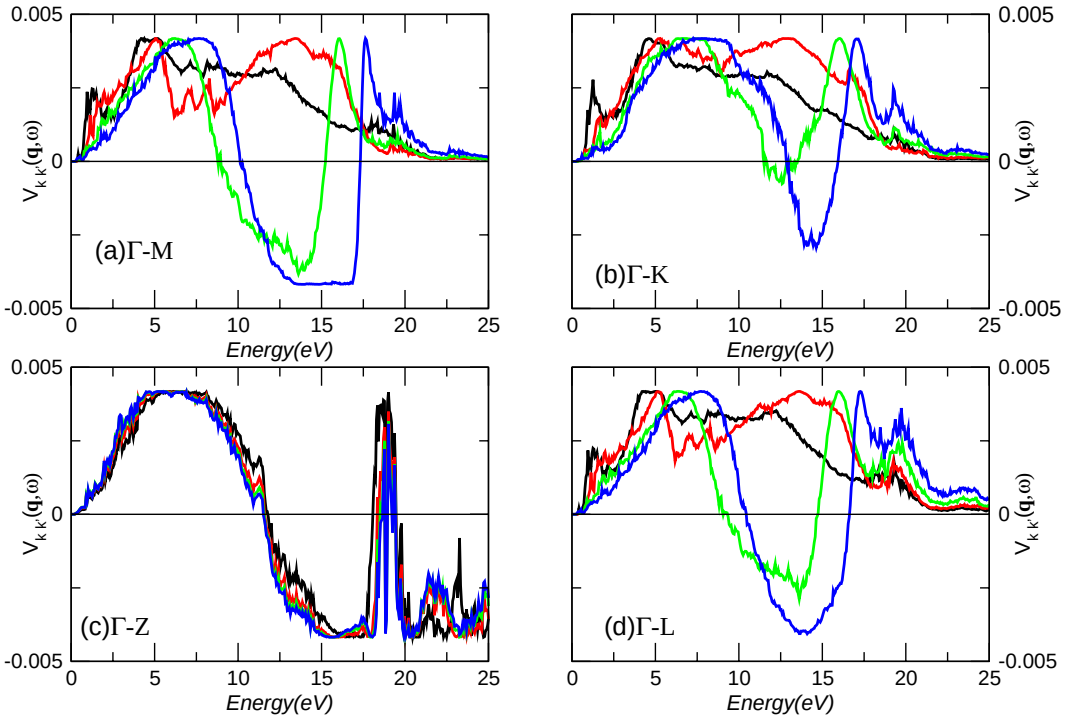

Figure 6.3: Pairing potential of the $n = 3$ superlattice: (a) $\Gamma - M$, (b) $\Gamma - K$, (c) $\Gamma - A$, and $\Gamma - L$.

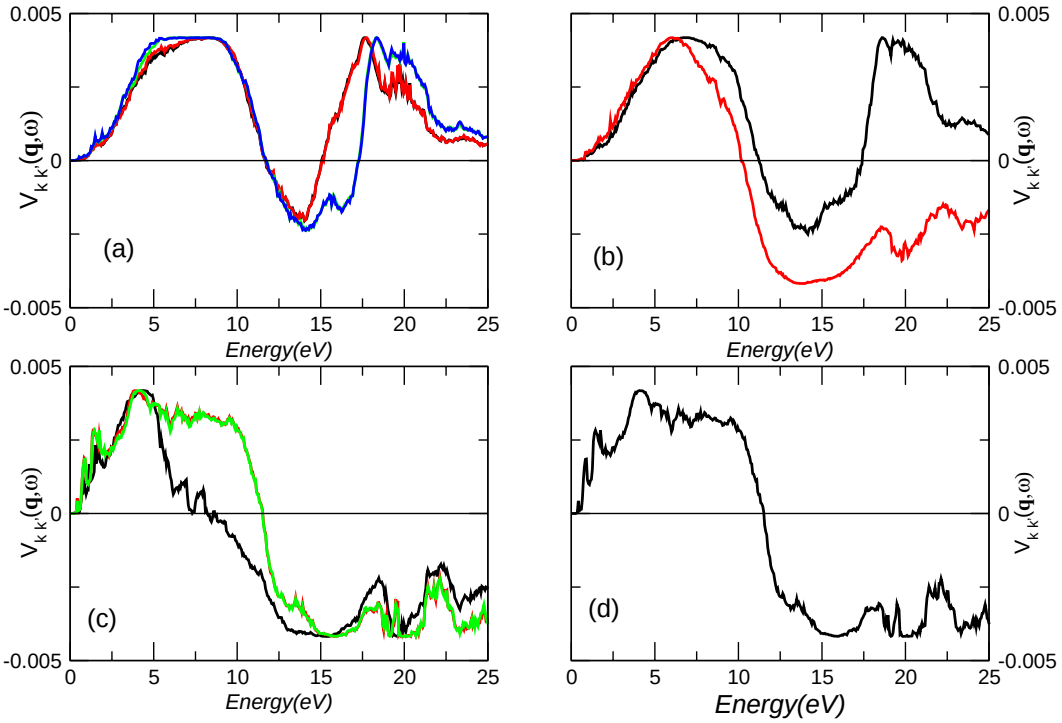

Figure 6.4: Pairing potential of the $n = 3$ superlattice with $\mathbf{q}$ points of $4 \times 4 \times 2$ Monkhorst-Pack mesh.

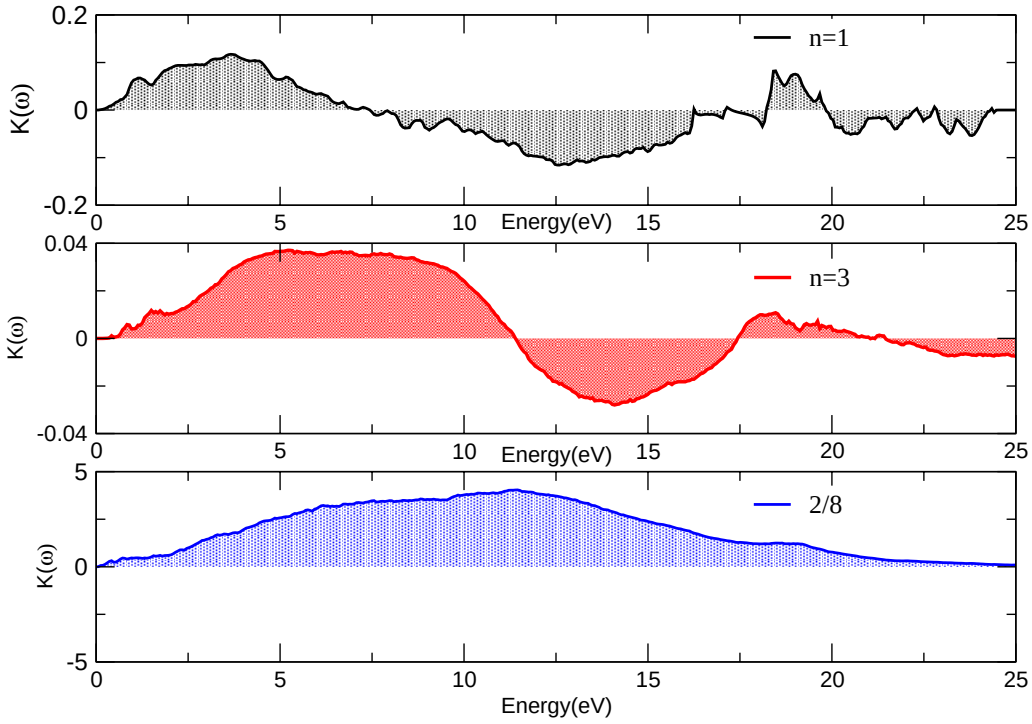

Figure 6.5: Kernel function of CuCl/Si superlattices: (a) $n = 1$, (b) $n = 3$, and (c) $2/8$.

Chapter 7: Conclusion and perspective

In summary, two main topics, optical properties and superconductivity were presented. For all calculations, the highly precise full potential linearized augmented plane wave (FLAPW) method was employed.

Although the local density approximation of the density functional calculations have been successful in describing and predicting ground state properties in many materials, it has shortcomings in descriptions of excited states and underestimates band gaps of many semiconductors. The screened-exchange LDA (sX-LDA) method was proposed and was very successful in describing excited states and has improved the LDA band gap problems.

The optical properties [$\varepsilon(\omega),\ n(\omega),\ k(\omega),\ R(\omega), \alpha(\omega)$] of some III-V semiconductors, such as InAs, InSb, GaSb, and AlSb, were calculated using sX-LDA plus spin-orbit coupling with self-consistent eigenvalues and eigenfunctions without adjustable parameters, such as the commonly used scissor operator. Superconductivity is an intensively and extensively studied topic in condensed matter physics. Although superconductivity has many potential applications, progress is hindered by the low T_C relative to room temperature. As an exploration to raise the T_C much higher than the conventional phonon mediated approach, the excitonic mechanism was proposed by Little and Ginzburg in the early 60's. ABB later studied the metal-insulator interface model and showed that exciton mediation

could exist and enhance T_C much more than the phonon mediated approach. In spite of subsequent experiments to find excitonic derived T_C's, no experiments have confirmed superconductivity. Mattes and Foiles, in 1985, reported almost an ideal diamagnetic susceptibility at 60$\sim$ 150 K in CuCl grown epitaxially on a Si (111) substrate. Yu and Freeman, encouraged by Bardeen, showed that there was interface metallicity and that interface superconductivity might be plausible. However, CuCl/Si superlattices were forgotten for 20 years after the discovery of cuprates in 1986. Here we continued and extended Yu and Freeman's work of CuCl/Si superlattices: $n = 1$ and $n = 3$ CuCl of [111] and $2/8$, $4/8$, and $4/12$ of [001] superlattices were investigated. In all superlattices, we found interface metallicity as evidenced by bands, Fermi surfaces and charge densities. This resembles the dielectric-metal-dielectric sandwich structure proposed by Ginzburg. T_C was estimated in the electron-phonon mediation scheme using the rigid muffin-tin approximation, giving $0.04 \sim 4.4$ K for the CuCl/Si superlattices. ZnS/Si and GaP/Si superlattices were studied to see if these superlattices show a similar behavior to CuCl/Si. While interface metallicity is present in the ZnS/Si and GaP/Si superlattices, there is no superconductivity within the electron-phonon mechanism, which makes CuCl/Si superlattices special.

To explore the possibility of an excitonic mechanism, we reformulated the pairing potential and the kernel function in the LAPW basis. Pairing potentials were found to be attractive for some $\mathbf{q}$ vectors, and the kernel function evaluation showed that there could be excitonic pairing in the $n = 1$ and $n = 3$ CuCl/Si superlattices, not in the $2/8$ superlattices. However, since the number of $\mathbf{q}$ points we used in the calculations are small, calculations with a larger number of $\mathbf{q}$ points is necessary to confirm the electronic pairing.

References

[1] P. Hohenberg and W. Kohn, Phys. Rev. **136**, B864 (1964).

[2] W. Kohn and L. J. Sham, Phys. Rev. **140**, A1133 (1965).

[3] L. Hedin and B. I. Lundqvist, J. Phys. C **4**, 2064 (1971).

[4] B. M. Bylander and L. Kleinman, Phys. Rev. B **41**, 7868 (1990).

[5] R. Asahi, W. Mannstadt, and A. J. Freeman, Phys. Rev. B **59**, 7486 (1999).

[6] R. Asahi, Ph.D. thesis, Northwestern University, 1999.

[7] E. Maxwell, Phys. Rev. **78**, 477 (1950).

[8] C. A. Reynolds, B. Serin, W. H. Wright, and L. B. Nesbitt, Phys. Rev. **78**, 487 (1950).

[9] W. A. Little, Phys. Rev. **134**, A1416 (1964).

[10] V. L. Ginzburg, Zh. Eksp. Teor. Fiz. **47**, 2318 (1964), [Sov. Phys.-JETP 20, 1549 (1965)]; Phys. Lett. 13, 101 (1964).

[11] D. Allender, J. Bray, and J. Bardeen, Phys. Rev. B **7**, 1020 (1973).

[12] B. L. Mattes and C. L. Foiles, Physica **135B**, 139 (1985).

[13] J. J. Yu and A. J. Freeman, Army Research Conf.,NJ, Dec.15,1986 (unpublished).

[14] E. Wimmer, H. Krakauer, M. Weinert, and A. J. Freeman, Phys. Rev. B **24**, 864 (1981).

[15] H. J. F. Jansen and A. J. Freeman, Phys. Rev. B **30**, 561 (1984).

[16] A. Seidl *et al.*, Phys. Rev. B **53**, 3764 (1996).

[17] M. Weinert, (unpublished).

[18] S. H. Rhim, M. Kim, A. J. Freeman, and R. Asahi, Phys. Rev. B **71**, 045202 (2005).

[19] J. Bardeen, L. Cooper, and J. R. Schrieffer, Phys. Rev. **108**, 1175 (1957).

[20] W. L. McMillan, Phys. Rev. **167**, 331 (1968).

[21] G. D. Gaspari and B. L. Gyorffy, Phys. Rev. Lett. **28**, 801 (1972).

[22] S. H. Rhim *et al.*, Phys. Rev. B **76**, 184505 (2007).

[23] P. E. Blöchl, O. Jepsen, and O. K. Andersen, Phys. Rev. B **49**, 16223 (1994).

[24] L. H. Thomas, Proc. Cambridge Philo. Soc. **23**, 542 (1927).

[25] E. Fermi, Z. Phys. **48**, 73 (1928).

[26] J. von Barth and L. Hedin, J. Phys. C **5**, 1629 (1972).

[27] V. Fock, Z. Phys. **61**, 126 (1930), *ibid* **62** 795.

[28] J. C. Slater, Phys. Rev. **81**, 385 (1951).

[29] O. K. Andersen, Phys. Rev. B **12**, 3060 (1975).

[30] M. Weinert, J. Math. Phys. **22**, 2433 (1981).

[31] L.-H. Ye, (unpublished).

[32] H. Ehrenreich and M. H. Cohen, Phys. Rev. **115**, 786 (1959).

[33] G. Greenwood, Proc. Phys. Soc. London **71**, 585 (1958).

[34] S. B. Trickey, F. R. G. Jr., and F. W. Averill, Phys. Rev. B **8**, 4822 (1973).

[35] J. P. Perdew and M. Levy, Phys. Rev. Lett. **51**, 1884 (1983).

[36] L. J. Sham and M. Schlüter, Phys. Rev. Lett. **51**, 1888 (1983).

[37] S. Adachi, J. Appl. Phys. **66**, 6030 (1989).

[38] G. A. Baraff and M. Schlüter, Phys. Rev. B **30**, 11789 (1984).

[39] R. D. Sole and R. Girlanda, Phys. Rev. B **48**, 11789 (1993).

[40] M. Alouani, L. Brey, and N. E. Christensen, Phys. Rev. B **37**, 1167 (1988).

[41] L. Hedin, Phys. Rev. (1965).

[42] S. Albrecht and L. Reining, Phys. Rev. Lett. **80**, 4510 (1998).

[43] A. F. Strace, Phys. Rev. A **3**, 1242 (1971).

[44] F. Gygi and A. Baldereschi, Phys. Rev. Lett. **48**, 2160 (1989).

[45] S. Massidda, A. Continenza, M. Posternak, and A. Baldereschi, Phys. Rev. Lett. **74**, 2323 (1995).

[46] S. Massidda, A. Continenza, M. Posternak, and A. Baldereschi, Phys. Rev. B **55**, 13494 (1997).

[47] W. Wolf *et al.*, Bull. Am. Phys. Soc. **43**, 797 (1998).

[48] C. B. Geller *et al.*, Appl. Phys. Lett. **79**, 368 (2001).

[49] R. Asahi, W. Mannstadt, and A. J. Freeman, Phys. Rev. B **62**, 2552 (2000).

[50] H. J. Monkhorst and J. D. Pack, Phys. Rev. B **13**, 5188 (1976).

[51] Z. H. Levine and D. C. Allen, Phys. Rev. Lett. **63**, 1719 (1989).

[52] O. Madelung, in *Introduction to Solid-State Theory*, edited by M. Cardona, P. Fulde, and H.-J. Queisser (Springer, New York, 1996), p. 262.

[53] S. Massidda *et al.*, Phys. Rev. B **41**, 12079 (1990).

[54] N. W. Ashcroft and N. D. Mermin, *Solid State Physics* (Holt, Rinehart and Winston, New York, 1976).

[55] J. Spitzer *et al.*, J. Appl. Phys. **77**, 811 (1995).

[56] T. Miyazaki and S. Adachi, Jpn. J. Appl. Phys. **31**, 979 (1992).

[57] M. M. noz *et al.*, Phys. Rev. B **60**, 8105 (1999).

[58] S. Zollner *et al.*, J. Appl. Phys. **66**, 383 (1989).

[59] D. E. Aspnes and A. A. Studna, Phys. Rev. B **27**, 985 (1983).

[60] B. O. Seraphin and H. E. Bennett, in *Semiconductors and Semimetals*, edited by R. K. Wilardson and A. C. Beer (Academic Press, ADDRESS, 1967), No. p.499.

[61] M. Cardona, *Solid state Physics* (Academic Press, New York, 1969).

[62] H. K. Onnes, Leiden Commun. **124C**, (1911).

[63] H. Kamimura, H. Ushio, S. Matsuno, and T. Hamada, in *Theory of copper oxide superconductors* (Springer, Berlin;New York, 2005).

[64] M. L. Cohen, Phys. Rev. **134**, A511 (1964).

[65] J. F. Schooley, W. R. Hosler, and M. L. Cohen, Phys. Rev. Lett. **12**, 474 (1964).

[66] W. Meissner and R. Ochsenfeld, Naturwiss. **21**, 787 (1933).

[67] C. J. Gorter, Nature **132**, 931 (1933).

[68] J. Bardeen, Phys. Rev. **79**, 167 (1950).

[69] J. Bardeen and D. Pines, Phys. Rev. **99**, 1140 (1955).

[70] P. W. Anderson, Phys. Rev. **112**, 1900 (1958).

[71] N. N. Boguliubov, N. V. Tolmachev, and D. V. Shirkov, *A New Method in the Theory of Superconductivity* (Consultants Bureau, Inc., New York, 1959).

[72] P. G. de Gennes, *Superconductivity of Metals and Alloys* (W. A. Benjamin, Inc., New York, 1966).

[73] L. P. Gor'kov, Zh. Eksperim. i. Teor. Fiz. **34**, 735 (1958).

[74] V. L. Ginzburg and L. D. Landau, Zh.Eksperim. i. Teor. Fiz. **20**, 1064 (1950).

[75] P. Morel and P. W. Anderson, Phys. Rev. **125**, 1263 (1962).

[76] J. P. Carbotte and F. Marsiglio, in *The Physics of superconductors: Conventional and High-T_C superconductors*, edited by K. H. Bennemann and J. B. Ketterson (Springer Verlag, New York, 2003), Chap. 4, p. 123.

[77] P. B. Allen and B. Mitrovic, in *Solid state physics*, edited by F. S. H. Ehrenreich and D. Turnbull (Academic, New York, 1982), Vol. 37, p. 1.

[78] A. A. Abrikosov, L. P. Gorkov, and I. E. Dzyaloshisnki, *Methods of the Quantum Field theory in Statistical Physics* (Dover, New York, 1975).

[79] H. J. Choi, M. L. Cohen, and S. G. Louie, Physica C **385**, 66 (2003).

[80] Y. Nambu, Phys. Rev. **117**, 648 (1960).

[81] F. Marsiglio, M. Schossmann, and J. P. Carbotte, Phys. Rev. B **37**, 4965 (1988).

[82] P. B. Allen and R. C. Dynes, Phy. Rev. B **12**, 905 (1975).

[83] H. L. Skriver and I. Mertig, Phys. Rev. B **32**, 4431 (1985).

[84] H. L. Skriver and I. Mertig, Phys. Rev. B **41**, 6553 (1990).

[85] J. J. Hopfield, Phys. Rev. **186**, 443 (1969).

[86] V. L. Ginzburg, Contemp. Phys. **9**, 355 (1968).

[87] V. L. Ginzburg, Ann. Rev. of Mat. Sci. **2**, 663 (1972).

[88] M. L. Cohen and P. W. Anderson, in *Superconductivity in d- and f-band metals*, edited by D. H. Douglas (Plenum Press, New York, 1972), p. 17.

[89] J. C. Inkson and P. W. Anderson, Phys. Rev. B **8**, 4429 (1973).

[90] D. Allender, J. Bray, and J. Bardeen, Phys. Rev. B **8**, 4433 (1973).

[91] M. L. Cohen and S. G. Louie, in *Superconductivity in d- and f-band metals*, edited by D. H. Douglas (Plenum Press, New York, 1976), p. 7.

[92] O. Zakharov, M. L. Cohen, S. G. Louie, and D. R. Penn, J. Phys. Condens. Matter **9**, 8501 (1997).

[93] G. A. Baraff, J. A. Appelbaum, and D. R. Hamann, Phys. Rev. Lett. **38**, 237 (1977).

[94] W. A. Harrison, E. A. Kraut, J. R. Waldrop, and R. W. Grant, Phys. Rev. B **18**, 4402 (1978).

[95] R. W. Grant, J. R. Waldrop, and E. A. Kraut, Phys. Rev. Lett. **40**, 656 (1978).

[96] T. Wang, N. Moll, K. Cho, and J. D. Joannopoulos, Phys. Rev. Lett. **82**, 3304 (1999).

[97] A. Ohtomo, D. A. Muller, J. L. Grazul, and H. Y. Hwang, Nature **419**, 378 (2002).

[98] S. Okamoto and A. J. Millis, Nature **428**, 630 (2004).

[99] A. Ohtomo and H. Y. Hwang, Nature **427**, 423 (2004).

[100] S. Okamoto and A. J. Millis, Physica B **359**, 1378 (2005).

[101] D. L. Miller, M. Strongin, O. F. Kammerer, and B. G. Streetman, Phys. Rev. B **8**, 4416 (1973).

[102] M. Strongin, O. F. Kammerer, H. H. Farrell, and D. L. Miller, Phys. Rev. Lett. **30**, 129 (1973).

[103] C. C. Tsuei and W. L. Johnson, Phys. Rev. B **9**, 4742 (1974).

[104] D. L. Miller, M. Strongin, O. F. Kammerer, and B. G. Streetman, Phys. Rev. B **13**, 4834 (1976).

[105] N. B. Brandt, S. V. Kuvshinnikov, A. P. Rusakov, and V. M. Semenov, JETP Lett. **27**, 33 (1978).

[106] C. W. Chu *et al.*, Phys. Rev. B **18**, 2116 (1978).

[107] A. A. Abrikosov, JETP Lett. **27**, 219 (1978).

[108] A. A. Abrikosov, J. Less-Common Metals **62**, 451 (1978).

[109] B. L. Mattes, Physica C **162-164**, 554 (1989).

[110] M. Cardona, Phys. Rev. **129**, 69 (1963).

[111] A. Göbel *et al.*, Phys. Rev. B **57**, 15183 (1998).

[112] S. Hull and D. A. Keen, Phys. Rev. B **50**, 5868 (1994).

[113] H.-C. Hsueh *et al.*, Phys. Rev. B **51**, 12216 (1995).

[114] G. C. Vezzoli, Phys. Rev. B **26**, 4140 (1982).

[115] C.-Z. Wang, R. Yu, and H. Krakauer, Phys. Rev. Lett. **72**, 368 (1994).

[116] S. Lewonczuk, J. G. Gross, and J. Ringeissen, Phys. Rev. B **27**, 1259 (1983).

[117] Y. Ma, J. S. Tse, and D. D. Klug, Phys. Rev. B **67**, 140301 (2003).

[118] A. Göbel *et al.*, Phys. Rev. B **56**, 210 (1997).

[119] C. Ulrich, A. Göbel, K. Syassen, and M. Cardona, Phys. Rev. Lett. **82**, 351 (1999).

[120] S.-H. Wei, S. B. Zhang, and A. Zunger, Phys. Rev. Lett. **70**, 1639 (1993).

[121] C. H. Park and D. J. Chadi, Phys. Rev. Lett. **76**, 2314 (1996).

[122] S. R. Bickham, J. D. Kress, L. A. Collins, and R. Stumpf, Phys. Rev. Lett. **83**, 568 (1999).

[123] A. Zunger and M. L. Cohen, Phys. Rev. B **20**, 1189 (1979).

[124] T. C. Collins, M. Chandrasekhar, and M. Seel, Int. J. Quant. Chem. **26**, 831 (1984).

[125] T. C. Collins *et al.*, Phys. Rev. B **27**, 140 (1983).

[126] C. W. Chu and H. K. Mao, Phys. Rev. B **20**, 4474 (1979).

[127] G. C. Vezzoli and J. Bera, Phys. Rev. B **23**, 3022 (1981).

[128] H. G. Salunke, R. Mittal, G. P. Das, and S. L. Chaplot, J. Phys. Condens. Mattter **9**, 10137 (1997).

[129] D. G. Pettifor, J. Phys. F **7**, 1009 (1977).

[130] D. Glözel, D. Rainer, and H. R. Schober, Z. Phys. B **35**, 317 (1979).

[131] Z. Vardeny, G. Gilat, and D. Moses, Phys. Rev. B **18**, 4487 (1978).

[132] E. G. Maksimov and D. I. Khomskii, in *High-Temperature Superconductivity*, edited by V. L. Ginzburg and D. A. Kirzhnits (Consultants Burea, New York and London, 1977), Chap. 4.

[133] K. Bennemann and J. Garland, in *Superconductivity in d- and f-band metals*, No. 3 in *AIP Conf. Proc.*, edited by D. H. Douglas (AIP, New York, 1972), p. 103.

[134] O. Madelung, *Numerical Data and functional relationships in Science and Technology, New Series, Group III* (Springer, Berlin, 1989), Vol. 22.

[135] http://www.ioffe.ru/SVA/NSM/ .

[136] D. A. Kirzhnits, Sov. Phys. Usp. **19**, 530 (1977).

[137] M. Weinert, (private communication).

[138] S. L. Adler, Phys. Rev. **126**, 413 (1962).

[139] J. Ihm, M. L. Cohen, and S. F. Tuan, Phys. Rev. B **23**, 3258 (1981).

[140] V. L.Ginzburg, Ann. Rev. Mater. Sci. **2**, 663 (1972), in *High-Temperature Superconductivity* (1977), Ch.1, edited by V. L. Ginzburg and D. A. Kirzhnits.

Appendix A: Fourier transform of bare Coulomb potential and pairing potential

In this appendix, we re-derive the Fourier component of the bare Coulomb potential and its effective screened potential with and without the local-field contribution, and we revisit the expression of the kernel function in plane wave basis by Zakharov *et al.*[92] and generalize it into the LAPW basis.

Without the local-field, the Fourier transform of a bare Coulomb potential would be

$$V(\mathbf{q}) = \frac{1}{\Omega}\int d\mathbf{r}\int d\mathbf{r}'\frac{e^2}{|\mathbf{r}-\mathbf{r}'|^2}\exp[i\mathbf{q}\cdot(\mathbf{r}-\mathbf{r}')] = \frac{4\pi e^2}{q^2}, \tag{1}$$

which becomes

$$\begin{aligned} V_{\mathbf{G},\mathbf{G}'}(\mathbf{q}) &= \frac{1}{\Omega}\int d\mathbf{r}\int d\mathbf{r}'\exp[i(\mathbf{q}+\mathbf{G})\cdot\mathbf{r}]\,\frac{e^2}{|\mathbf{r}-\mathbf{r}'|^2}\exp[-i(\mathbf{q}+\mathbf{G}')\cdot\mathbf{r}'] \\ &= \frac{1}{\Omega}\int d\mathbf{r}\int d\mathbf{r}'\exp[i(\mathbf{q}+\mathbf{G})\cdot\mathbf{r}]\,\frac{e^2}{|\mathbf{r}-\mathbf{r}'|^2}\exp[-i(\mathbf{q}+\mathbf{G})\cdot\mathbf{r}']\,\exp[i(\mathbf{G}-\mathbf{G}')\cdot\mathbf{r}'] \\ &= \frac{1}{\Omega}\int d\mathbf{x}\int d\mathbf{r}'\exp[i(\mathbf{q}+\mathbf{G})\cdot\mathbf{x}]\,\frac{e^2}{\mathrm{x}^2}\exp[i(\mathbf{G}-\mathbf{G}')\cdot\mathbf{r}'] \\ &= \frac{4\pi e^2}{\Omega|\mathbf{q}+\mathbf{G}|^2}\delta(\mathbf{G}-\mathbf{G}'), \end{aligned} \tag{2}$$

when local-field contribution is considered, where $\mathbf{x} = \mathbf{r} - \mathbf{r}'$ and Ω is the volume of the unit cell. In most of the literature, the delta function in Eq. (2) is omitted for brevity.

The effective screening potential, $V^{eff}_{\mathbf{G},\mathbf{G}'}(\mathbf{q},\omega)$, is expressed in momentum space as a matrix multiplication of the bare Coulomb potential and the inverse dielectric function,

$$V^{eff}_{\mathbf{G},\mathbf{G}'}(\mathbf{q},\omega) = \sum_{\mathbf{G}''} V_{\mathbf{G},\mathbf{G}''}(\mathbf{q},\omega)\epsilon^{-1}_{\mathbf{G}'',\mathbf{G}'}(\mathbf{q},\omega). \tag{3}$$

The real space representation of the effective screened potential, $V^s(\mathbf{r},\mathbf{r}')$, is obtained via

the inverse Fourier transform of $V^{eff}_{\mathbf{G},\mathbf{G}'}(\mathbf{q},\omega)$:

$$V^s(\mathbf{r},\mathbf{r}';\omega) = \sum_{\mathbf{q}} \sum_{\mathbf{G},\mathbf{G}'} e^{i(\mathbf{q}+\mathbf{G})\cdot\mathbf{r}}\, V^{eff}_{\mathbf{G},\mathbf{G}'}(\mathbf{q},\omega) e^{-i(\mathbf{q}+\mathbf{G}')\cdot\mathbf{r}'}, \tag{4}$$

where ω is determined by the frequency of the inverse dielectric function.

It is worthwhile to check the relations between $\mathbf{k}'$ and $\mathbf{k}+\mathbf{q}$ by looking into the pairing potential. Rewriting the pairing potential $V^{eff}_{\mathbf{G},\mathbf{G}'}$ in terms of the inverse dielectric function, it is expressed as in Eq. (6.18) of Chapter 6:

$$V^p_{\mathbf{k},\mathbf{k}'} = \frac{4\pi e^2}{\Omega} \sum_{\mathbf{q},\mathbf{G},\mathbf{G}'} P(\mathbf{k},\mathbf{q},\mathbf{G}) \cdot \frac{\varepsilon^{-1}_{\mathbf{G},\mathbf{G}'}(\mathbf{q},\omega)}{|\mathbf{q}+\mathbf{G}|^2} \cdot P^*(\mathbf{k},\mathbf{q},\mathbf{G}'), \tag{5}$$

where the optical matrix $P(\mathbf{k},\mathbf{q},\mathbf{G})$ is

$$P(\mathbf{k},\mathbf{q},\mathbf{G}) = \langle \mathbf{k}',\varepsilon' | e^{i(\mathbf{q}+\mathbf{G})\cdot\mathbf{r}} | \mathbf{k},\varepsilon \rangle. \tag{6}$$

We note that any Bloch state can be expanded by Fourier series,

$$|\mathbf{k}\rangle = e^{i\mathbf{k}\cdot\mathbf{r}} u_{\mathbf{k}}(\mathbf{r}) = e^{i\mathbf{k}\cdot\mathbf{r}} \sum_{\mathbf{G}} \frac{1}{\Omega} c_{\mathbf{G}} e^{i\mathbf{G}\cdot\mathbf{r}}, \tag{7}$$

where $u_{\mathbf{k}}(\mathbf{r})$ is the periodic part of the Bloch state and $c_{\mathbf{G}}$ are the Fourier coefficients. Inserting Eq. (7) into Eq. (5) gives the optical matrix $P(\mathbf{k},\mathbf{q},\mathbf{G})$ in terms of Fourier coefficients

$$\begin{aligned} & \int d\mathbf{r} e^{i(\mathbf{q}+\mathbf{G})\cdot\mathbf{r}} \Big[\frac{1}{\Omega} e^{-i\mathbf{k}'\cdot\mathbf{r}} \sum_{\mathbf{G}_1} \frac{1}{\Omega} c_{\mathbf{G}_1} e^{-i\mathbf{G}_1\cdot\mathbf{r}}\Big] \Big[\frac{1}{\Omega} e^{i\mathbf{k}\cdot\mathbf{r}} \sum_{\mathbf{G}_2} \frac{1}{\Omega} c_{\mathbf{G}_2} e^{i\mathbf{G}_2\cdot\mathbf{r}}\Big] \\ = & \sum_{\mathbf{G}_1,\mathbf{G}_2} c^*_{\mathbf{G}_1} c_{\mathbf{G}_2} \delta(\mathbf{q}+\mathbf{G}-\mathbf{k}'+\mathbf{k}-\mathbf{G}_1+\mathbf{G}_2). \end{aligned} \tag{8}$$

From Eq. (8), $P(\mathbf{k},\mathbf{q},\mathbf{G})$ vanishes unless $\mathbf{k}'-\mathbf{k}-\mathbf{q} = \mathbf{G}-\mathbf{G}_1+\mathbf{G}_2$. Since $\mathbf{G}$ vectors are the reciprocal lattice vectors, $\mathbf{k}' = \mathbf{k}+\mathbf{q}+\mathbf{G}_o$, where $\mathbf{G}_o$ is the reciprocal lattice vector

without which the pairing potential would vanish. Hence, in the plane wave representation the optical matrix

$$P(\mathbf{k},\mathbf{q},\mathbf{G}) = \sum_{\mathbf{G}_2} c^*_{\mathbf{G}_2+\mathbf{G}-\mathbf{G}_0} c_{\mathbf{G}_2} \equiv Z_{\mathbf{G}}. \tag{9}$$

The pairing potential $V_{\mathbf{k},\mathbf{k}'}$ in the plane wave basis becomes that of Zakharov *et al*:[92]

$$V^p_{\mathbf{k},\mathbf{k}'} = \frac{4\pi e^2}{\Omega} \sum_{\mathbf{q},\mathbf{G},\mathbf{G}'} Z^*_{\mathbf{G}} \frac{\varepsilon^{-1}_{\mathbf{G},\mathbf{G}'}(\mathbf{q},\omega)}{|\mathbf{q}+\mathbf{G}|^2} Z_{\mathbf{G}'} \ , \tag{10}$$

with the restriction that $\mathbf{k}' = \mathbf{k} + \mathbf{q} + \mathbf{G}_0$. This relation does not change if one uses the LAPW basis since any Bloch state satisfies periodicity and can be represented by a Fourier expansion. Therefore, $\mathbf{k}' = \mathbf{k} + \mathbf{q} + \mathbf{G}_0$ should hold if we have a nonvanishing pairing potential in momentum space.

Appendix B: The tetrahedron summation involving the Dirac delta function

We give the improved tetrahedron method by Blöchel, Jepsen, and Andersen:[23]

$$\langle X \rangle = \sum_n \int d\mathbf{k}\ X_n(\mathbf{k}) f(e_\mathbf{k}), \tag{11}$$

where $f(e_\mathbf{k})$ is the Fermi-Dirac function, n is the band index, and $X_n(\mathbf{k})$ is defined as

$$X_n(\mathbf{k}) = \langle \Psi_n(\mathbf{k}) | \hat{X} | \Psi_n(\mathbf{k}) \rangle, \tag{12}$$

the expectation value of the operator $\hat{X}$ for a given wave function $\Psi_n(\mathbf{k})$. The integral in Eq. (11) can be rewritten in terms of the theta function,

$$\langle X \rangle = \sum_n \int d\mathbf{k}\ X_n(\mathbf{k}) \theta(e - e_\mathbf{k}). \tag{13}$$

For a given set of *k* points, $X_n(\mathbf{k})$ is interpolated as $\bar{X}_n(\mathbf{k})$ inside the tetrahedron so that

$$\bar{X}_n(\mathbf{k}) = \sum_j X(\mathbf{k}_j) w_j(\mathbf{k}). \tag{14}$$

Using the interpolated function, Eq. (11) can be further rewritten as

$$\begin{aligned}
\langle X \rangle &= \sum_n \int d\mathbf{k}\ X_n(\mathbf{k}) \theta(e - e_\mathbf{k}) && (15)\\
&= \sum_n \int d\mathbf{k}\ \bar{X}_n(\mathbf{k}) \theta(e - e_\mathbf{k}) && (16)\\
&= \sum_n \int d\mathbf{k}\ [\sum_j X_n(\mathbf{k}_j) w_j(\mathbf{k})] \theta(e - e_\mathbf{k}) && (17)\\
&= \sum_t \sum_n [\sum_j X_n(\mathbf{k}_j) w_{nj}], && (18)
\end{aligned}$$

where in the last line, we invoked the tetrahedron summation with index t. Thus, w_{nj} is given as

$$w_{nj} = \int d\mathbf{k}\; w_j(\mathbf{k})\theta(e - e_{\mathbf{k}}). \tag{19}$$

where all four values are shown in the Appendix of Blöchel *et al.*[23] depending on the energies of corner points and E_F.

In the calculation of optical properties, the integration of the Dirac delta function appears often for the imaginary part of dielectric function. Taking the energy derivative of $\langle X \rangle$ given in Eq. (15), one obtains

$$\begin{aligned}
-\frac{\partial}{\partial e}\langle X\rangle &= \sum_n \int d\mathbf{k}\; X_n(\mathbf{k})[-\frac{\partial}{\partial e}\theta(e - e_{\mathbf{k}})] && (20)\\
&= \sum_n \int d\mathbf{k}\; X_n(\mathbf{k})\delta(e - e_{\mathbf{k}}) && (21)\\
&= \sum_n \int d\mathbf{k}\; \Big[\sum_j X_n(\mathbf{k}_j) w_j(\mathbf{k})\Big]\delta(e - e_{\mathbf{k}}) && (22)\\
&= \sum_t \sum_n \sum_j X_n(\mathbf{k}_j)\dot{w}_{nj}\;. && (23)
\end{aligned}$$

In this formulation $\dot{w}_{nj}$ is expressed as

$$\begin{aligned}
\dot{w}_{nj} &= \int d\mathbf{k}\; w_j(\mathbf{k})\delta(e - e_{\mathbf{k}}) && (24)\\
&= \int d\mathbf{k}\; w_j(\mathbf{k})(-\frac{\partial}{\partial e}\theta(e - e_{\mathbf{k}})) && (25)\\
&= -\frac{\partial}{\partial e}\int d\mathbf{k}\; w_j(\mathbf{k})\theta(e - e_{\mathbf{k}}) && (26)\\
&= -\frac{\partial}{\partial e} w_{nj}. && (27)
\end{aligned}$$

The energy derivatives of the weights, $\dot{w}_{nj}$, can be directly obtained from the weights w_{nj}. However, to increase numerical stability, we use the following expression for $\dot{w}_{nj}$, where the corner point energies are sorted according to $e_1 \le e_2 \le e_3 \le e_4$, and the short-

hand notation for energy difference $e_{ij} = e_i - e_j$ is employed:

$$
\begin{aligned}
&\text{(i)} && e < e_1 && (28)\\
&\dot{w}_i &=& \ 0, && (29)\\
&\text{(ii)} && e_1 < e < e_2 &\\
&C &=& \ \frac{1}{e_{21}e_{31}e_{41}}(e-e_1)^2 && (30)\\
&\dot{w}_1 &=& \ C \cdot \Big[3 - (e-e_1)(\frac{1}{e_{21}} + \frac{1}{e_{31}} + \frac{1}{e_{41}})\Big] &\\
&\dot{w}_2 &=& \ C \cdot \frac{e-e_1}{e_{21}} &\\
&\dot{w}_3 &=& \ C \cdot \frac{e-e_1}{e_{31}} &\\
&\dot{w}_4 &=& \ C \cdot \frac{e-e_1}{e_{41}} &\\
&\text{(iii)} && e_2 < e < e_3 &\\
&\dot{w}_1 &=& \ \frac{(e-e_2)^3}{e_{41}e_{31}e_{32}e_{42}} \times \Big[\frac{(e_{42}+e_{31})(e_{41}+e_{31})}{e_{41}e_{31}} - 1\Big] && (31)\\
&&+& \ \frac{3(e-e_2)+8e_{21}}{e_{41}e_{31}} - \Big[3(e-e_2)^2 + 3(e-e_2)e_{21} + e_{21}^2\Big]\frac{(e_{41}+e_{31})}{e_{41}^2e_{31}^2} &\\
&\dot{w}_2 &=& \ \frac{(e-e_2)^3}{e_{41}e_{31}e_{32}e_{42}} \cdot [1 + ((e_{41}+e_{31})(e_{42}+e_{31}) - 2e_{31}e_{41})\frac{1}{e_{42}e_{32}}] &\\
&&-& \ 3(e-e_2)^2 \cdot (e_{42}+e_{31})\frac{1}{e_{41}e_{31}e_{42}e_{32}} &\\
&&+& \ \Big[3(e-e_2) + 4e_{21}\Big]\frac{1}{e_{41}e_{31}} &\\
&\dot{w}_3 &=& \ \frac{(e-e_2)^3}{e_{41}e_{42}(e_{31}^2)(e_{32}^2)} \cdot [e_{21} \cdot (e_{42}+e_{31}) - e_{31}(e_{42}+e_{31}+e_{41})] &\\
&&+& \ \Big[3 \cdot (e-e_2)^2 + 3(e-e_2)e_{21} + \frac{e_{21}^2}{e_{41}e_{31}e_{31}}\Big] &\\
&\dot{w}_4 &=& \ \frac{(e-e_2)^3}{e_{31}e_{41}^2e_{32}e_{42}^2} \cdot \Big[e_{21}(e_{42}+e_{31}) - e_{41} \cdot (e_{42}+2e_{31})\Big] &\\
&&+& \ \Big[3(e-e_2)^2 + 3(e-e_2) \cdot e_{21} + e_{21}^2\Big]\frac{1}{e_{41}e_{41}e_{31}} &
\end{aligned}
$$

(iv) $e_3 < e < e_4$

$$C = \frac{(e_4 - e)^2}{e_{41}e_{42}e_{43}} \tag{32}$$

$$\dot{w}_1 = C\frac{e_4 - e)}{e_{41}}$$

$$\dot{w}_2 = C\frac{(e_4 - e)}{e_{42}}$$

$$\dot{w}_3 = C\frac{(e_4 - e)}{e_{43}}$$

$$\dot{w}_4 = C\Big(3 - (\frac{1}{e_{41}} + \frac{1}{e_{42}} + \frac{1}{e_{43}}) \cdot (e_4 - e)\Big)$$

(v) $e > e_4$

$$\dot{w}_i = \frac{1}{4} \tag{33}$$